

© 2021 by Zoë Richter. All rights reserved.

ISOTOPIC AND REACTOR PHYSICS CHARACTERIZATION OF A GAS-COOLED, PEBBLE-BED  
MICROREACTOR

BY

ZOË RICHTER

THESIS

Submitted in partial fulfillment of the requirements  
for the degree of Master of Science in Nuclear, Plasma, Radiological Engineering  
in the Graduate College of the  
University of Illinois at Urbana-Champaign, 2021

Urbana, Illinois

Master's Committee:

Dr. Madicken Munk  
Dr. Tomasz Kozlowski

# Abstract

Pebble-bed High Temperature Gas-Cooled Reactor (HTGR) designs present a unique modeling challenge. Pebble-bed reactors can have a variety of pebble compositions due to varying levels of burnup. In addition, the pebbles are mobile in the core — entering from the top and exiting through the bottom — and may fall in a haphazard arrangement. This work introduces a 20 MWth pebble-bed HTGR reactor design (which will be referred to as Sangamon20) that is representative of current pebble bed reactors, and investigates not only the neutronics of the base model, but the changes to core neutronics after making modifications to the simulation. These modifications include: heterogenous versus homogenous pebble centers, imposing a universal symmetry assumption, and changing the arrangement of pebble fuel compositions, using Serpent and Python. This is in support of the ultimate goal of this project: to establish a baseline source term and to determine what simplifications, if any, can be made in the model to strike a balance between computational cost and precision of the results. This is crucial for any future licensing effort, safety analysis, or accident analysis involving pebble-bed reactors. The model of Sangamon20 uses a random dispersal of seven different pebble compositions, each corresponding to a different burnup level. The heterogeneous tests compare  $k_{eff}$ ; thermal and fast flux profiles; and the neutron lethargy-adjusted energy spectra in the core, reflector, coolant, a random fresh, and a random discharge-burnup pebble. Shuffling and symmetry tests monitor changes to  $k_{eff}$  and the outgoing neutron current at the outer reflector boundary; the former because it is an important reactor physics parameter, and the latter because it can be used to find the anticipated neutron flux the Reactor Pressure Vessel (RPV) would experience. This informs the level of radiation damage one could expect the RPV to experience each year - which is useful from a design and safety perspective. Neither the symmetry test nor the shuffling test showed a major difference in either the  $k_{eff}$  or the outward neutron current at the outer edge of the reflector. This would suggest that there is no need to simulate all possible pebble placements to characterize a reactor. However, for the heterogeneous tests,  $k_{eff}$  differed by 4.45%, and the pebble spectra at certain higher energies disagreed by a factor of 2-4. A complete fuel isotopic composition at each burnup step is accessible at [37]. This thesis discusses select isotopic inventories of interest. These can be used to inform source term determination or spent fuel compositions.

# Acknowledgments

I'd like to thank Dr. Madicken Munk, my advisor, whose insight and experience was invaluable; and Professor Tomasz Kozlowski, my second reader for giving me their expertise. To Nathan Ryan of the Advanced Reactors and Fuel Cycles group, my tireless reviewer: thank you for all of your hard work.

I would also like to thank everyone else in the Advanced Reactors and Fuel Cycles group, past and present, for giving me their time, aid, and advice: Amanda Bachmann, Dr. Andrei Rykhlevskii, Ansh Chaube, Greg Westphal, Gwendolyn Chee, Mehmet Turkmen, Nataly Panczyk, Roberto Fairhurst, Sam Dotson, and Sun Myung Park.

Thank you to my family, for always believing in me; Trinket, for loving hugs; and Sara, without whom nothing in this project would have a good name.

This work is supported by the Nuclear Regulatory Commission Fellowship Program.

# Table of Contents

<b>List of Tables . . . . .</b>	<b>vi</b>
<b>List of Figures . . . . .</b>	<b>vii</b>
<b>List of Acronyms . . . . .</b>	<b>viii</b>
<b>Chapter 1 Introduction . . . . .</b>	<b>1</b>
1.1 Motivation . . . . .	1
1.2 Objectives . . . . .	2
1.3 Background . . . . .	3
1.3.1 The High Temperature Gas Cooled Reactor: Beginnings and Concepts . . . . .	4
1.3.2 Earliest Operational HTGRs . . . . .	5
1.3.3 Earliest HTGRs: Conclusion . . . . .	8
<b>Chapter 2 Literature Review . . . . .</b>	<b>9</b>
2.1 Computational Modeling and Software . . . . .	9
2.1.1 Serpent . . . . .	9
2.1.2 MCNP . . . . .	10
2.1.3 BEAU . . . . .	10
2.1.4 Fuel Modeling . . . . .	11
2.2 Modern HTGRs . . . . .	12
2.2.1 PBMR . . . . .	12
2.2.2 Next Generation Nuclear Plant (NGNP) . . . . .	14
2.2.3 HTR-10 . . . . .	14
2.2.4 Xe-100 . . . . .	15
2.2.5 Modern HTGRs: Conclusion . . . . .	15
<b>Chapter 3 Methodology . . . . .</b>	<b>16</b>
3.1 Modeling Particle and Pebble Dispersal . . . . .	16
3.2 Run Parameters and Conditions . . . . .	17
3.3 Single Pebble Depletion Model Geometry and Materials . . . . .	17
3.3.1 Fuel Composition Determination . . . . .	19
3.4 Sangamon200 . . . . .	20
3.5 Sangamon20 . . . . .	22
3.5.1 Graphite Reflector Thickness Determination . . . . .	22
3.5.2 Inner Core Volume Determination . . . . .	23
3.6 Heterogenization Tests . . . . .	26
3.7 Reactor Sensitivity to Pebble Locations and Symmetry . . . . .	26

<b>Chapter 4 Results . . . . .</b>	<b>28</b>
4.1 Fuel Isotopic Compositions . . . . .	28
4.2 Full-Core Control Model . . . . .	33
4.3 Effect of Homogenization . . . . .	40
4.4 Shuffling and Symmetry Tests . . . . .	51
4.4.1 Effects of Symmetry Assumption . . . . .	51
4.4.2 Effects of Pebble Shuffling . . . . .	53
<b>Chapter 5 Conclusion . . . . .</b>	<b>55</b>
5.1 Summary and Discussion . . . . .	55
5.2 Future Work . . . . .	56
<b>Appendices . . . . .</b>	<b>62</b>
A Image Difference and RGB Color . . . . .	62
B Symmetry Test . . . . .	63
C Shuffle Test . . . . .	74

# List of Tables

1.1	Helium Coolant Specific Activities in the AVR, reproduced from Table 2 in [14] — Results of experiments at the AVR Reactor by H.Gottaut and K.Krüger . . . . .	8
1.2	Pebble Dust Specific Activities, reproduced from Table 3 in [14] — Results of experiments at the AVR Reactor by H.Gottaut and K.Krüger . . . . .	8
3.1	Relevant Monte Carlo Parameters for Single Pebble and Sangamon Reactor Simulations . . . . .	17
3.2	Relevant Material Properties Used in Monte Carlo Simulations . . . . .	17
3.3	Pebble Parameters Used in Monte Carlo Simulations . . . . .	18
3.4	Particle Parameters Used in Monte Carlo Simulations . . . . .	19
3.5	Geometric and Internal Core Parameters in the Sangamon Reactors . . . . .	20
3.6	Shuffle Test Run Schemes . . . . .	27
4.1	Runtime and CPU Usage Between the Homogenized and Heterogenized Sangamon20 Models . . . . .	42
4.2	Symmetry Run Results Summary . . . . .	51
4.3	Shuffling Run Results Summary . . . . .	54
5.1	Symmetry and Shuffle Test Error Ranges, Average Values, and Uncertainty in the Associated Control Model Value . . . . .	55
2	Representation of Pebbles by Number of Passes in a 10 cm Square Rectangular Prism Surrounding an Image Difference Hotspot at Approximately $x = 11$ cm, $y = -56$ cm . . . . .	86
3	Representation of Pebbles by Number of Passes in a 5 cm Square Rectangular Prism Surrounding an Image Difference Hotspot at Approximately $x = 11$ cm, $y = -56$ cm . . . . .	86

# List of Figures

1.1	Side-View of Daniels et. al. (1955) Reactor Concept, from [44] . . . . .	4
1.2	Diagram of Coolant Flow in Daniels et. al. (1955) Concept, from [44] . . . . .	5
2.1	Diagram of fuel regions in an equilibrium PBMR core model . . . . .	13
3.1	Pebble Zones . . . . .	18
3.2	TRISO Particle Layers . . . . .	19
3.3	Geometry of the Single-Pebble Burnup Calculation for Sangamon20 . . . . .	20
3.4	Detector Placement Inside Reflector in Sangamon200 and Sangamon20 . . . . .	21
3.5	Outward Neutron Current versus Reflector Thickness . . . . .	23
3.6	Curve of possible height and radii that satisfy the volume requirements imposed by packing fraction(s) $\eta_{pf}$ . . . . .	25
3.7	Symmetry Test Run Layouts . . . . .	27
4.1	Serpent-Generated Mesh Figures of the Fission Rate and Thermal Flux for the Representative Single-Pebble at each Depletion Step . . . . .	28
4.2	Evolution of Safety Relevant Isotopic Concentrations in Pebbles of Sangamon20 over Six Six-Month Passes . . . . .	30
4.3	Geometry Cross Sections (left) and Thermal Flux(cold color map) and Fission Rate (hot color map) Meshes (right) for the Control Model of Sangamon20 . . . . .	34
4.4	Radial Thermal and Fast Flux Profiles along the X-Axis at the Mid-Plane in the Homogenized-Pebble Sangamon20. Black vertical lines at $\pm 90$ cm show the inner reflector boundary. . . . .	36
4.5	Axial Thermal and Fast Flux Profiles along the X-Axis at the Mid-Plane in the Homogenized-Pebble Sangamon20. Black vertical lines at $\pm 90$ cm show the inner reflector boundary. . . . .	36
4.6	Thermal Flux in xy Plane in Sangamon20: Homogenized Pebbles. The dotted line annotation marks the boundary between the active core and the graphite reflector. . . . .	38
4.7	Fast Flux in xy Plane in Sangamon20: Homogenized Pebbles. The dotted line annotation marks the boundary between the active core and the graphite reflector. . . . .	38
4.8	Lethargy Adjusted Neutron Flux Energy Spectrum in the Whole-Core for the Homogenized-Pebble Sangamon20 . . . . .	39
4.9	Lethargy Adjusted Neutron Flux Energy Spectrum in the Each Pebble Burnup and Coolant for the Homogenized-Pebble Sangamon20 . . . . .	40
4.10	Full Core Using Heterogenized Pebbles . . . . .	41
4.11	Radial Thermal and Fast Flux Profiles along the X-Axis at the Mid-Plane in the Heterogenized-Pebble Sangamon20. Black vertical lines at $\pm 90$ cm show the inner reflector boundary. . . . .	42
4.12	Axial Thermal and Fast Flux Profiles along the Z-Axis at the Centerline in the Heterogenized-Pebble Sangamon20. Black vertical lines at $\pm 90$ cm show the inner reflector boundary. . . . .	43
4.13	Thermal Flux in xy Plane in Sangamon20: Heterogenized Pebbles. The dotted line annotation marks the boundary between the active core and the graphite reflector. . . . .	43
4.14	Fast Flux in xy Plane in Sangamon20: Heterogenized Pebbles. The dotted line annotation marks the boundary between the active core and the graphite reflector. . . . .	44

4.15 Lethargy Adjusted Neutron Flux Energy Spectrum in the Whole-Core for the Heterogenized-Pebble Sangamon20 . . . . .	45
4.16 Lethargy Adjusted Neutron Flux Energy Spectrum in the Each Pebble Burnup and Coolant for the Heterogenous-Pebble Sangamon20 . . . . .	45
4.17 Relative Difference in Radial Thermal and Fast Flux Profiles Between Cores Using Homogenized and Heterogenized Pebbles . . . . .	46
4.18 Relative Difference in Lethargy Adjusted Neutron Flux Energy Spectra Between Cores using Homogenized and Heterogenized Pebbles . . . . .	48
4.19 Sensitivity Analysis: $\frac{1}{6}$ Symmetry Using the Portion of the Core Between $0^\circ - 60^\circ$ . . . . .	52
4.20 An Image Generated by Subtracting 4.19b from 4.3b. . . . .	53
 1 An Example of RGB Color Values . . . . .	63
2 Sensitivity Analysis: $\frac{1}{6}$ Symmetry Using the Portion of the Core Between $60^\circ - 120^\circ$ . . . . .	64
3 An Image Generated by Subtracting Figure 2b from Figure 4.3b. . . . .	65
4 Sensitivity Analysis: $\frac{1}{6}$ Symmetry Using the Portion of the Core Between $120^\circ - 180^\circ$ . . . . .	66
5 An Image Generated by Subtracting Figure 4b from Figure 4.3b. . . . .	67
6 Sensitivity Analysis: $\frac{1}{6}$ Symmetry Using the Portion of the Core Between $180^\circ - 240^\circ$ . . . . .	68
7 An Image Generated by Subtracting Figure 6b from Figure 4.3b. . . . .	69
8 Sensitivity Analysis: $\frac{1}{6}$ Symmetry Using the Portion of the Core Between $240^\circ - 300^\circ$ . . . . .	70
9 An Image Generated by Subtracting Figure 8b from Figure 4.3b. . . . .	71
10 Sensitivity Analysis: $\frac{1}{6}$ Symmetry Using the Portion of the Core Between $300^\circ - 360^\circ$ . . . . .	72
11 An Image Generated by Subtracting Figure 10b from Figure 4.3b. . . . .	73
12 Shuffle Analysis: Run 1 . . . . .	74
13 An Image Generated by Subtracting Figure 12b from Figure 4.3b. . . . .	75
14 Shuffle Analysis: Run 2 . . . . .	76
15 An Image Generated by Subtracting Figure 14b from Figure 4.3b. . . . .	77
16 Shuffle Analysis: Run 3 . . . . .	78
17 An Image Generated by Subtracting Figure 16b from Figure 4.3b. . . . .	79
18 Shuffle Analysis: Run 4 . . . . .	80
19 An Image Generated by Subtracting Figure 18b from Figure 4.3b. . . . .	81
20 Shuffle Analysis: Run 5 . . . . .	82
21 An Image Generated by Subtracting Figure 20b from Figure 4.3b. . . . .	83
22 Shuffle Analysis: Run 6 . . . . .	84
23 An Image Generated by Subtracting Figure 22b from Figure 4.3b. . . . .	85

# List of Abbreviations

ACE	A Compact ENDF
AVR	Arbeitsgemeinschaft Versuchsreaktor
BEAU	Burnup Equilibrium Analysis Utility
BCC	Body Centered Cubic
BCT	Body Centered Tetragonal
BISO	Bi-Structural Isotropic
CRP	Coordinated Research Project
CSG	Constructive Solid Geometry
DEM	Discrete Element Method
EFPD	Effective Full Power Days
ENDF	Evaluated Nuclear Data Format
FCC	Face Centered Cubic
GIF	GEN IV International Forum
HCP	Hexagonal Close Packed
HTG-SMR	High Temperature Gas-Cooled Small Modular Reactor
HTGR	High Temperature Gas-Cooled Reactor
HTR	High Temperature Reactor
HTTR	High Temperature Test Reactor
IAEA	International Atomic Energy Agency
INL	Idaho National Laboratory
LEU	Low-Enriched Uranium
LWR	Light Water Reactor
MCNP	Monte Carlo N-Particle transport
MOL	Middle Of Life
NGNP	Next Generation Nuclear Plant

ORNL	Oak Ridge national Laboratory
OTTO	Once Through Then Out
PB-FHR	Pebble-Bed Fluoride High Temperature Reactor
PBMR	Pebble Bed Modular Reactor
RGB	Red-Green-Blue
RMC	Reactor Monte Carlo
RPV	Reactor Pressure Vessel
RSA	Random Sequential Addition
RUG	Random Universe Geometry
SBO	Station Black-Out
SC	Simple Cubic
SMR	Small Modular Reactor
THTR	Thorium High Temperature Reactor
TRISO	Tri-Structural Isotropic
UAM	Uncertainty Analysis in Modeling
UCO	Uranium Oxycarbide
VHTRC	Very High Temperature Reactor Critical Assembly
VSOP	Very Superior Old Programs

# Chapter 1

## Introduction

### 1.1 Motivation

The effects of climate change increase in severity every year. From 1980 to present, the global temperature anomaly — defined as the difference between the current average global temperature and the average temperature from 1951 to 1980 — has steadily increased to  $1.05^{\circ}\text{C}$  [47, 26]. One factor contributing to this global climate change is the use of fossil fuels, which emit greenhouse gases. In relatively recent years, there has been a growing push for energy technologies that do not rely on fossil fuels, such as nuclear power. While nuclear technology is currently in use across the world, many of these reactors are facing closure as their licenses run out. In turn, energy companies may be forced to return to fossil fuels to supply the baseload power that was once supplied by nuclear.

The next generation of nuclear reactor technology — Generation IV — uses advanced materials and reactor designs. These provide a myriad of benefits, including features such as passive safety systems, or improved fuel utilization. There is an international effort to support the development of these reactors, led by the GEN IV International Forum (GIF). GIF identified eight goals the design of Gen IV reactors should fulfill, encompassing improvements to sustainability, economics, safety, and non-proliferation [13].

One such class of Gen IV reactor is the High Temperature Gas-Cooled Reactor (HTGR) with which this thesis is concerned. HTGRs tend to be cooled with a non-reactive gas — usually helium, use graphite as a moderator, and have a thermal neutron energy spectrum. HTGRs can have a variety of fuel forms, including pebble fuel. Pebble-type fuels consist of a sphere of graphite, approximately the size of a billiard ball, embedded with tri-structural isotropic (TRISO) particles. TRISO-based fuels are popular in Gen IV reactor design because they are robust, that is, they are not prone to cracking and are stable at higher temperatures than standard Light Water Reactor (LWR) fuel. This is advantageous to long-term spent fuel safety (though it does make reprocessing much more difficult). Pebble-type fuels in particular can be refueled online, which reduces the need for planned shutdowns. However, HTGRs are typically very large designs, which can be prohibitively costly to build and operate, or simply unneeded for small-scale projects.

To reduce size — and consequently costs — another class of reactor was designed: the Small Modular Reactor

(SMR). These reactors are smaller than the conventional LWR. They usually generate around 200-300 MWth, and are small enough to be shipped in a standard shipping truck or train (which are generally around 50 feet in length). Owing to their small size, they are also easier and cheaper to manufacture, and theoretically reach  $n^{th}$  of a kind faster. One can deploy an SMR in a variety of new settings, such as isolated towns or work sites, or station many together in one location to fill the role of a single larger reactor.

There exists a class of reactor even smaller than the SMR: the microreactor. Microreactors generally have a capacity of 70 MWth or less and could be deployed in areas only needing a small amount of power, used for research and testing, or used to supply heat for other industrial processes, such as producing hydrogen. Smaller reactors, such as SMRs or microreactors, have a few inherent safety benefits over their larger cousins, prompting their development. The reduced size of the reactor pressure vessel (RPV) additionally allows for smaller active cooling loops. In the case of a Station Black-Out (SBO), when the gas blowers cannot actively circulate the coolant, passive systems can rely on natural convection and surface heat transfer to remove decay heat. Under normal operation, supplementary fans and surface coolers can also aid heat removal [36].

This work created a 200MWth pebble-bed high-temperature gas-cooled SMR model based on existing designs. We call this 200MWth reactor the Sangamon200. Sangamon200 is meant to reflect a "classic" — if generic — Gen IV HTGR. A smaller 20MWth design was created by scaling down the Sangamon200 model. The 20MWth model, hereafter referred to as Sangamon20, is a microreactor counterpart to the 200MWth reactor. Sangamon20 is the main focus for all subsequent testing and analysis, and it is simplified to provide a foundation for investigating core neutronics and fuel isotopes. No additional features beyond the randomness and heterogeneity of the pebbles inside are modeled, as fuel perturbations are the focus of this study. In Section 1.2, I will discuss the objectives of these designs, and then in Section 1.3 I will provide a brief history of HTGR development.

## 1.2 Objectives

This thesis briefly describes a 200 MWth pebble-bed HTGR SMR, inspired by concepts from the PBMR [52] and X-Energy [17] reactors, henceforth named Sangamon200. We established the larger reactor as a baseline for the scaled-down 20 MWth model, Sangamon20, that is the focus of the analysis in Chapter 4.

For a reactor to be licensed, one must be able to show it is safe. This will require a combination of computational and experimental work, and we will focus on the former. Computational models allow researchers and reactor designers to model accident scenarios or test models without an expensive or intensive experimental setup. However, any high fidelity full-core pebble-bed reactor model will require significant computational resources to produce reliable results. In order to make running such models less demanding, it is sometimes necessary to make

simplifications that are not reflected in a real-world core. A pebble-bed reactor has multiple layers of heterogeneity; the locations of the TRISO particles in the pebbles are randomly generated as well as the location of the fuel pebbles in the core. Pebble location aside, there are seven fuel compositions also distributed uniformly and randomly throughout the core. As said before, Sangamon20 uses random pebble dispersal. This means that there are a theoretically infinite number of Sangamon20 designs that *could* exist, with only pebble locations changing. This randomness presents a design and licensing challenge — even if one can demonstrate a particular permutation of a given pebble bed reactor is safe, is that model sufficient to prove all variations are? To help answer this question, a test was performed that "shuffled" the burnup levels of fuel in the pebbles, changing which burnup went into which pebble. This has been named the shuffle test (see: Section 3.7, Table 3.6), and the model variations are compared to the original "control" core model. Another source of variation in the model is using a symmetry assumption. When a symmetry condition is used, Serpent takes a user-defined fraction of the core (for this thesis,  $\frac{1}{6}$ ) and uses it to represent the entire core. Assuming a symmetry condition may make the core easier to model, but it also introduces error. One can imagine that if this user-defined region happens to have a higher fraction of a particular burnup of pebbles than the rest of the reactor, the results wouldn't accurately reflect the whole-core. To investigate the potential effects of this, a series of simulations running the Sangamon20 model while utilizing a radial symmetry condition were analyzed (henceforth called the symmetry test, see Section 3.7, Figure 3.7). These tests will not only show the impact on this specific design, but also provide insight on the effects such simplifications may have on other pebble-bed models. Additionally, the isotopic compositions that were generated and implemented can be used in source term, spent fuel, and safety analysis.

### 1.3 Background

While HTGRs and pebble bed reactors have had a recent resurgence in interest and research, they are an older concept. The following subsections describe early HTGR concepts, reactors, and how they contributed to our present knowledge of HTGRs. Even though experimental data collection and analysis is not the goal nor focus of this thesis, the previous empirical data and experience informs and generates confidence in modern-day HTGR design and modeling, which is the foundation for this work. Additionally, as there have not been many modern-day HTGR designs that have come to fruition, these early experimental and commercial reactors provide us with valuable insight for future modeling efforts. The remainder of this chapter will focus on a few of these early (pre-1970) designs, such as the early pebble bed or pebble-pile designs from Dr. Farrington Daniels, and the AVR, Dragon, and Peach Bottom 1. Other notable HTGRs that came online after 1970, such as the 1976 Fort St. Vrain reactor (a 824 MWth prismatic HTGR [53]), the 1985 Thorium High Temperature Reactor (THTR) (a 300 MWth pebble bed [4]),

and the 1998 High Temperature Test Reactor (HTTR) (a 30 MWth prismatic HTGR [43]) are not discussed in great detail here.

### 1.3.1 The High Temperature Gas Cooled Reactor: Beginnings and Concepts

HTGRs are a prominent Generation IV reactor design which often uses helium as a coolant, and graphite as a moderator. Their fuel form uses TRISO particles, which consist of a small kernel of fuel, less than half a millimeter across, surrounded by layers of carbon and silicon carbide to protect the fuel kernel and prevent the leakage of radioisotopes. Fuel elements are made by embedding these TRISO particles in graphite. In prismatic HTGRs, the graphite is in the shape of hexagonal columns. In pebble-bed reactors, the graphite is in the shape of a sphere, often six [cm] in diameter. These pebbles are mobile in the core, and in the case of gas-cooled reactors, will enter from the top and exit at the bottom.

Preliminary concepts for a gas-cooled reactor existed as early as 1944, in a report titled "Suggestions for a High-Temperature Pebble Pile" [12]. Farrington Daniels and Oak Ridge National Laboratory (ORNL) established the most basic characteristics of the HTGR. The choice of helium for coolant, graphite for moderator, the direct gas turbine cycle, and the use of uranium or thorium carbides for fuel all came from the work of Daniels et al [44]. However, this initial suggestion was still vastly different from the HTGR designs we recognize today.

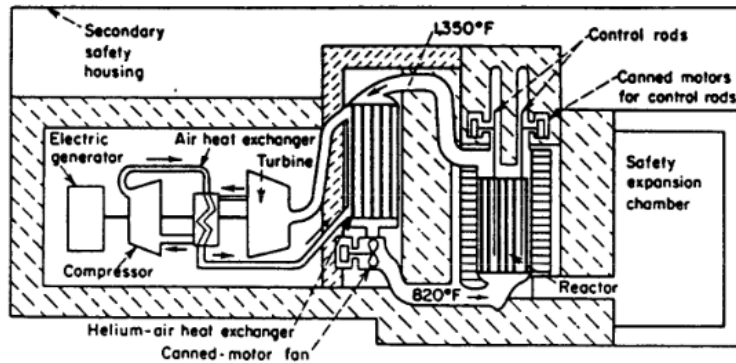


Figure 1.1: Side-View of Daniels et. al. (1955) Reactor Concept, from [44]

Figures 1.1 and 1.2 show a later design from 1955 by Daniels et al, which is more closely related to modern designs. A key difference between the Farrington Daniels et al designs and modern HTGRs is the fuel form. While modern designs use TRISO particles embedded in graphite, the Daniels et al design used solid graphite blocks, with channels for both coolant and fuel. Within the fuel channels, fuel loaded in either a pellet or cartridge form, both a mixture of 10% uranium dicarbide and graphite powder. In addition to these fuel channels, the design included an outer ring of graphite reflector in which used thorium to breed  $^{233}U$ . Control rods were of a boron-containing molybdenum. Steel wires that would melt in the case of an accident held more control rods above the core, and

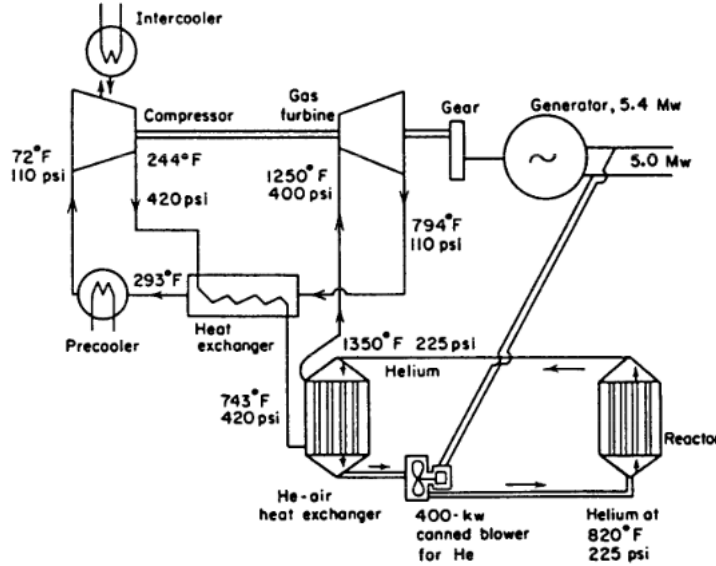


Figure 1.2: Diagram of Coolant Flow in Daniels et. al. (1955) Concept, from [44]

would drop the safety rods in case of an accident [44].

### 1.3.2 Earliest Operational HTGRs

The earliest operational HTGRs came online in the 1960s. These early reactors are discussed in the sections below: Dragon, operating in the UK; Peach Bottom 1, in the US; and the AVR, from Germany. Of these three, only Peach Bottom 1 was a commercial-scale demonstration - the others, Dragon and the AVR, were experimental reactors. Of particular interest is the AVR, which is the only pebble-bed reactor of the three. Experiments in the AVR not only provided empirical data on the inner-core temperatures inside the AVR core, but also tested accident response, and observed a "pebble dust" that accumulated in the AVR over its operation — including its activity.

#### Dragon

The Dragon prismatic HTGR was a test reactor operated in Winfrith, UK, by the Organization for Economic Co-operation and Development from 1964 to 1975, making it the oldest of the reactors discussed in this chapter. It operated with inlet and outlet temperatures of 350 °C and 750 °C, respectively, and at 20MWth [5]. Dragon's main purpose was to test reactor materials, with an emphasis on fuels. It originally used uranium and thorium as fuel but switched to a purely uranium-based fuel with a lower enrichment later in life due to concerns over availability. The fuel elements themselves were similar in shape to the Daniels et al design: hexagonal prisms with fuel rod channels.

Contrary to the fuel philosophy seen today, Dragon originally allowed fission products released from fuel elements into the circulating helium coolant. The fission products were then purged from the helium. However,

Dragon later switched to a coated-particle fuel when it became clear that having such fission product releases were difficult to manage [44], especially because it would have required large filters to trap fission products.

### **Peach Bottom 1**

Peach Bottom 1 operated from 1966 to 1974, by the Philadelphia Electric Company and was located in Delta, Pennsylvania [5]. It was the first operational HTGR in the US, and the first to produce electric power. It was slightly larger than Dragon, at a nameplate capacity of 115 MWth/40MWe and a slightly lower operating temperature range at 327°C to 700°C inlet to outlet [5]. Like Dragon, Peach Bottom 1 was a prismatic reactor; however, Peach Bottom used coated uranium and thorium carbide particles coated by a single layer of pyrolytic carbon. However, after multiple fuel failures, Peach Bottom upgraded to bistructural isotropic, or BISO, fuels by adding an additional layer of pyrolytic carbon. Peach Bottom would later upgrade the fuel once again by adding a silicon carbide layer, forming TRISO particles [5]. One operational benefit of upgrading to TRISO particles from BISO particles was that the superior fission product retention meant that Peach Bottom 1 could remove the helium purging systems and continue to house safe operation. In addition to the inner fuel region, Peach Bottom, like the Daniels et al design, bred  $^{233}U$  in an outer region using thorium.

Beyond changing the number and materials for fuel coatings, the experiences in Peach Bottom 1 helped to develop HTGR fuel elements. Operators saw that they could dilute the fuel with graphite moderating material more so than other diluents. This has the advantage of saving fuel material, improving heat transfer, and reducing radiation damage. Additionally, operational experience showed that, in order to prevent the creation and buildup of  $^{236}U$  and  $^{237}Np$ , which are neutron poisons, the  $^{235}U$  and  $^{233}U$  should be kept separate [44]. In the end, however; Peach Bottom 1 closed after the Philadelphia Electric Company determined its size made it no longer economically viable.

### **AVR**

The Arbeitsgemeinschaft Versuchsreaktor (AVR) was an experimental pebble-bed reactor operated in and by the Jülich Research Center (in Jülich, Germany) from 1967 to 1988. It had a capacity of 46 MWth/15MWe, with inlet and outlet temperatures of 275°C and 950°C [5]. The AVR used a combination of uranium and thorium fuels, though it began with bi-structural isotropic (BISO) particles. The core held around 100,000 graphite pebbles, only a third of which had fuel in them.

The AVR housed many experiments that improved our body of knowledge on HTGR technology. During the first few years of its life, the goal of the AVR was to demonstrate that it was a reliable technology — that the reactor could operate safely, that they could control the core power and temperatures, safely shutdown, and remain sub-critical

for long periods of time. After this initial period, the AVR shifted focus to include new experiments including: observing core temperature distributions, accident analysis, and fuel testing. The AVR also shifted from highly enriched to low enriched fuel over time, which caused a variation in fuel pebble compositions, on top of the range of compositions inherent to a multi-pass pebble cycle due to varying burnup.

The AVR also provided data to validate simulations of pebble-bed reactors, and conducted an experiment to better characterize the radial distribution of temperatures in the core [14]. Operators loaded a number of marked pebbles into the core, each housing a series of wires that would melt at a certain temperature, the lowest being 655°C, the highest 1280°C. Those conducting the test tracked pebble location using flow data, and examined them after they were ejected to determine what temperatures the pebbles experienced. Despite the outlet temperature being 950°C, multiple pebbles experienced a temperature greater than or equal to the 1280°C maximum temperature in the melt wires. The results noted that these pebbles went through a zone with a spike in local power density, which could account for the temperature spike [14].

The AVR also demonstrated the inherent safety of HTGR reactors in accident scenarios by purposefully causing failures of the active cooling system. In the first, the coolant blowers were shutoff, and no shutdown rods inserted, while operating at full power. The operators additionally shut the main circuit valves to prevent natural circulation to regions outside the active core. Overall, the changes to core temperatures were unremarkable. The hottest regions cooled, while the coldest regions warmed up. Additionally, due to negative temperature feedback coefficients, the reactor power immediately declined in response to the transient event. The temperature slowly rose to 2 MW again over 24 hours, leveling out around 300 kW. A further test provided data on loss of coolant and depressurization accidents. As before, the core temperature changes were unremarkable. The upper core region cooled, while the lower, originally cooler core region slowly rose in temperature. The experiment's thermal data helped validate HTGR computer models by providing a real-world comparison. This meant that the results to aid in the analysis of other HTGRs [14].

Beyond accident safety, the AVR allowed for testing and demonstration of the safety qualities of TRISO and BISO fuel elements; especially relating to high temperature tolerance, and fission product retention. Initial tests used BISO based pebbles, then later transitioned to TRISO, then to low-enriched-uranium (LEU) TRISO pebbles. The TRISO-LEU pebbles had good fission product retention compared with their BISO-based predecessors, based on the activity of samples taken from the circulating helium. Beyond radioisotopes being directly released into the coolant gas, the AVR also showed that in order to accurately characterize the source term of an HTGR pebble bed reactor, one must take the dust from the pebbles into account. Dust from the pebbles bumping and scraping against each other deposited on reactor surfaces in the primary loop. Sixty kg of dust had accumulated by the end of the reactor's life, which averages to 3 kg of dust each year. Measurements of specific activity in the dust showed

that the activities of  $^{137}Cs$ ,  $^{134}Cs$ ,  $^{131}I$ ,  $^{90}Sr$ , and  $^{60}Co$  were on the order of  $10^{-01}$  to  $10^{02} \frac{Bq}{g}$  (see Table 1.1 and Table 1.2). Even though relatively little dust accumulates, the activity of this dust is fairly high, especially compared to the activity of the coolant gas [14]. This dust can become mobile in an accident scenario, potentially being released into the environment, or inhaled.

Table 1.1: Helium Coolant Specific Activities in the AVR, reproduced from Table 2 in [14] — Results of experiments at the AVR Reactor by H.Gottaut and K.Krüger

Isotope	Specific Activity in Primary Coolant Gas [ $\frac{Bq}{m^3}$ ]
$\Sigma$ Fission noble gas	$4.6 \times 10^{08}$
$^3H$	$3.7 \times 10^{07}$
$^{14}C$	$1.9 \times 10^{07}$
$^{137}Cs$	$3.0 \times 10^{02}$
$^{131}I$	$5.2 \times 10^{02}$
$^{110m}Ag$	$4.9 \times 10^{01}$
$^{90}Sr$	$2.0 \times 10^{02}$
$^{60}Co$	$1.0 \times 10^{01}$

Table 1.2: Pebble Dust Specific Activities, reproduced from Table 3 in [14] — Results of experiments at the AVR Reactor by H.Gottaut and K.Krüger

Isotope	Specific Activity in Dust [ $\frac{Bq}{g}$ ]
$^{137}Cs$	2 - 96
$^{134}Cs$	0.7 - 27
$^{131}I$	0 - 3
$^{110m}Ag$	0.1 - 43
$^{89}Sr$	0.6 - 42
$^{90}Sr$	19 - 363
$^{60}Co$	0.2 - 8

### 1.3.3 Earliest HTGRs: Conclusion

The three earliest operational HTGRs have been discussed in Section 1.3.2. Even though Dragon and Peach Bottom 1 are not pebble-bed reactors, they still used TRISO particle fuels, and still provided experience in HTGR operation and management. The AVR, meanwhile, was a pebble-bed reactor, and not only provided general HTGR experience, but also provided pebble-fuel specific data, such as on pebble dust accumulation and activity. The experience from these reactors helped to inform the design of modern HTGRs, especially in regard to providing experimental data to validate computational models against.

# **Chapter 2**

## **Literature Review**

### **2.1 Computational Modeling and Software**

The subsections of section 2.1 focus on more recent modeling efforts in the pebble bed, HTGR, and SMR/microreactor areas. The first sections provide highlights of some relevant work in specific software, including Monte Carlo N-Particle transport (MCNP) [54] and Burnup Equilibrium Analysis Utility (BEAU) [9] (see Subsection 2.1.2). The later sections discuss an analysis of the effects that the pebble-distribution lattice has on the reactor core as a whole. These will set up the available tools to analyze the reactors summarized in Section 2.2, which includes a description of the Pebble Bed Modular Reactor (PBMR), Next Generation Nuclear Plant (NGNP), Xe-100, and HTR-10 reactors. These descriptions will be supplemented with a discussion of modeling experience or progress achieved by the respective reactor design teams.

#### **2.1.1 Serpent**

Serpent is a Monte Carlo code developed out of VTT [28]. Serpent uses Constructive Solid Geometry (CSG) to allow user-defined, complex geometries. This includes particles, lattices, and nested components [28]. TRISO particles have locations defined by the three-dimensional coordinates for their centers and their outermost radius. To generate thousands or even millions of random particle locations — Serpent has a built-in particle dispersal routine. Because particle dispersal is relevant to this modeling effort, the mechanics of the dispersal routine are discussed in greater detail in the Methods Chapter (see Chapter 3).

A 2016 study by Friederike Bostelmann et al compared the Very High Temperature Reactor Critical Assembly (VHTRC) [33] benchmark (originally made by the International Atomic Energy Agency (IAEA) Coordinated Research Project (CRP) on Uncertainty Analysis in Modeling (UAM)) to computational models of the VHTRC made in Serpent and SCALE [6]. The VHTRC is a single hexagonal fuel assembly made of graphite, with holes for fuel pins. Normally, a fuel-pin based assembly would not be of interest, however; the VHTRC fuel rods are composed of a graphite in which BISO particles have been uniformly distributed, and so it still has the complexities of particle-based fuels. Friederike et al makes use of two Serpent models — one with a random dispersal and one with a lattice arrangement

of BISO particles in the fuel pins. The SCALE model does the same. In general, Serpent had fairly good agreement with the experimental data in criticality calculations (less than 50 pcm), while SCALE 6.1.2 models differed from the Serpent model by as much as 150 pcm. SCALE 6.2b4, which was in beta at the time, had a disagreement of less than 60 pcm to the Serpent model [6].

### 2.1.2 MCNP

MCNP, like Serpent, is a Monte Carlo transport code. There has been significant work in MCNP to aid HTGR modeling. A 1996 effort developed a new sampling method for particle placement in Monte Carlo to be used in MCNP, which would answer the difficulties of modeling two or more types of pebble in a single reactor. Its creators dubbed the version of MCNP that used the sampling algorithm as MCNP-BALL [31]. After testing by performing isotopic inventory and criticality calculations the MCNP-BALL code results were accurate to 0.2% [31].

An additional look into MCNP HTGR simulations examined the ability to create what would normally be a stochastic geometry with a uniform design. Specifically, it used a body-centered-tetragonal (BCT) and hexagonal close pack (HCP) lattice for the TRISO particles. Defining pebble and particle locations in this way is often easier to define in the model, and requires no secondary utility to generate the particle locations randomly. However, this regular arrangement doesn't reflect reality, and can cause pebbles to be cut-off, rather than having their locations conform to the boundaries of the container. For low packing fractions the particles are far enough apart that the differences between two lattice structures are insignificant. In smaller cores, with strong reflectors, the differences between the pebble packing lattices were more significant. Additionally, completely homogenizing the coating of the TRISO particles — blending them with the graphite matrix — lowered  $k_{eff}$  by as much as 0.20%. For methods using less dramatic homogenization methods, such as blending the four TRISO coatings into one uniform layer, the computational load decreased (due to the simpler geometry definitions), and the results were marginally (less than 0.05%) different from the 4-coating TRISO particle [24].

### 2.1.3 BEAU

Beyond steady-state codes such as Serpent and MCNP, burnup calculation and fuel composition are also of importance. Burnup calculations are required for determining the isotopic composition of fuel, which is a necessity in source-term determination and analysis. Burnup Equilibrium Analysis Utility (BEAU) is a Python-based coupling software that combines either MCNP5 or Serpent with ORIGEN2 [11], using new interface inspired by the MOCUP [3] software named `mocup.py` [9]. `Mocup.py` takes the output files from an MCNP5 or Serpent simulation, and turns them into an object for aiding in depletion simulations. BEAU is for reactor and fuel depletion analysis and finding the maximum burnup equilibrium. It was benchmarked against results for a pebble-bed HTGR in PEBBED [48] and

VSOP [40]. A lattice of mixed-burnup pebbles (corresponding to passes through the core) was defined according to the benchmark definitions for the core, pebbles, and TRISO particles [9].

BEAU models depletion and multiple burnup states for a continuously refueled pebble bed reactor [9]. It uses the novel multiple burnup state method (MBSM) to do so, which improves on most full-core pebble bed computational methods by including all burnup states for a pebble rather than homogenizing them into a representative average pebble.

Though the benchmark also included a test of a Once Through Then Out (OTTO) fuel cycle. BEAU was found to agree fairly well with PEBBED and VSOP in calculating the equilibrium  $k_{eff}$ , burnup, and the isotopic concentrations of uranium and plutonium. However, BEAU consistently under-predicted the isotopic concentrations of  $^{244}Am$  and  $^{155}Gd$  by an order of magnitude [9].

BEAU aided in the design of the Mark-1 pebble bed fluoride high temperature reactor (PB-FHR [9]). The model of the Mark-1 PB-FHR handles pebble locations using a face-centered cubic (FCC) lattice in which all burnup states corresponding to a pass through the core are present in the lattice.

#### 2.1.4 Fuel Modeling

A more general study than the parametric PB-FHR study using BEAU examined the effects of pebble packing on the core neutronics in an HTGR [50]. Rather than model a full core, the study created a unit cell as a reference. The study considers body centered cubic (BCC) and hexagonal close-packed (HCP) lattice unit cells. Instead of using a variety of compositions to represent an equilibrium, middle-of-life (MOL) core, the study used an enrichment of 9.6% — lower than the often-used 15% for fresh HTGR pebble-fuel — for all pebbles. For each lattice configuration, tests varied the fuel/moderator (F/M) ratio, and examined the effects on core neutronics and isotopic compositions. The analysis showed no significant difference between BCC and HCP cells. The study determined it would be difficult to select a truly 'optimal' energy spectrum for minimizing the accumulation of particularly harmful fission products. The authors concluded that F/M ratios less than 1/1 favor reducing actinide inventories, while ratios greater than 1/1 can reduce the generation of fission products that would corrode the layers of the TRISO fuel.

Earlier work on HTGRs by General Atomics determined the composition of discharged thorium/uranium prismatic fuel elements. The study assumed fuel recycling to complement the proposed breed/burn fuel cycle. Additionally, the fuel cycle assumes the reactor can start with an initial feed material of 93%  $^{235}U$ , which is currently infeasible due to IAEA restrictions [15]. While the Sangamon20 is not a prismatic reactor the General Atomic studies help to inform the isotopic compositions of fuel that has reached its end burnup, and provides a point of reference.

## 2.2 Modern HTGRs

The following discusses more recent HTGR designs, which are the inspiration for Sangamon200 and Sangamon20. These modern designs were chosen so that the two Sangamon models more accurately reflect designs that may be deployed in the future.

### 2.2.1 PBMR

The PBMR is a South African pebble bed HTGR design. While it did not ultimately make it to construction, its design has offered invaluable insight to later HTGR pebble bed designs. The PBMR is heavily based on the German High Temperature Reactor (HTR) design, and has a nameplate thermal power of 400 MW, with inlet-outlet temperatures of 500 °C to 900 °C. It is a modular design, with each unit containing a graphite moderated, helium-cooled-core housed in a steel pressure vessel. In accident scenarios, the PBMR would rely on passive safety features using conduction and convection to provide cooling.

Each core unit would hold around half a million pebbles, which used LEU fueled TRISO particles as the fuel form. These TRISO particles are pressed into a 2.5 [cm] radius graphite sphere, which then has an additional 0.5 [cm] thick layer of graphite pressed around it, to form a 3.0 [cm] radius pebble. The pebbles would undergo a six-pass cycle to reach a target end burnup of  $92,000 \left[ \frac{MWd}{tU} \right]$  [52].

As part of the design process, multiple 400 MWth PBMR computational models underwent development and testing. An early version using MCNP5 simplified the fuel by assuming a pebble enrichment of 9.6 wt%. It also used a BCC lattice for pebble positions. Its calculated  $k_{eff}$  differed from previous MCNP4b results by as much as 1,315 pcm when the model explicitly modeled the bottom cone-shaped regions of the reactor as opposed to a flat surface approximation [25].

An improved design modeled an older VSOP model more closely. A full-core model used a cubic array to map TRISO particles inside the pebbles, while an HCP lattice defined pebble locations [2]. As an improvement on previous iterations, it adds back in the fuel regions from the VSOP model, which tracks pebbles in channels and axial layers to simulate their movement through the core. These layers are modeled in the simplified scheme shown in Fig 2.1.

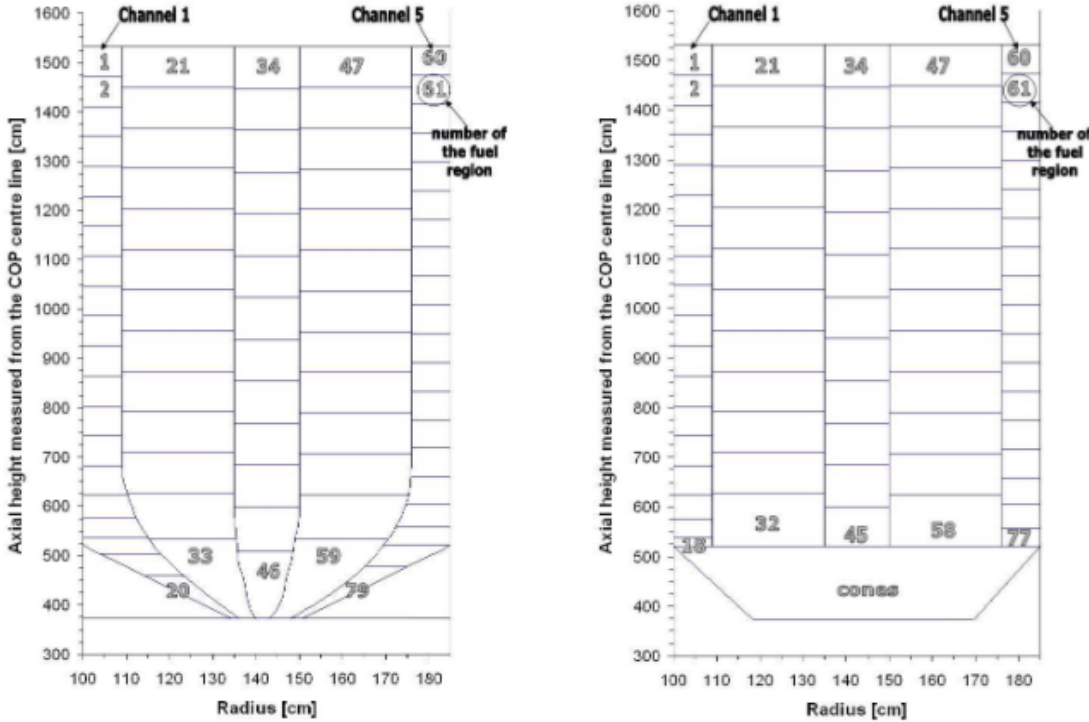


Figure 2.1: Diagram of fuel regions in an equilibrium PBMR core model, reproduced from [2]. Axial fuel zones defined for use in MCNP model validation (right) against a previous VSOP model (left).

To simplify, the different pebble burnups in each region are averaged. This study also investigated the effects of different pebble packing arrangements, but rather than use a full-core, a representative one-meter cube of pebbles defines a reference model. The study tested random, HCP, BCC, and FCC at packing fractions of 0.542 and 0.61. It found that across identical packing fractions, differences in reactivity were less than 350 pcm, though  $k_{eff}$  values differed by several standard deviations [2].

A separate study by Adem et al performed criticality and burnup calculations using MCNP5 and MONTEBURNS 2.0. It used an averaged 9.6% enriched fuel to simulate an equilibrium core [1]. It tested three pebble arrangements: a BCC lattice with a packing fraction of 0.68, a random arrangement with a packing fraction of 0.61, and a simple cubic (SC) lattice with a packing fraction of 0.52. The initial  $k_{eff}$  were similar: 1.2395, 1.2357, and 1.2223, respectively. However, the effective full power days (EFPDs) and end of life burnup required to reach an end  $k_{eff}$  of 1.02 differed considerably. BCC required 1200 EFPDs and ended at 99,000  $\frac{MWD}{T}$ , the random arrangement ended on 1000 EFPDs and a burnup of 92,000  $\frac{MWD}{T}$ , and the SC lattice required 800 EFPDs and achieved a final burnup of 86,000  $\frac{MWD}{T}$  [1]. However, for the random pebble arrangement, which was used to validate the model, the disagreement in excess reactivity was approximately 14%.

Finally, a study using VSOP focused on possible power peaking and the potential consequences of hot spots [35] from fresh pebbles "lumping together". To test this, a mass of fresh pebbles were purposefully introduced in the

fuel region corresponding to the peak power. Even for a very large cluster of fresh pebbles, maximum fuel power only increased by 16%. However, the volumetric power density increased from  $11.32 \frac{MW}{m^3}$  to  $18.66 \frac{MW}{m^3}$  [35]. The authors noted that this scenario is highly unlikely — the region of highest power is three meters into the core, by which point fresh pebbles would've undergone fission and would have some fission products. This is in addition to the already accidental loading of over one thousand fresh pebbles at once.

### **2.2.2 Next Generation Nuclear Plant (NGNP)**

Like the PBMR, the NGNP did not make it to construction though it provides many insights to our design of HTGRs. The NGNP project down selected its design choices to two reactors — a prismatic HTGR and a pebble-bed HTGR. While the NGNP project eventually opted for a prismatic HTGR design due to reasons related to pebble costs, studies noted that, technologically speaking, there was no inherent advantage or disadvantage between the two technologies [22]. Another project supporting the NGNP was a whole-core depletion model that used a once through fuel cycle, and assumed an average burnup of  $100\text{-}150 \left[ \frac{GWd}{t} \right]$  after an 18 to 24 month residence time in the core [45]. Much of the work from this study is applicable only to prismatic designs, such as the effects of the number of batches cycling, and fuel shuffling on core neutronics [45].

### **2.2.3 HTR-10**

The HTR-10 is a 10 MW, HTGR design. Multiple studies exist examining the effects of pebble and TRISO arrangement on the HTR model. These studies primarily work with the Reactor Monte Carlo (RMC) or MCNP5 programs. A base benchmark study created the HTR-10 in MCNP. Pebbles contained 8335 TRISO particles on average, dispersed in a cubic lattice. Pebbles, meanwhile, are in a BCC arrangement, such that fuel/moderator ratios and void fractions stay constant [25].

A later study used RMC to study the explicit modeling of the random nature of both the pebbles and particles in the core, a 'double heterogeneity' [42]. The Random Sequential Addition (RSA) method was used to distribute the TRISO particles within the pebbles (the packing fraction was less than 30%, the maximum RSA can achieve). The Discrete Element Method (DEM) dispersed pebbles. To simplify the model, it assumed that all pebbles have identical TRISO dispersal patterns. Testing showed this caused little ( $\sigma$  less than 0.00014) error between this simplification and a model using different TRISO arrangements in each pebble. The RMC model had good agreement with VSOP HTR-10 simulations [42].

Other work with the HTR-10 introduces a new method of explicit random particle dispersion for use in RMC, called the Random Universe Geometry method (RUG). RUG improves on RSA by allowing a higher particle packing fraction, and on the DEM by being faster and simpler to implement [29]. Whenever a particle enters a cell that is

stochastic, the algorithm randomly samples from a list of possible materials, and determines the contents of the cell mid-transport. The RUG method has good agreement with preliminary testing using HTR-10 benchmarks [29].

#### 2.2.4 Xe-100

Aided by experience from the PBMR project, the X-energy Xe-100 is a 200 MWt HTGR pebble-bed SMR [17, 16]. It is similar in design to all of its predecessors, featuring LEU TRISO particle fuel in 3.0 [cm] radius pebbles. While the Xe-100, or a similar design from X-energy, is not in operation as of this publication, the project is still ongoing. It is this reactor that the micro-reactor described in this thesis is most heavily influenced by.

The Xe-100 uses approximately 220,000 pebbles in a six-pass cycle, and TRISO particles using Uranium Oxycarbide (UCO) — identical to the ones intended for the PBMR [17]. However, while the number of passes is unchanged, the target end burnup for the pebbles is higher, at  $160,000 \left[ \frac{MWd}{tU} \right]$  [17]. While the Xe-100 hasn't been built yet, there have been studies conducted by ORNL providing data on the production and material properties of the UCO-based fuel particles [19] and pebbles utilizing them, which the Sangamon20 and Sangamon200 models reference for fuel material data such as density.

#### 2.2.5 Modern HTGRs: Conclusion

While the PBMR and Xe-100 are the most closely related to the Sangamon20 and Sangamon200 models, the HTR-10 is a helpful point of reference, as it is closest in size to Sangamon20. In contrast to the reactors mentioned in Chapter 1, the modern HTGR examples discussed in this chapter focused on computational modeling and methods as opposed to empirical data and methods. In particular, the modeling efforts of Karriem, Z. et al. [24] provide an important point of comparison in the heterogenization tests. Additionally, the analysis in [35] on the effects of fresh pebbles lumping together in the PBMR using VSOP provided insight when investigating pebble lumping due to randomness in the Sangamon reactors.

# Chapter 3

## Methodology

This chapter introduces modeling and design details of Sangamon reactors: the Sangamon200, and a scaled-down version, the Sangamon20; inspired by the pebble bed designs of the PBMR [52], Xe-100 [16, 17], and the smaller size of the HTR-10. Both Sangamon200 and Sangamon20 are UCO-pebble fueled, helium cooled reactors. All simulations used Serpent version 2 [27] with postprocessing and analysis performed using Python [51] and the Python libraries numpy [18] and PyNE [41].

Before one can confidently analyze reactor physics and safety, it is important to ensure the models used are reliably defined and well-understood. To this end, Section 3.1 and Section 3.2 will lay the foundation for the model, describing mechanics of the particle dispersal routine and the Monte Carlo run parameters. The following sections, Section 3.3 and Subsection 3.3.1, detail the single-pebble models, which are used to find the fuel compositions used in the full-core models. The full-core models themselves are described in Section 3.4 and Section 3.5. Finally, the last sections of this chapter detail the various effects we test by perturbing the Sangamon20 model.

### 3.1 Modeling Particle and Pebble Dispersal

Often in HTGR modeling, a uniform lattice is used to approximate the locations of TRISO particles and fuel pebbles. However, this doesn't reflect realistic TRISO distributions in the pebbles and pebble distribution in the core. Pebbles are not perfectly stacked in the core. Further, models utilizing lattices often cut off portions of pebbles at the boundaries that don't perfectly fit. Instead, the Sangamon200 and Sangamon20 use a random placement of pebbles. This random dispersal is not only truer to a real pebble-bed, but restricts pebble locations to the boundaries of the core, ensuring edge effects are accounted for in our models.

In order to determine the locations of random TRISO particles and pebbles, the Serpent particle dispersal routine was leveraged. The routine takes either the number of particles, defined by the user; or  $\eta_{pf}$ , the packing fraction (the total volume of particles divided by the volume of that space). The user must define the particle radius, and the size and shape of the volume housing the particles. The routine first randomly determines a single point for each particle contained in the volume. Then, the routine uses the 'growth factor' and 'shake factor' - both described

as fractions of the particle radius, and iterates. During each iteration, the size of the point's radius increases by the growth factor. Additionally, the center will move in a random direction a distance equal to the shake factor. If the particle growth causes the particle to overlap with another particle or leave the volume, it doesn't grow that cycle. Similarly, if the center's movement causes overlap or the particle to leave the containing volume, it doesn't move [10]. The dispersal routine iterates until all particles are to their full size, contained in the volume, and not overlapping with any other particles. The routine generates an output file, in which each line gives the location of a particle center (in x,y,z coordinates), a particle radius, and the name of the particle type, to associate it with the "pbcd" (short for pebble bed) card (see the input syntax manual from [27]). For this work, we used a growth factor of 0.05 and a shake factor of 0.1 [10].

## 3.2 Run Parameters and Conditions

All Serpent 2 simulations and post-processing scripts were run on an Ubuntu 18.04 machine using Python version 3.8.5, numpy version 1.19.2, and PyNe version 0.7.1. Cross-section data is from the JEFF 3.1.2 data libraries. Below, Table 3.1 gives the Monte Carlo run parameters for each Serpent model.

Table 3.1: Relevant Monte Carlo Parameters for Single Pebble and Sangamon Reactor Simulations

Parameter	Single Pebble	Sangamon200	Sangamon20
Inactive Cycles	250	50	50
Active Cycles	500	150	100
Neutron Population	20000	70000	50000

All input files are available on github at [39].

## 3.3 Single Pebble Depletion Model Geometry and Materials

The single pebbles are the only simulations that utilize individually defined TRISO particles by default. Each pebble has an inner region containing the TRISO particles embedded in graphite, and an outer region consisting only of graphite as illustrated by Figure 3.1.

Table 3.2: Relevant Material Properties Used in Monte Carlo Simulations

Material	Density [ $\frac{g}{cc}$ ]	Source
UCO	11.0	[19, 34]
Graphite	1.74	[21, 23]
Pyrolytic Carbon	2.20	[32]
Silicon Carbide	3.10	[32]

Table 3.2 gives the densities of all solid materials in the model. The density of the helium coolant was calculated

using the ideal gas law [30]. The graphite reflector properties are assumed to be the same as the buffer layer in TRISO particles (which is assumed to have the same properties as the graphite matrix in the pebbles).

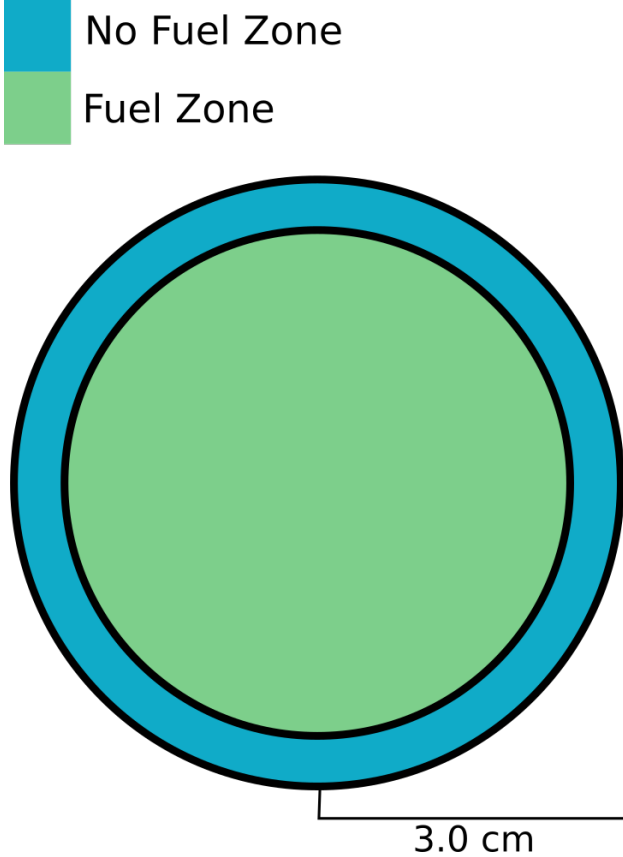


Figure 3.1: Pebble Zones

Table 3.3: Pebble Parameters Used in Monte Carlo Simulations

Parameter	Value
Fueled-Center Radius [cm]	2.5
Graphite Outer Shell Thickness [cm]	0.5
Total Radius [cm]	3.0
TRISO Particles per Pebble	18,000

Figure 3.1 shows the fueled vs non-fueled regions of the pebbles, while Table 3.3 provides the geometric measurements of the pebbles. For homogenized pebbles, the "fuel zone" is the homogenized center consisting of dispersed TRISO particle material blended with graphite, while the non-fueled region is pure graphite. Each region homogenized by volume fraction uses the "mix" card (see [27]) in Serpent to blend the fuel, TRISO layer, and graphite matrix materials. In heterogeneous models, the fueled region marks the part of the pebble where TRISO particles are located inside a graphite matrix, and the non-fuel region is the area of pure graphite that surrounds it. Figure 3.2 and Table 3.4 give detailed measurements on geometric dimensions of a TRISO particle and its layers,

and gives a visual reference. Figures 3.2 and 3.1 are both to scale.

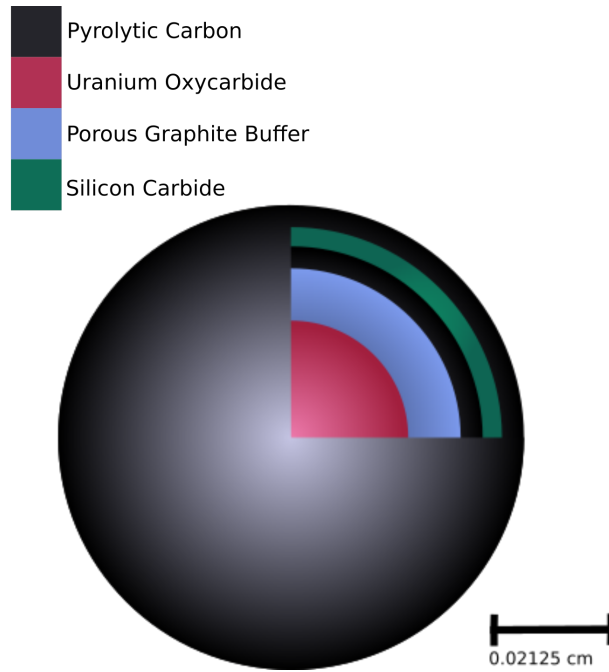


Figure 3.2: TRISO Particle Layers

Table 3.4: Particle Parameters Used in Monte Carlo Simulations

Parameter	Value [cm]
Uranium Oxycarbide Kernel Radius	0.02125
Graphite Layer Thickness	0.03075
Inner Pyrolytic Carbon Layer Thickness	0.03475
Silicon Carbide Layer Thickness	0.03825
Outer Pyrolytic Carbon Layer Thickness	0.04225

### 3.3.1 Fuel Composition Determination

The residence time of a pebble in the active core determines its isotopic composition. We chose to model seven possible pebble compositions, one for each of the six 6-month passes, plus an additional composition for fresh pebbles. The seven pebble compositions are equally and randomly distributed in the core.

The design approximates the exact isotopic composition by running a burnup calculation using Serpent for a single pebble inscribed within a cube of helium. The model uses a reflective boundary condition, and burnup steps are measured in days, with each step corresponding to a complete six-month pass: 180, 360, 540, 720, 900, and 1080 days.

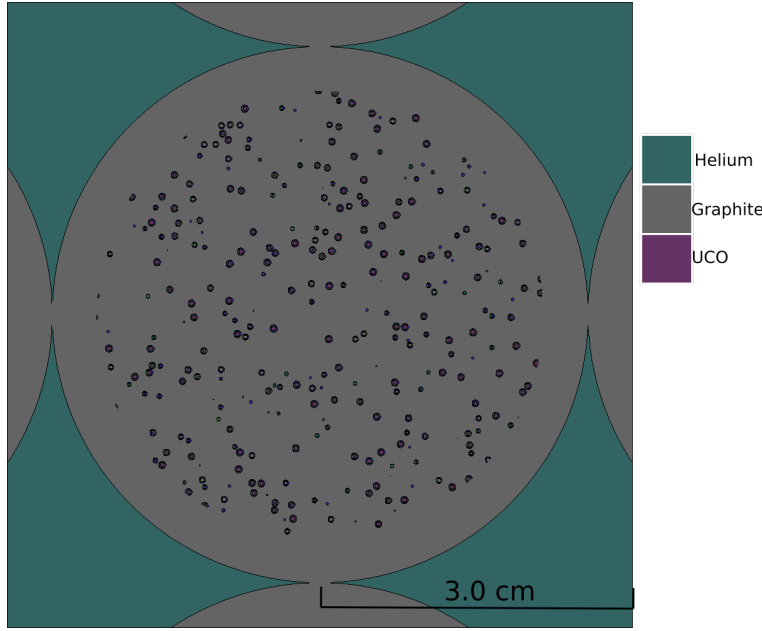


Figure 3.3: Geometry of the Single-Pebble Burnup Calculation for Sangamon20

Figure 3.3 is a cross-sectional slice of the pebble used in the depletion runs performed by Serpent. With seven depletion states in total — one for each pass, plus one for the fresh fuel — we subsequently have seven unique pebble compositions. Both the Sangamon20 and Sangamon200 models use this method to generate the necessary isotopic compositions, though they have a different starting enrichment (see 3.5 in the fresh pebbles).

### 3.4 Sangamon200

The top and bottom of the reactor core are a flat surface, to create a cylindrical shape for the active core. The graphite reflector, which is a cylindrical shell as well, surrounds it with no barriers between the reflector and active core region. There are no control rods included in these simulations.

Table 3.5: Geometric and Internal Core Parameters in the Sangamon Reactors

Parameter	Sangamon200 [17], [16]	Sangamon20
Thermal Power [MW]	200	20
Average Core Temperature [K]	800	800
Enrichment [wt%]	15.5%	19.75%
Average Core Pressure [MPa]	5.9	5.9
Outer Core Radius [cm]	216	165
Outer Core Height [cm]	1150	330
Reflector Thickness [cm]	92	75
Number of Pebbles	220,000	22,680
Packing Fraction [%]	53.0	56.0

While Sangamon200 is not the focus of this assessment, some parameters were used to develop the Sangamon20's design. We used the outgoing partial current of the reflector to constrain the Sangamon20 design such that the external exposure of the 20 MWth design was less than or equal to the 200 MWth design. To do so, a surface detector placed in the reflector, just inside the outer bound of the reflector, shown in Figure 3.4, to tally the outgoing neutron current. When determining the appropriate reflector thickness in Sangamon20, this current is used as an upper boundary and reference point — that is, the graphite reflector must not only be sufficient to keep the reactor critical, but must also keep the outgoing surface current less than or equal to Sangamon200's to protect the RPV.

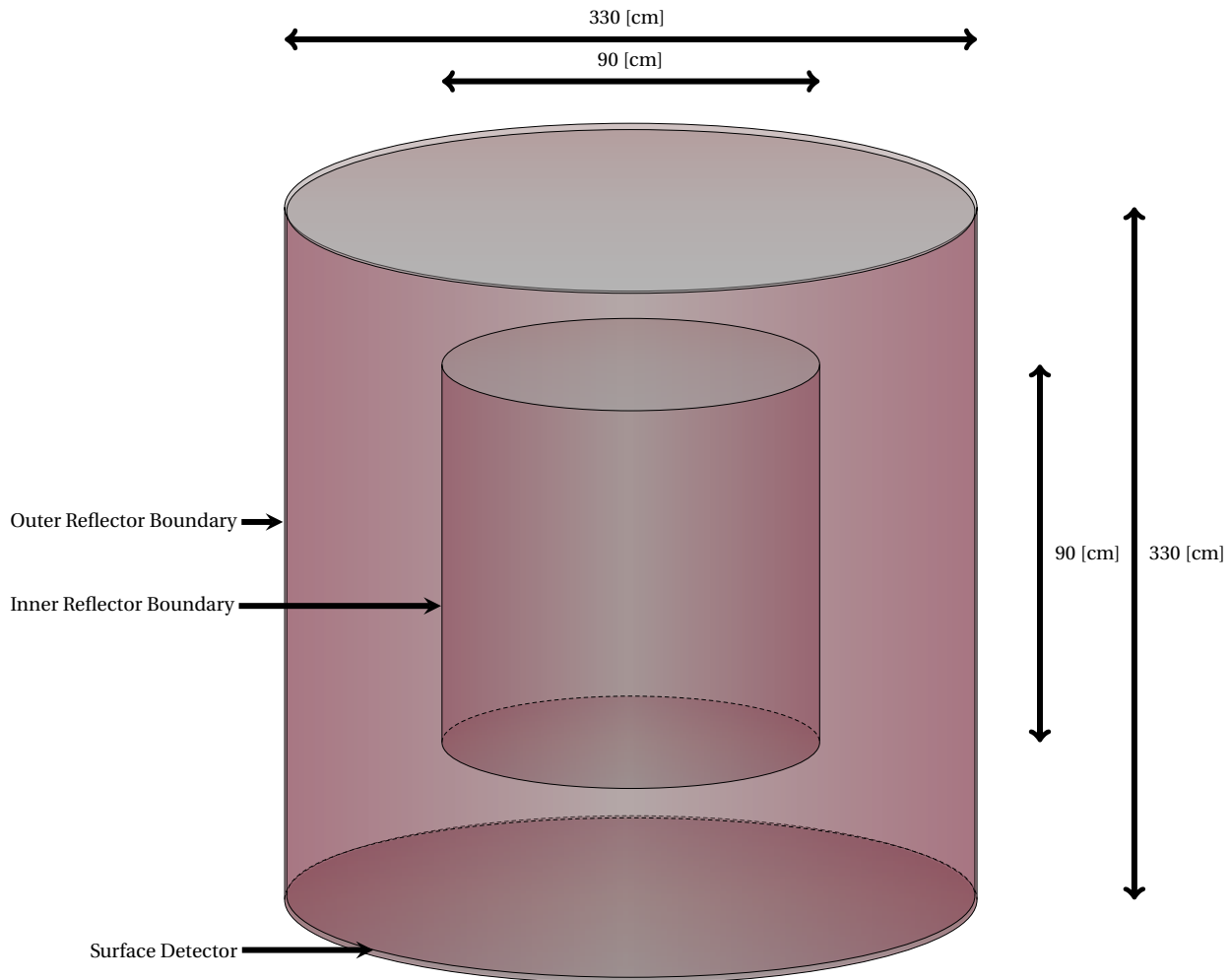


Figure 3.4: Detector Placement Inside Reflector in Sangamon200 and Sangamon20

In Figure 3.4, the graphite reflector outer boundary is shown, with the surface detector shell shown inside of it. The active core region, which contains the fuel pebbles, is the innermost cylindrical region, while the reflector is the region surrounding it. The surface detector's height is 2 [cm] less than that of the reflector (e.g., the top of the detector is 1 [cm] below the top of the reflector) and the radius is 1 [cm] less than that of the reflector. This

detector measures the outgoing neutron current in  $\left[ \frac{\text{neutrons}}{\text{s}} \right]$ . To arrive at the unit of  $\left[ \frac{\#}{\text{cm}^2 \text{s}} \right]$  most are familiar with, we divide by the detector's surface area thus:

$$J^+ = \frac{J_s^+}{S_d} \quad (3.1)$$

where

$$\begin{aligned} J^+ &= \text{outgoing neutron current } \left[ \frac{\#}{\text{cm}^2 \text{s}} \right] \\ J_s^+ &= \text{surface unadjusted outgoing neutron current } \left[ \frac{\#}{\text{s}} \right] \\ S_d &= \text{detector surface area } [\text{cm}^2] \end{aligned}$$

After accounting for the surface area, the outgoing current at the detector in Sangamon200 is  $9.156 \times 10^{11} \pm 1.099 \times 10^{09} \left[ \frac{n}{\text{cm}^2 \text{s}} \right]$ .

## 3.5 Sangamon20

Sangamon20 has identical material properties to Sangamon200, with the exception of the fuel, which is enriched to 19.75%  $^{235}\text{U}$  when fresh (and subsequently has a different isotopic composition as it burns). It also assumes an identical power density, which is assumed not only in the single pebble models, but is also used when calculating the active core volume (see Subsection 3.5.2). While the thermal power of Sangamon20 is 10% that of Sangamon200, it isn't sufficient to simply scale Sangamon200's dimensions down to 10% of their original values, as that wouldn't have the correct volume for the required pebbles, and the neutronics — such as leakage — would be inconsistent. An inner core volume that is 10% Sangamon200's should be a good approximation, but in order to be certain that this volume would hold the mass of fuel needed, a constraining calculation was carried out, which is detailed in Subsection 3.5.2.

### 3.5.1 Graphite Reflector Thickness Determination

As discussed in Section 3.4, the outgoing neutron current at the outer reflector boundary — where the RPV would be — is used as the maximum acceptable value for outgoing neutron current in Sangamon20. Figure 3.5 below provides the outgoing neutron current at the reflector boundary in Sangamon20 versus the thickness of the reflector.

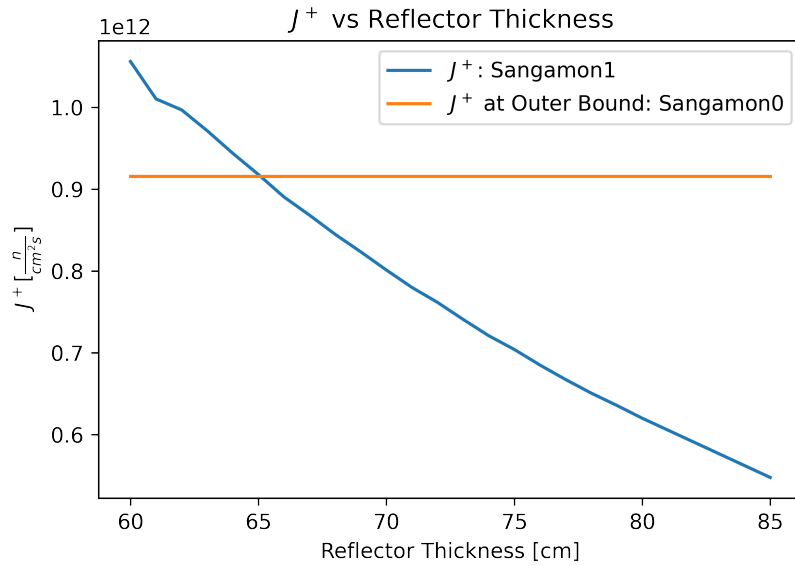


Figure 3.5: Outward Neutron Current versus Reflector Thickness

Ultimately, the chosen reflector thickness was 75 [cm].

### 3.5.2 Inner Core Volume Determination

The first assumption made in the scale-down is that Sangamon200 and Sangamon20 have the same specific power, or  $\left[ \frac{\text{kW}}{\text{g UCO}} \right]$ .

To calculate the mass of fuel in Sangamon200:

$$M_{f,200} = \frac{4}{3}\pi r_u^3 \rho_u n_T n_{p,200} \quad (3.2)$$

where

$$M_{f,200} = \text{mass of fuel in Sangamon200 [g]}$$

$r_u$  = the radius of the UCO kernel inside a TRISO particle [cm]

$\rho_u$  = the density of UCO in [ $\frac{\text{g}}{\text{cc}}$ ]

$n_T$  = number of TRISO particles in one pebble

$n_p$  = number of pebbles in Sangamon200

Using the parameters from Table 3.5, the power density of Sangamon200 and Sangamon20 is 0.11 [ $\frac{kW}{g}$ ]. With a power capacity of 20 MWth, one can calculate the total mass of UCO in Sangamon20 as

$$M_{f,20} = \frac{P}{\rho_p} = 181818.18 [g] \quad (3.3)$$

where

$M_{f,20}$  = total mass of UCO in Sangamon20 [g]

$P$  = Thermal power of Sangamon20 [kW]

$\rho_p$  = Sangamon20's power density [ $\frac{kW}{g}$ ]

Equation 3.2 calculates the total mass of fuel in the Sangamon200 reactor by first calculating the mass of UCO in a single pebble using the density of UCO and the total volume of UCO kernels in a single pebble. This value is then multiplied by the number of pebbles in Sangamon 200 (see Table 3.5). The total mass of fuel in the reactor divided by the mass of fuel in a single pebble gives the number of pebbles in the reactor, as follows:

$$n_{p,20} = \frac{M_{f,20}}{\frac{4}{3} r_u^3 n_T \rho_u} \quad (3.4)$$

where

$n_{p,20}$  = number of pebbles in Sangamon20 [-]

$M_{f,20}$  = total mass of UCO in Sangamon20 [g]

$r_u$  = radius of a UCO kernel [cm]

$n_T$  = number of TRISO particles in a single pebble [-]

$\rho_u$  = density of UCO [ $\frac{g}{cm^3}$ ]

Rounding up - there can only be complete pebbles - we arrive at the number of pebbles for the Sangamon20 that are reported in Table 3.5.

Knowing the number of pebbles is insufficient - the exact dimensions of the active core region are still undefined.

To determine the volume of this space, the formula uses concept of the packing fraction. Assuming the pebble behavior is random loose packing [49] - the pebbles have unsystematically fallen into the core and the core is unshaken - the packing fraction in the range of 0.56 to 0.60 [49]. Using the definitions above, the active core volume is

$$V_{c,20} = \frac{n_{p,20} \frac{4}{3} \pi r_p^3}{\eta_{pf}} \quad (3.5)$$

where

$V_{c,20}$  = volume of the active core in Sangamon20 [ $cm^3$ ]

$n_{p,20}$  = number of pebbles in Sangamon20 [-]

$r_p$  = radius of a pebble [cm]

$\eta_{pf}$  = packing fraction [-]

Using the formula for the volume of a cylinder, one can plot possible sets of  $r_{c,20}$  and  $h_{c,20}$  that satisfy the volume requirement, which is illustrated in 3.6.

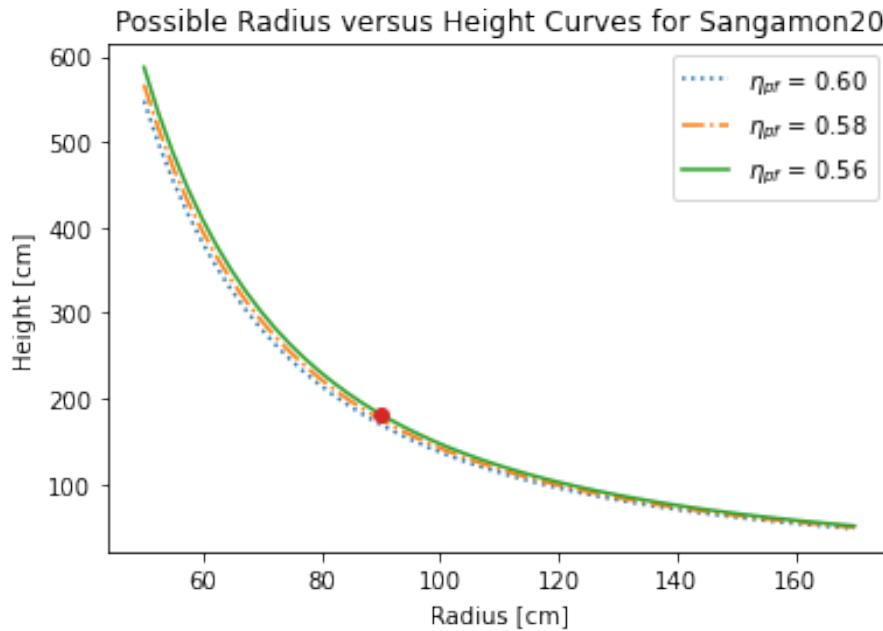


Figure 3.6: Curve of possible height and radii that satisfy the volume requirements imposed by packing fraction(s)  $\eta_{pf}$

One of the most critical configurations for a cylinder is a *square* shape, in which the height is equal to the diameter. As most designs use a height that is greater than or equal to the diameter, Sangamon20 is a square cylinder. A packing fraction of 0.56 was ultimately chosen for Sangamon20 as it is the closest packing fraction to Sangamon200 while still staying in the range appropriate for haphazard packing. The point indicated in 3.6 shows the radius and height selected for Sangamon20 - a radius of 90 [cm], and a height of 180 [cm].

## 3.6 Heterogenization Tests

As described above, the pebbles use the approximation of a homogenized 'fueled-center', to reduce computational load. This can, however, make the results of the simulation less accurate. To determine the degree to which this affects reactor parameters such as  $k_{eff}$  or outward neutron current, a few simulations performed undid this change, explicitly defining all TRISO particles in the pebbles, as they are in the single-pebble (infinite lattice) depletion models which generated the equilibrium fuel composition. These so-called heterogenization tests compared the 2-group fast and thermal fluxes in the radial and axial direction. In addition, they compared the neutron energy spectrum using a 315-group energy structure. Beyond showing the full spectra for each of these values for comparison, the relative difference is provided graphically for each so the differences induced by this change can be more readily observed. Other than the choice to explicitly model the TRISO particles, the heterogenized model is identical to the Sangamon20 homogenized-pebble model. The results of this test can be found in Section 4.3.

## 3.7 Reactor Sensitivity to Pebble Locations and Symmetry

By the nature of random pebble dispersal, there are a theoretically infinite number of perturbations to the Sangamon reactor models that are no different with the exception of slight variations in pebble locations. It is also entirely possible to have bands in the reactor such that multiple pebbles of same (or similar) burnup align to form localized lines or pockets. In the interest of better characterizing the extent to which these may effect the neutronics, we created a series of tests to explore the affect of various pebble composition locations.

The *shuffling* test maintained the pebble locations, but changed what composition the individual pebbles were (for results, see Subsection 4.4.2). As an example, Run 1 in the shuffle test makes all fresh, or "zero-pass" pebbles of the first-pass composition, first-pass pebbles of the second-pass, and so on down the line. Run 2 makes the originally fresh (zero-pass) pebbles the second pass composition, the first-pass pebbles the third-pass composition, and so on. This scheme is described in 3.6.

The second analyzed the effects of using a symmetry simplification, in order to improve computational speed (see Subsection 4.4.1) where  $\frac{1}{6}$  of the core is modeled with a periodic boundary condition (neutrons exiting one side

Table 3.6: Shuffle Test Run Schemes

Original Fuel Position in Control	Position in Test Run					
	Run 1	Run 2	Run 3	Run 4	Run 5	Run 6
0	1	2	3	4	5	6
1	2	3	4	5	6	0
2	3	4	5	6	0	1
3	4	5	6	0	1	2
4	5	6	0	1	2	3
5	6	0	1	2	3	4
6	0	1	2	3	4	5

of the symmetry slice enter the other at the same height and trajectory). We start with a full core model, and then select a slice from that core. The slice used to simplify changed in each test, shown in Figure 3.7. In each test, all other parameters remain the same.

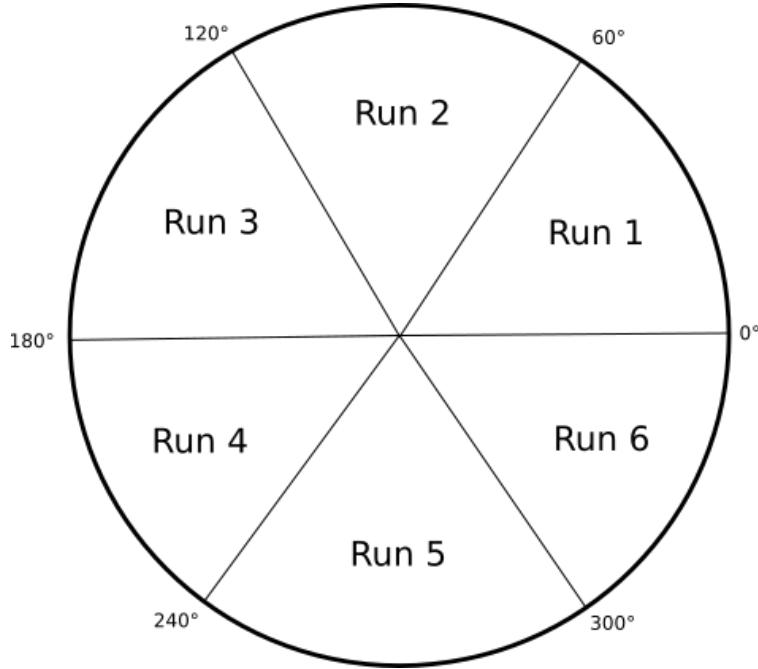


Figure 3.7: Symmetry Test Run Layouts

In both tests, the  $k_{eff}$  and outgoing currents are recorded and compared to the control model's  $k_{eff}$  and  $J^+$  (for results please refer to Section 4.2). A full spectrum of core components wasn't performed as in the heterogenous tests, as the difference between the results of this test and the control were small compared to the heterogeneity tests. Appendix 5.2 and Section B contains all geometry and mesh images for each run, and a pixel-by-pixel image difference of the mesh results.

# Chapter 4

## Results

This chapter presents the results of the tests described in Section 3.5, 3.6, and 3.7. Section 4.1 first presents the atomic fractions of select isotopes of interest, and the fission rate/thermal flux mesh corresponding to each depletion time step. Then, Section 4.2 covers the results of the basic control model. The final sections — dedicated to homogenization (see Section 4.3), symmetry (see Subsection 4.4.1), and shuffling (see Subsection 4.4.2) — compare the results of these perturbations to the control model.

#### 4.1 Fuel Isotopic Compositions

Figure 4.1 depicts the evolution of the fission rate (hot color map) and thermal flux (cold color map) over the seven stages of burnup that we chose to model. The maximum cutoff for thermal flux is 0.625 eV in these figures. Over successive depletion steps, the fission rate and thermal flux increases. This is not unexpected — as the pebble burns, the atomic fraction of fissile  $^{235}U$  decreases. This requires that the fission rate increase to maintain criticality. Notably, the fission rate mesh for the six-month depletion step has fewer points indicating higher values when compared to the initial depletion step; however, the scales of these images are not uniform, and this is likely indicative of the fission rate profile within the six-pass pebble flattening.

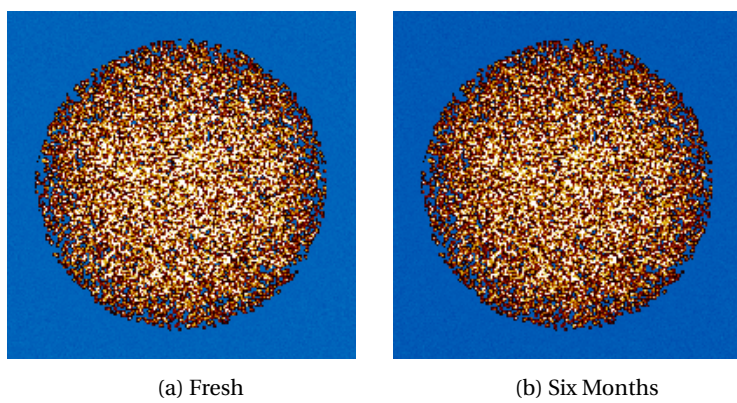


Figure 4.1: Serpent-generated mesh figures of the fission rate (hot color map) and thermal flux (cold color map) for the representative single-pebble at each depletion step. A cold color map is from shades of whitish-blue (high) to blackish-blue (low) while the hot color map is from a whitish-yellow (high) to reddish-brown (low)

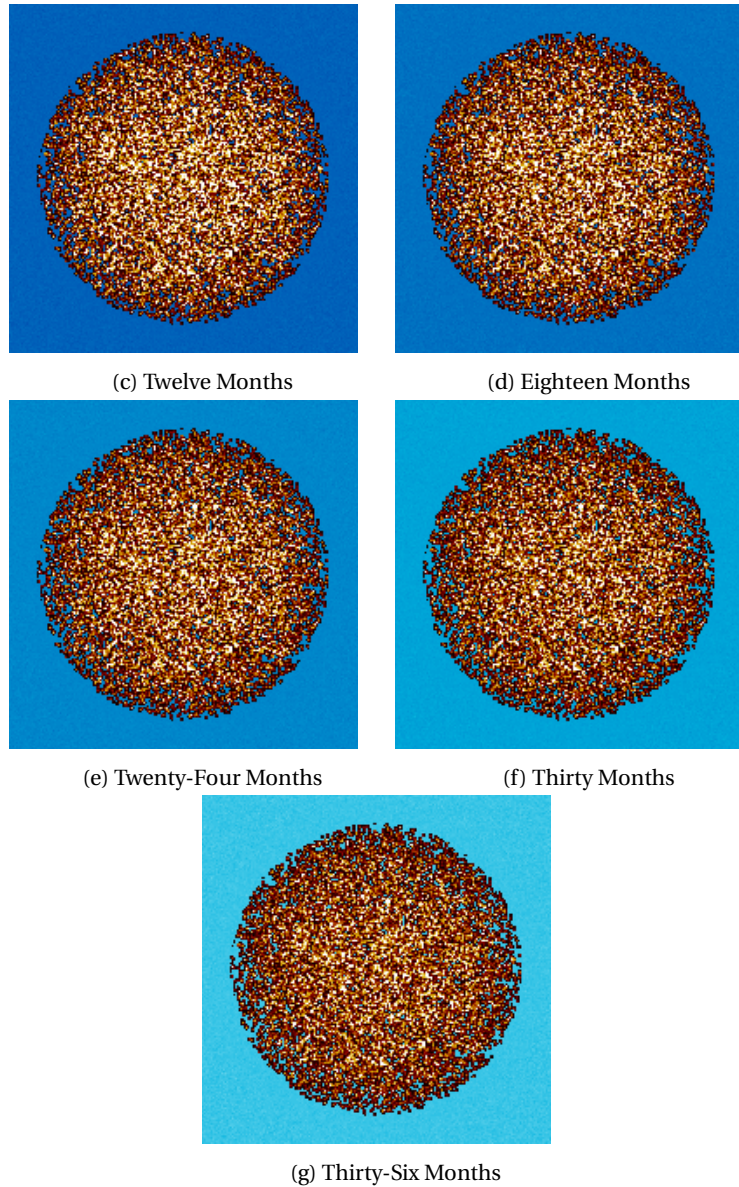
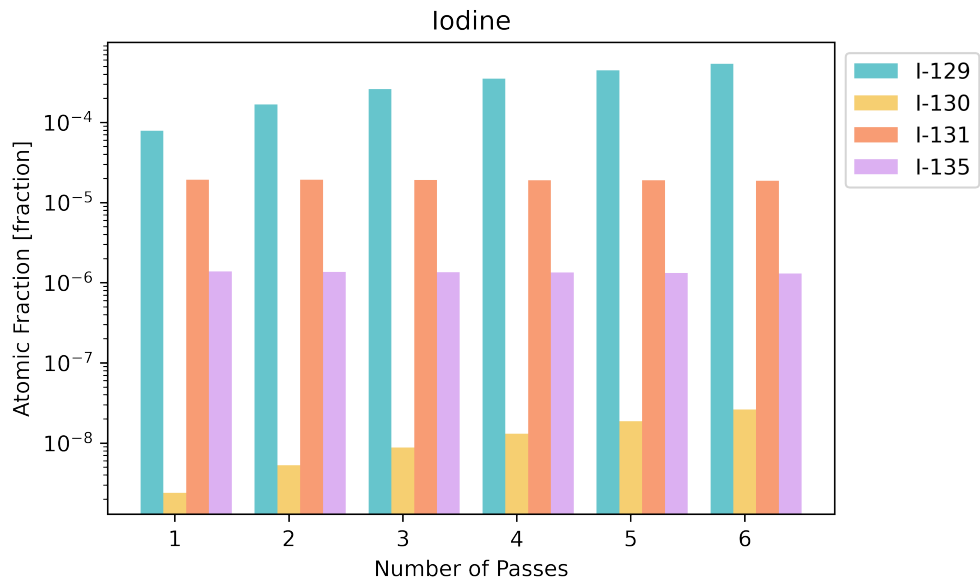


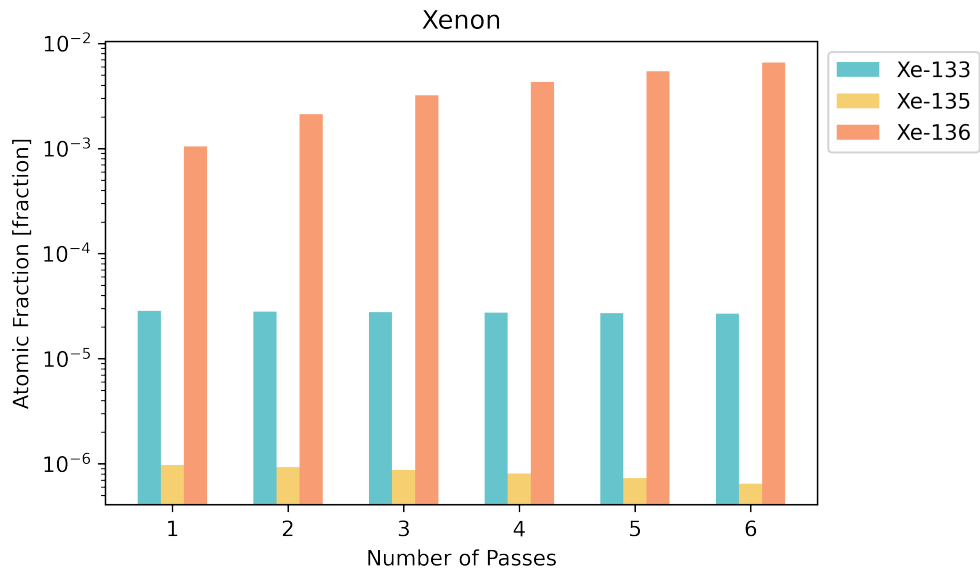
Figure 4.1: (cont.)

Understanding the effects on core neutronics such as the fission rate or thermal flux is not the only reason to find the isotopic composition of the fuel. Fission product buildup in the fuel has long term ramifications for spent fuel handling, and matters for our understanding of accident consequence analysis. The potential isotopes — and in what amounts — that a living being or environment might be exposed to after an accident is called a source term. As shown in Tables 1.1 and 1.2 in Chapter 1, fission products can either leach into the coolant gas, or be found in the fine dust formed when the pebbles bump against each other during operation. In an accident, this dust could end up outside of the RPV in the case of a breach, where it could be inhaled or reach the ground or groundwater. In order to fully understand accident consequences, one must robustly characterize the source term. Figure 4.2

provides the atomic fractions of isotopes of iodine, xenon, cesium, uranium, and plutonium within depleted fuel in the Sangamon Reactors.

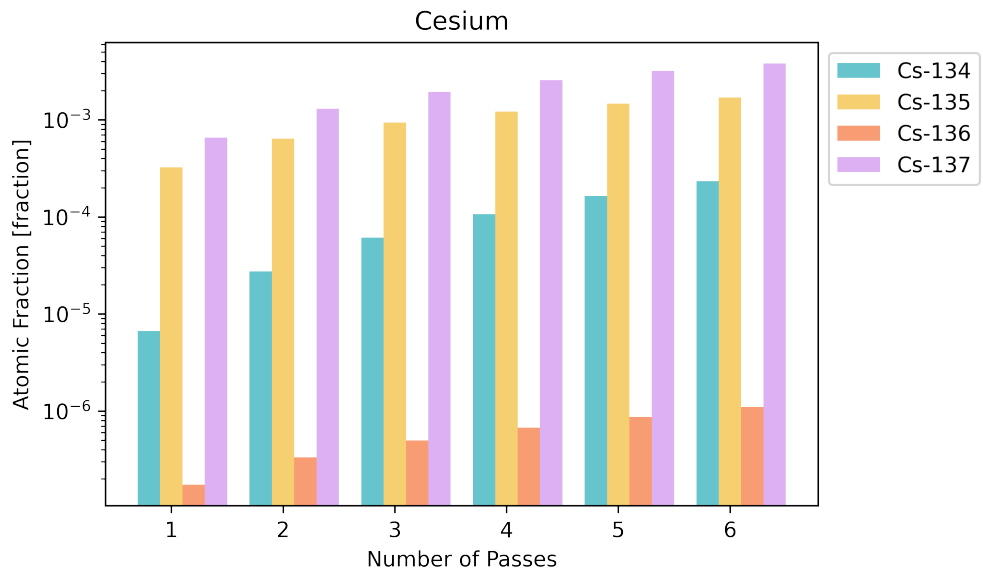


(a) Iodine isotope buildup over six burnup stages

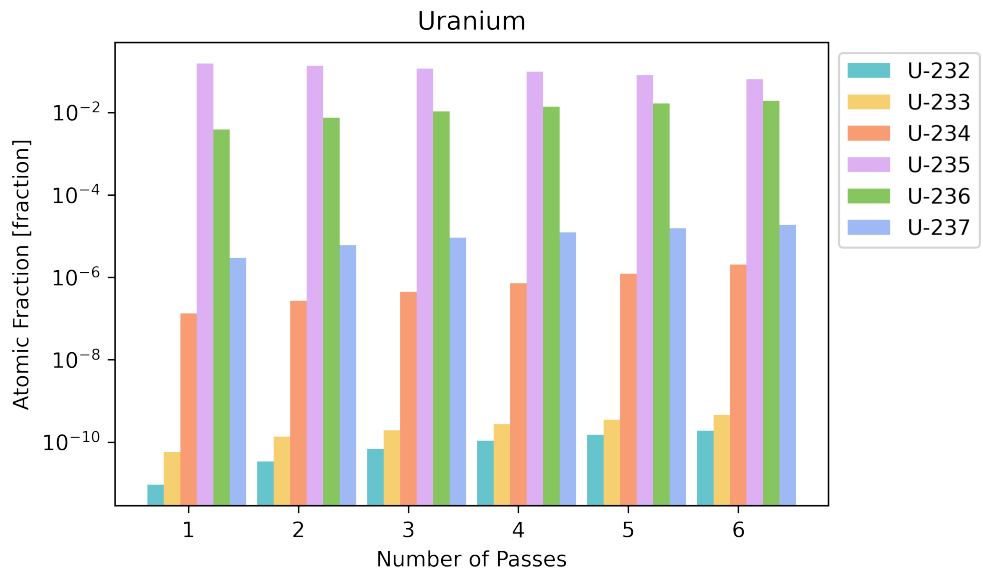


(b) Xenon isotope buildup over six burnup stages

Figure 4.2: Evolution of Safety Relevant Isotopic Concentrations in Pebbles of Sangamon20 over Six Six-Month Passes (measured in atomic fraction)

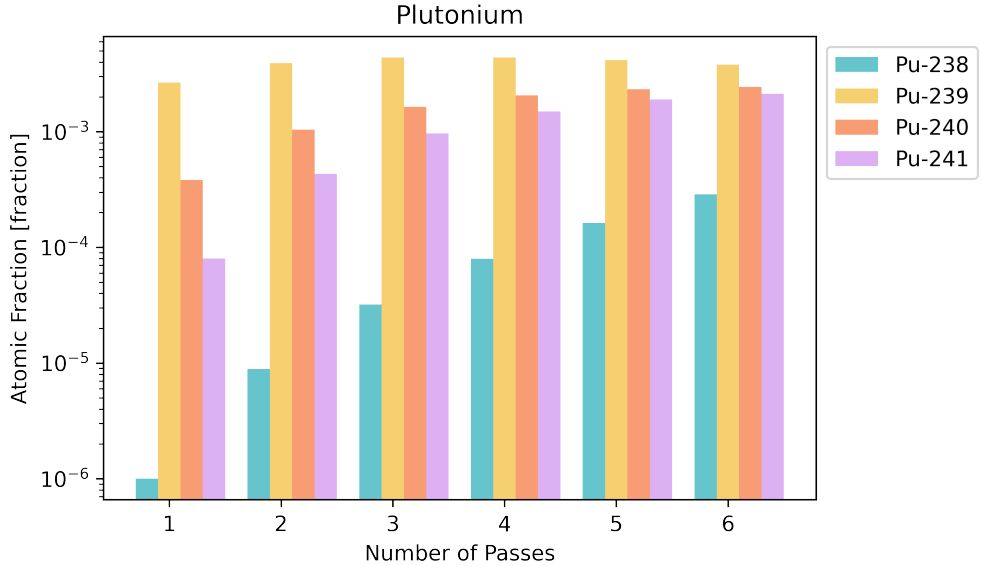


(c) Cesium isotope buildup over six burnup stages



(d) Uranium isotope buildup over six burnup stages

Figure 4.2: (cont.)



(e) Plutonium isotope buildup over six burnup stages

Figure 4.2: (cont.)

The full isotopic inventory tracked in the Sangamon20 reactor models extends far beyond those supplied in Figure 4.2. For a full list, see [37] and [38] for the compositions in Sangamon20 and Sangamon200, respectively, or [39] for a complete input file and associated output. Figure 4.2 focuses on those of interest in safety analysis, such as those in Table 1.2 and Table 1.1.

All isotopes of uranium steadily increase over time with the exception of  $^{235}U$ , ending at 0.0647 by atomic fraction in the sixth pass — significantly lower than the 0.17698 it started with.  $^{232}U$ , initially the smallest fraction of uranium sees the most dramatic increase over time, increasing by two orders of magnitude between the first ( $9.28 \times 10^{-12}$ ) and sixth ( $1.9 \times 10^{-10}$ ) cycle. While the atomic fraction doesn't reach an equilibrium, the rate at which it increases each cycle is steady by the third pass - increasing by  $4.02 \times 10^{-11}$ ,  $4.2 \times 10^{-11}$ , and  $3.9 \times 10^{-11}$  from the third to fourth, fourth to fifth, and fifth to sixth pass, respectively. The behavior of plutonium is also of interest, with  $^{239}Pu$  peaking at 0.00439. However, unlike many other isotopes, which peak in the sixth cycle,  $^{239}Pu$  crests in the third and fourth passes, decreasing from 0.00439 in the fourth pass to 0.00380 in the sixth as it begins to burn away.  $^{238}Pu$ , meanwhile, is the least abundant, but does experience the most dramatic increase over time (especially between the first and second passes).

Only the xenon content rivals the inventory of uranium.  $^{133}Xe$  appears to be steady around its initial concentration of  $2.86 \times 10^{-5}$  atomic fraction, decreasing only to  $2.68 \times 10^{-5}$  by the sixth pass.  $^{135}Xe$  is mostly stable, but does decrease slightly over the full residence time of the pebble, going from an initial  $9.70 \times 10^{-7}$  after its first six months, to  $6.46 \times 10^{-7}$  after thirty-six months.  $^{136}Xe$  is both the greatest contributor to xenon content in the fuel, and the

only isotope reported in Figure 4.2b to increase, owing to its long half life. Each cycle increases  $^{136}Xe$  content by 0.0011, beginning at a concentration of 0.00105 in the first cycle and ending at 0.0066 after the sixth. Isotopes of iodine form a smaller portion of fission products than xenon or cesium (still a relatively high magnitude) which is of concern due to its high mobility in water and uptake in the thyroid.  $^{129}I$  is the most abundant isotope of iodine reported here. It increases for the entirety of the pebble's life, beginning at  $7.38 \times 10^{-5}$  and peaking at 0.000538 at its discharge burnup.  $^{130}I$  and  $^{135}I$  are both relatively stable, due to their short half-lives, combined with transmutation after undergoing neutron capture. While  $^{130}I$  is the least abundant, it increases over time. Cesium has a net concentration similar to xenon's. Unsurprisingly  $^{135}Cs$  and  $^{137}Cs$ , which both have half-lives longer than a pebble's residency time in the reactor, are in greatest abundance, and increase over time. These, too, are of concern, due to their long half-life.

## 4.2 Full-Core Control Model

The control model of the Sangamon20 reactor is the basis for the three characterization tests this work performed, and it is the model that the results of these tests are compared against. Figure 4.3 shows a cross section of the core geometry at the origin (the midplane, the center of which is the point (0, 0, 0) ) in the xy and xz planes (Sub-Figures 4.3a and 4.3c, respectively) and provides a mesh of the fission rate and thermal flux in the xy and xz planes (Sub-Figures 4.3b and 4.3d, respectively). Both of these integrate over z and y, respectively, to produce a 2D image. The value of  $k_{eff}$  is  $1.009 \pm 0.00055$ , while the outward neutron current at the reflector edge is  $7.003 \times 10^{11} \pm 8.683 \times 10^{08}$ .

Figure 4.3e is a legend of material compositions in all cross-sectional geometry figures. In homogenized simulations, the shades of green represent the material blend forming the center of the pebble at a given burnup. For heterogenized simulations, these same shades represent the TRISO particle kernel at a particular burnup.

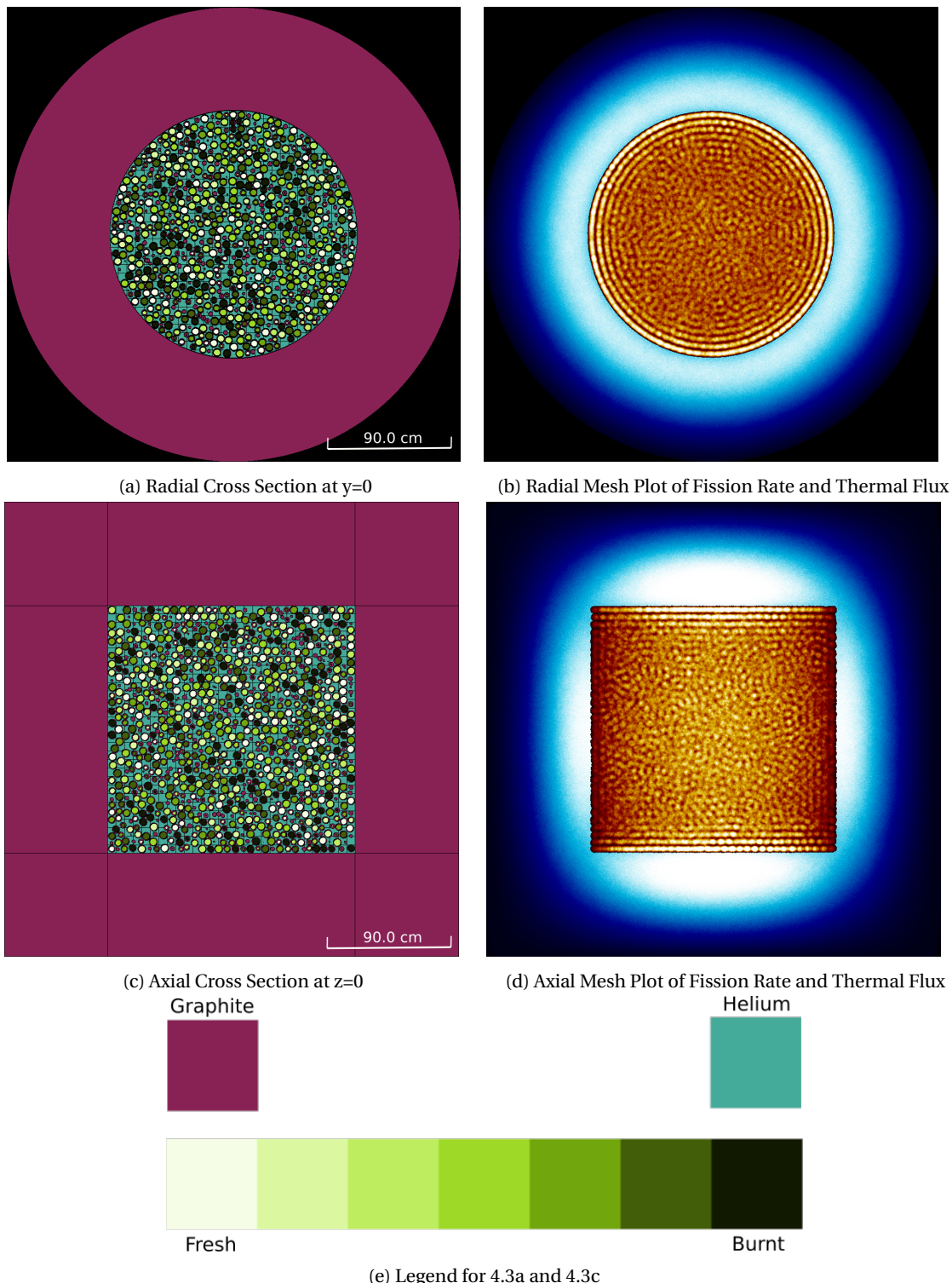


Figure 4.3: Geometry Cross Sections (left) and Thermal Flux(cold color map) and Fission Rate (hot color map) Meshes (right) for the Control Model of Sangamon20

Figure 4.3b shows bands of concentric rings around the outer edges of the active core. These bands suggest

that there is pebble alignment at the edge of the core, and that the outermost areas of the core are regions of high fission activity relative to the center. Certainly the pebbles are physically forming rings at the outer edges, and their placement becomes less structured toward the center. However, the high intensities seen in this outer region in the mesh figures are unindicative of a total flux profile showing the same. Recall that Serpent integrates over the z direction to produce a 2D plot of the xy plane. For a cylinder, the distance in z each point integrates over is the same - the height of the reactor. However, points at the outermost regions are integrating in a volume composed more of pebbles - and therefore fissile material - than the center, where more space filled with coolant. The outer regions are more regularly packed with pebbles - and therefore have less coolant than the center - because the dispersal routine (and the grow and shake algorithm) naturally cause the pebbles to line up along the reactor boundary. Lattice arrangements wouldn't have this feature because these methods ignore core boundaries.

In Figure 4.3d we can see a similar banding effect on the top and bottom edge of the core region, but not on the sides. No hot-spots on the edges because Figure 4.3d is in the xz plane, and integrates over y. However, for a cylinder, the distance integrated over is not the same at all points. At the centerline, the distance is simply the diameter. However, as you move towards the edge, the distance integrated over approaches zero. So, while these plots can help provide some insight into the core, one must be very careful to keep this uneven integration area in mind when interpreting them.

Figures 4.4 and 4.5 provide the fast and thermal flux profiles in the control model of Sangamon20, which uses homogenized pebbles, at the axial and radial (x-direction) centerlines, respectively. Bin size in the detectors was selected based on reactor geometry and the average diffusion length of neutrons in graphite [20].

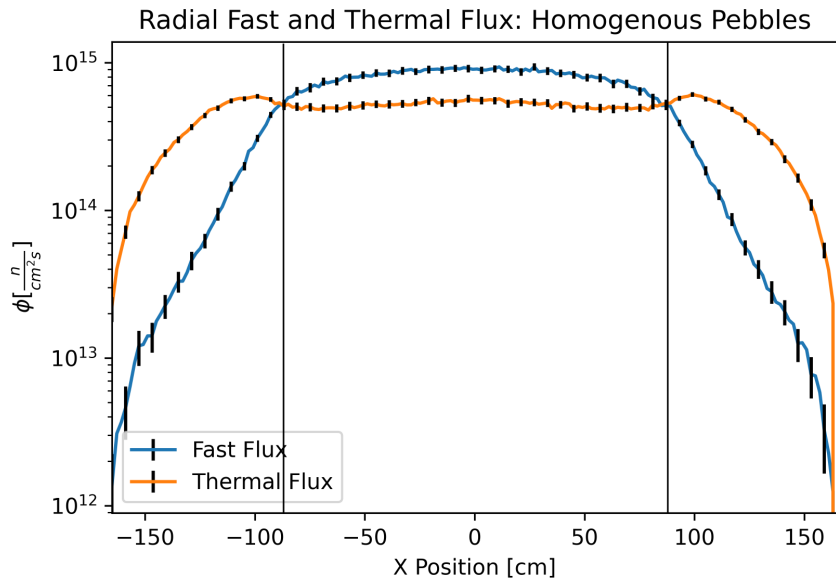


Figure 4.4: Radial Thermal and Fast Flux Profiles along the X-Axis at the Mid-Plane in the Homogenized-Pebble Sangamon20. Black vertical lines at  $\pm 90$  cm show the inner reflector boundary.

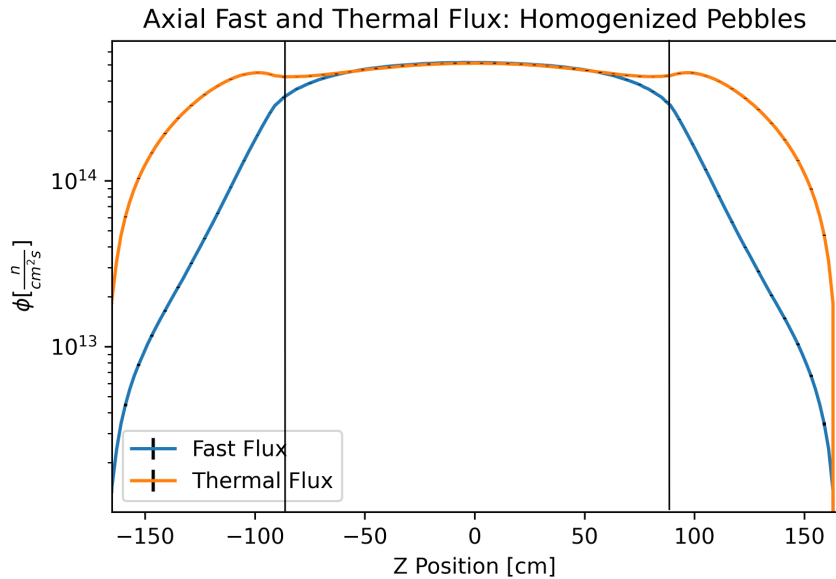


Figure 4.5: Axial Thermal and Fast Flux Profiles along the X-Axis at the Mid-Plane in the Homogenized-Pebble Sangamon20. Black vertical lines at  $\pm 90$  cm show the inner reflector boundary.

For the radial flux, a detector in the xy plane was used, which had finite bin sizes in x and y, and spanned the whole height of the reactor in the z direction. For the axial fluxes, the bins were finite in z and spanned the entire diameter of the core. Normally, these two figures would be subject to the same unequal bin sizing that affected

Figure 4.3. To counteract this, the axial fluxes (Figure 4.5) are multiplied by the ratio of the radial detector bin volume to the axial detector bin volume, as follows:

$$\phi_{axial,adjusted} = \phi_{axial,unadjusted} \frac{V_{radial}}{V_{axial}} \quad (4.1)$$

where

$\phi_{axial,adjusted}$  = detector bin-size adjusted flux  $\left[ \frac{\#}{cm^2 s} \right]$

$\phi_{axial,unadjusted}$  = unadjusted axial flux  $\left[ \frac{\#}{s} \right]$

$V_{radial}$  = radial detector bin volume  $[cm^3]$

$V_{axial}$  = axial detector bin volume  $[cm^3]$

Both axially and radially, the thermal flux sees a 'bump', which peaks approximately 10 [cm] into the reflector, at 100 [cm]. These are the highest peaks in the thermal flux, with the second highest thermal flux being at the center line. For the fast flux profile we see a flattened peak in the active core (-90.0 [cm] to 90 [cm]). Fast flux rapidly decreases in the reflector as fast neutrons down scatter in the graphite. Both Figures 4.4 and 4.5 show that the flux peaks are at the core centerline, as expected.

In addition to centerline fast and thermal flux profiles, Figures 4.7 and 4.6 provide a heatmap of the fast and thermal flux profiles in the xy plane.

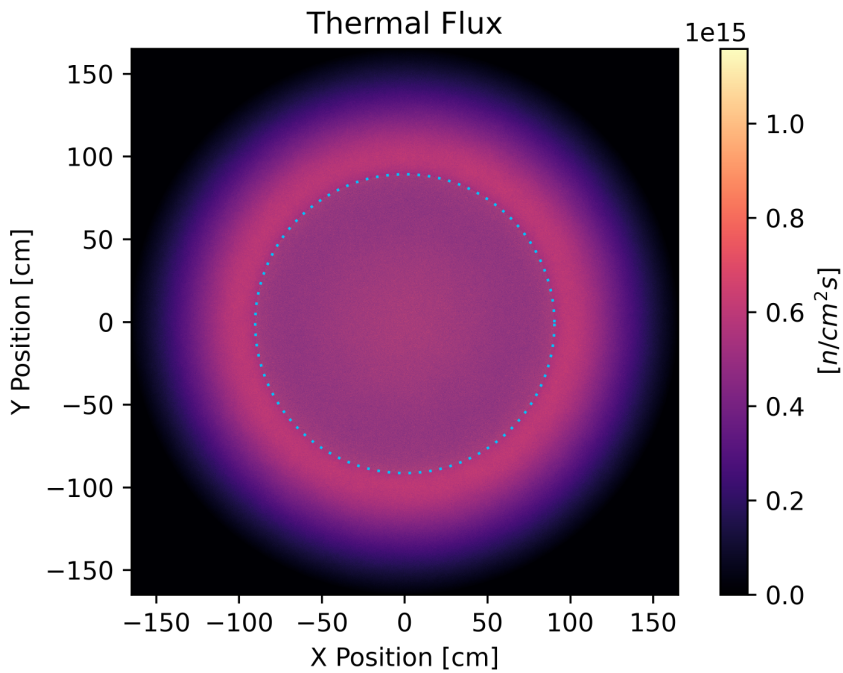


Figure 4.6: Thermal Flux in  $xy$  Plane in Sangamon20: Homogenized Pebbles. The dotted line annotation marks the boundary between the active core and the graphite reflector.

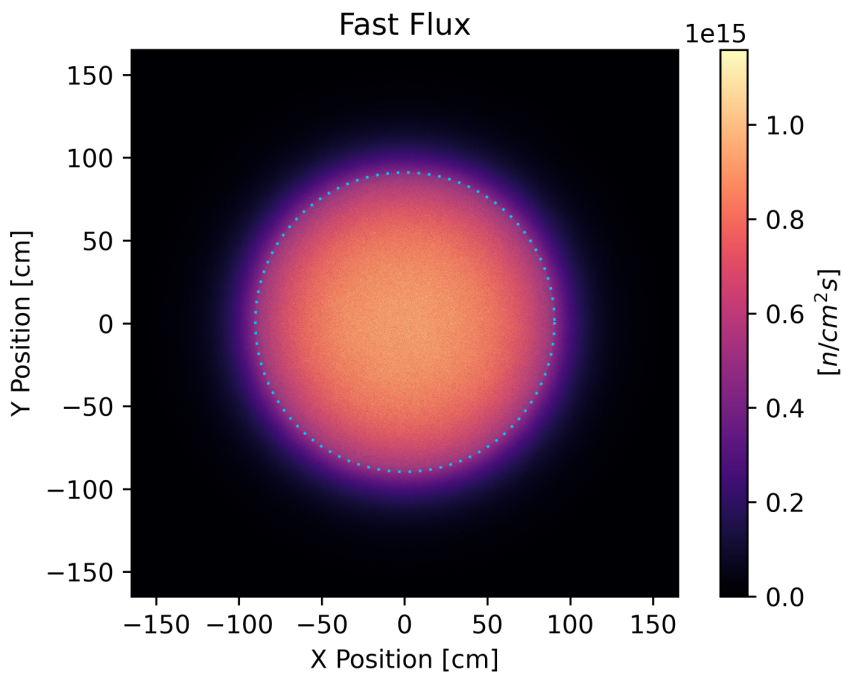


Figure 4.7: Fast Flux in  $xy$  Plane in Sangamon20: Homogenized Pebbles. The dotted line annotation marks the boundary between the active core and the graphite reflector.

A slight banding pattern on the active core's edge exists — primarily in the fast, rather than thermal, flux — but with less intensity than the fission rate banding. In the thermal flux, we see that the peak in 4.4 continues in a circular pattern surrounding the active core, approximately 10 cm into the graphite reflector. The steep drop-off in fast flux once within the outer reflector, meanwhile, is clearer in 4.7. Once again, Figure 4.7 and Figure 4.6 show that while the banding morphology may be present in the fission rate profile (and do cause a slight increase relative to the region immediately surrounding it) it does not cause concentric spikes in the flux profiles.

Figure 4.8 presents the energy spectra in the reflector, coolant, overall core, and a randomly selected fresh and sixth-pass pebble. The results are per unit lethargy and use the Tripoli 315-group energy structure [8] to set energy bin boundaries. This group structure was chosen not only because there were a sufficient number of bins to provide the desired fidelity, but also because the highest fidelity regions (smallest bin size) in the spectrum were in the lower energy values, which is of greater interest to a thermal spectrum reactor.

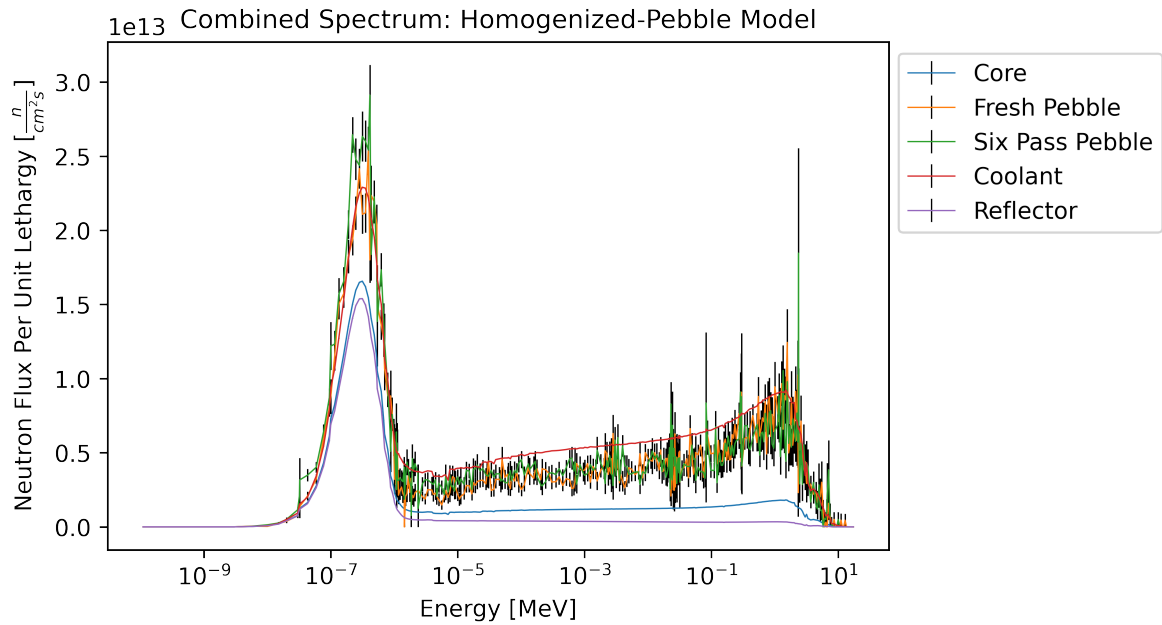


Figure 4.8: Lethargy Adjusted Neutron Flux Energy Spectrum in the Whole-Core for the Homogenized-Pebble Sangamon20

The thermal peak of the whole-core and reflector both occur around  $10 \times 10^{-7}$  MeV, which is also the energy of neutrons most-responsible for fission. The thermalization of neutrons in the reflector dominates the spectrum in Figure 4.8, indicated by the high magnitude of the thermal peak in the reflector and core and their similar shape.

The spectra for a randomly selected fresh and sixth-pass pebble are subject to the highest uncertainty of all the provided spectra in Figure 4.8, as a single pebble has a relatively small bin size, which means fewer particles contribute to the tally regions. However, if plotted alongside the coolant spectra, as in Figure 4.8, they provide

a clearer look at the flux energy spectrum in the active core region. We can see that, while the thermal energy of the fresh and six-pass pebbles is similar in shape and magnitude, the magnitude of the faster groups differs considerably.

Figure 4.9 shows the spectra of the one, two, three, four, and five pass pebbles, alongside the fresh pebble, six-pass pebble, and coolant spectra from 4.8.

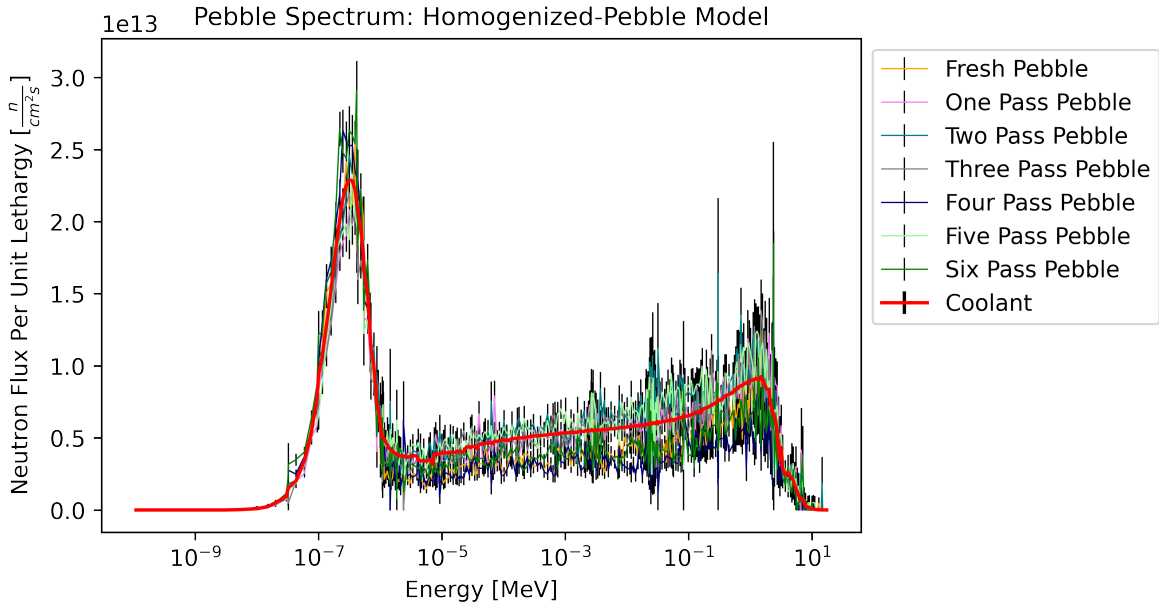


Figure 4.9: Lethargy Adjusted Neutron Flux Energy Spectrum in the Each Pebble Burnup and Coolant for the Homogenized-Pebble Sangamon20

Figure 4.9 shows that, compared to the other pebble burnup levels, the fresh and six-pass pebbles have the softest spectra. This may be due to the higher levels of  $^{239}Pu$  in the MOL pebbles. Additionally, once all pebble spectra are presented together, along with the coolant, one can see much more clearly that the coolant spectrum provides a very generalized look at the overall behavior in the pebble spectra.

### 4.3 Effect of Homogenization

The results discussed in Section 4.2 use the assumption of a pebble that has the TRISO particles homogenized and blended with the rest of the pebble matrix in the region containing fuel. However, homogenization can cause under-predictions of  $k_{eff}$  as much as 5-6% [7]. To test the impact of homogenization on Sangamon20, the heterogenization tests were performed. These tests use an otherwise identical Sangamon20 model with explicitly modeled TRISO particles and compares  $k_{eff}$ , the core spectra, and the outer reflector current. As a reminder, the isotopic compositions come from the same burnup simulation. As such, the isotopic compositions between the

homogenized and heterogenized simulations are identical.

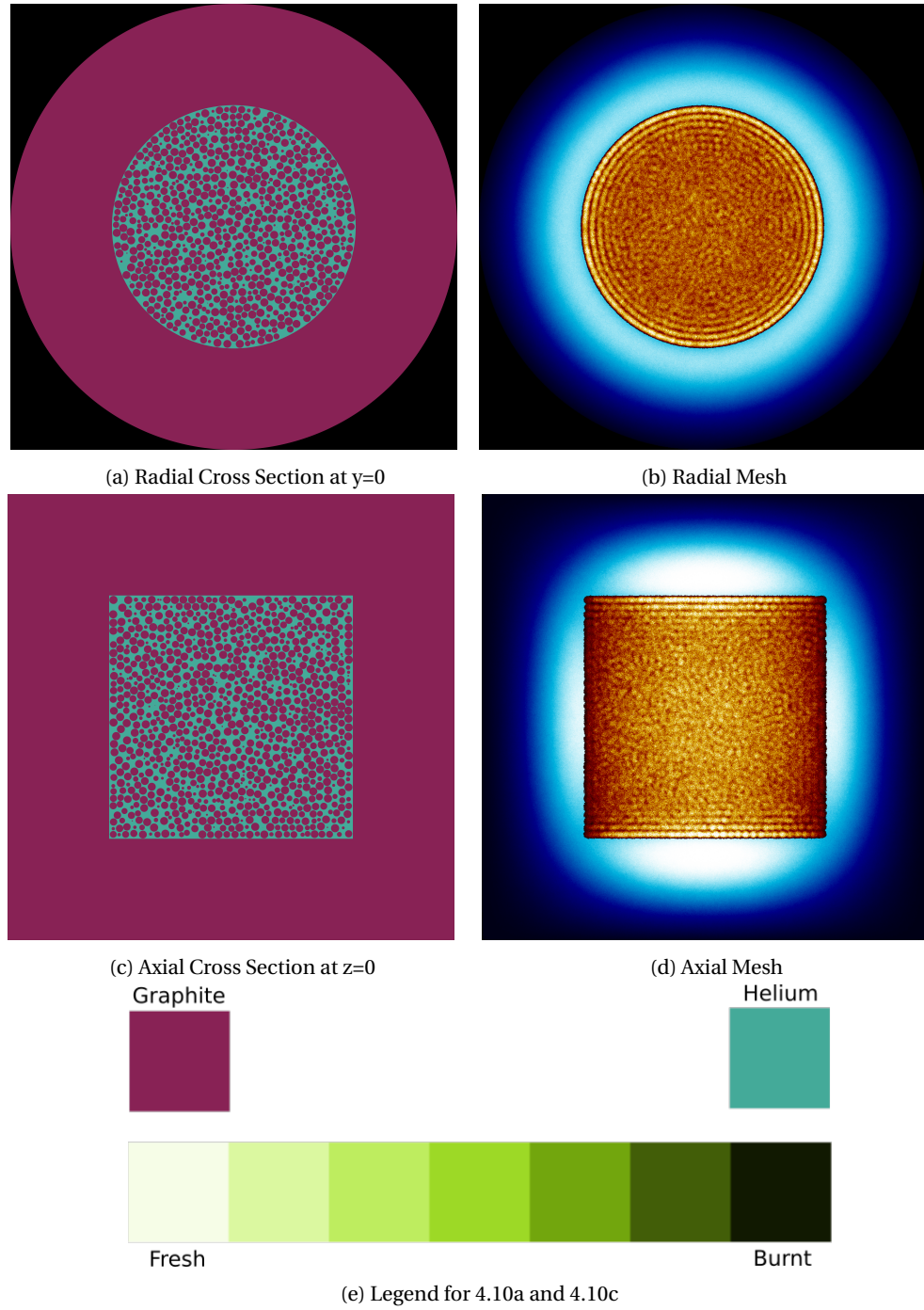


Figure 4.10: Full Core Using Heterogenized Pebbles

The heterogenized-TRISO model reported a  $k_{eff}$  of  $1.056 \pm 0.00033$ . This is significantly higher than the  $k_{eff}$  reported for the control (homogenized-TRISO) model — only  $1.009 \pm 0.00055$ . In agreement with [7], this is a difference of 4.45%.

In 4.10, we can observe the axial and radial fission rates and thermal fluxes of the heterogeneous core. Overall, the mesh result for the heterogenization test fission rate is much the same - the banding patterns are still present, if slightly less defined. In 4.1 below, the run time and CPU usage parameters are provided. CPU usage is defined as the ratio of CPU time to total run time.

Table 4.1: Runtime and CPU Usage Between the Homogenized and Heterogenized Sangamon20 Models

Model	Total CPU Time [minutes]	Running Time [minutes]	CPU Usage
Homogeneous Pebbles	615.61	273.83	2.24815
Heterogeneous Pebbles	915.96	240.75	3.80461

Even though the homogeneous model had a run time that was around 30 minutes longer, it took significantly less CPU time than the heterogeneous model. It is possible that this difference in total run time doesn't occur on average, but more runs are required to test this.

While Figure 4.10 best serves as a qualitative visualization aid, Figures 4.11, 4.12, 4.13, and 4.14 support this in a more quantitative manner. These figures provide the shape and magnitude of the fluxes.

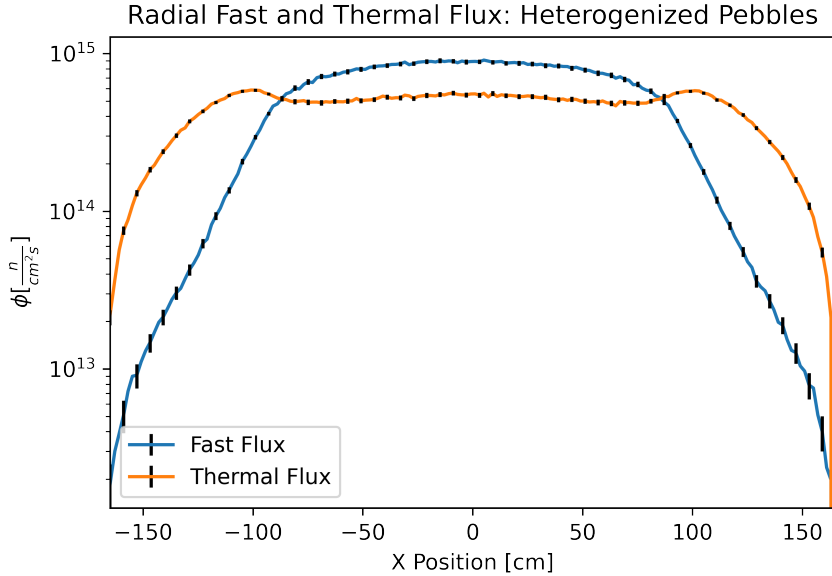


Figure 4.11: Radial Thermal and Fast Flux Profiles along the X-Axis at the Mid-Plane in the Heterogenized-Pebble Sangamon20. Black vertical lines at  $\pm 90$  cm show the inner reflector boundary.

Compared with the homogenized Sangamon20, the heterogenized core reports a slightly lower neutron current at the outer edge of the reflector, at  $6.809 \times 10^{11} \pm 5.515 \times 10^{08}$ , a relative difference of 2.85%. The heterogenized model otherwise shows a similar flux profile to the homogenized model (see Figure 4.17), and experiences a similar level of uncertainty in the outer edges of the reflector for the fast flux profiles, likely due to the significant thermalization of neutrons by that point in the reflector — which results in fewer fast neutrons contributing to outer region tallies.

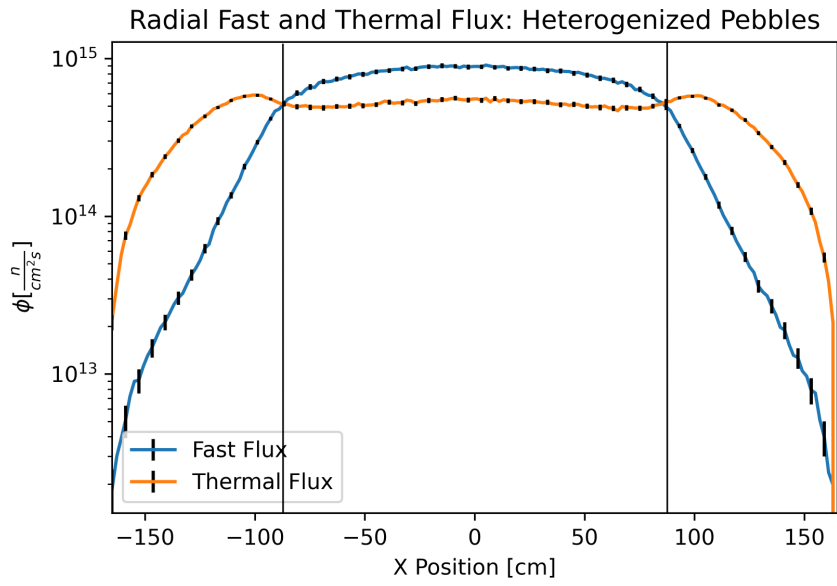


Figure 4.12: Axial Thermal and Fast Flux Profiles along the Z-Axis at the Centerline in the Heterogenized-Pebble Sangamon20. Black vertical lines at  $\pm 90$  cm show the inner reflector boundary.

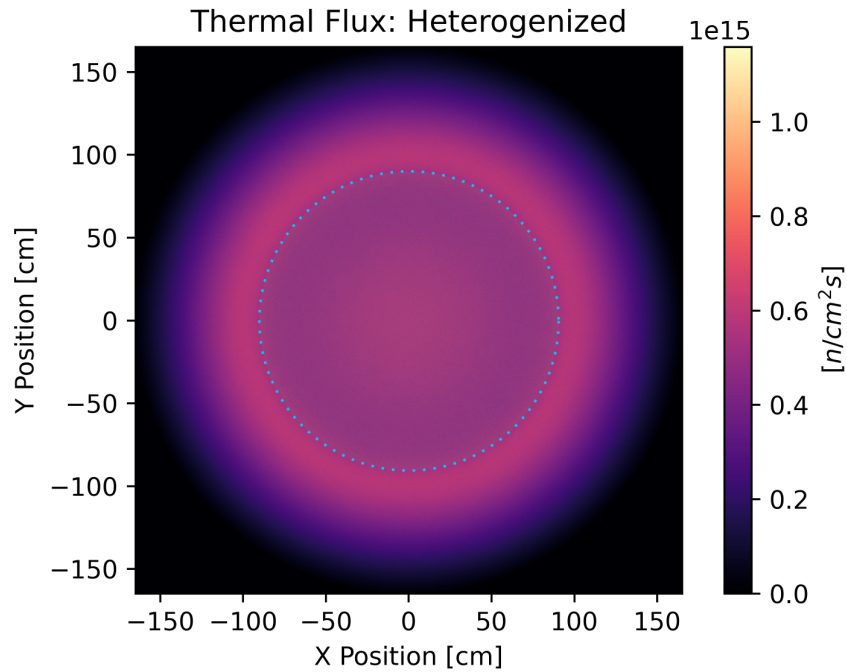


Figure 4.13: Thermal Flux in xy Plane in Sangamon20: Heterogenized Pebbles. The dotted line annotation marks the boundary between the active core and the graphite reflector.

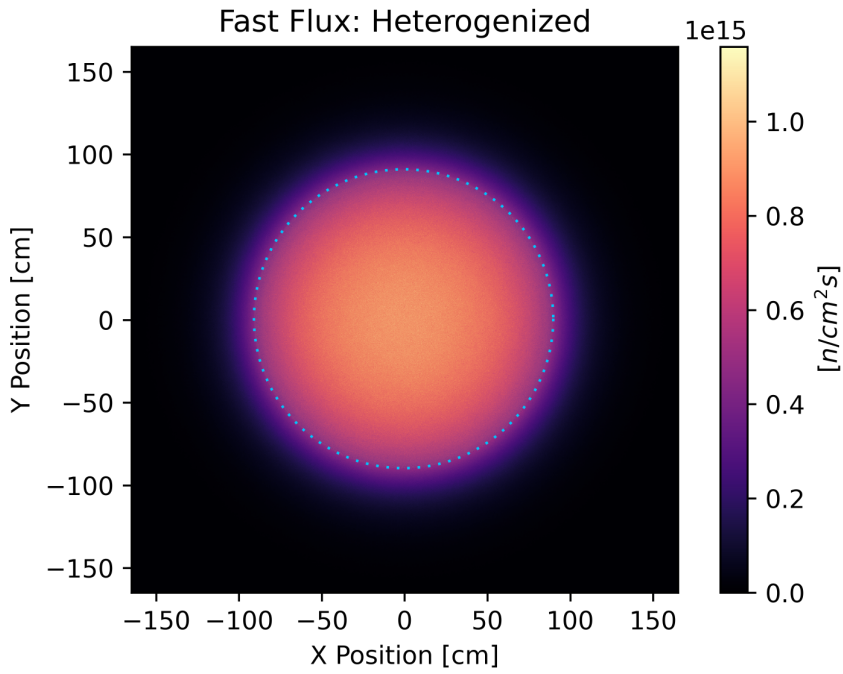


Figure 4.14: Fast Flux in xy Plane in Sangamon20: Heterogenized Pebbles. The dotted line annotation marks the boundary between the active core and the graphite reflector.

Compared with Figures 4.13 and 4.14, the edge pebble bands are much less distinct. This is because the homogenized pebbles have the fissile material spread over the entirety of the 2.5 cm radius fueled center. The heterogenized pebbles, meanwhile, may have the same number of fissile atoms, but they concentrate the regions capable of fission in the TRISO kernel. The rest of the pebble consists of its graphite matrix. This results in a self-shielding effect. Because the fission reactions are not localized to the TRISO kernels, the entire fuel region is more clearly-defined visually in the homogeneous results.

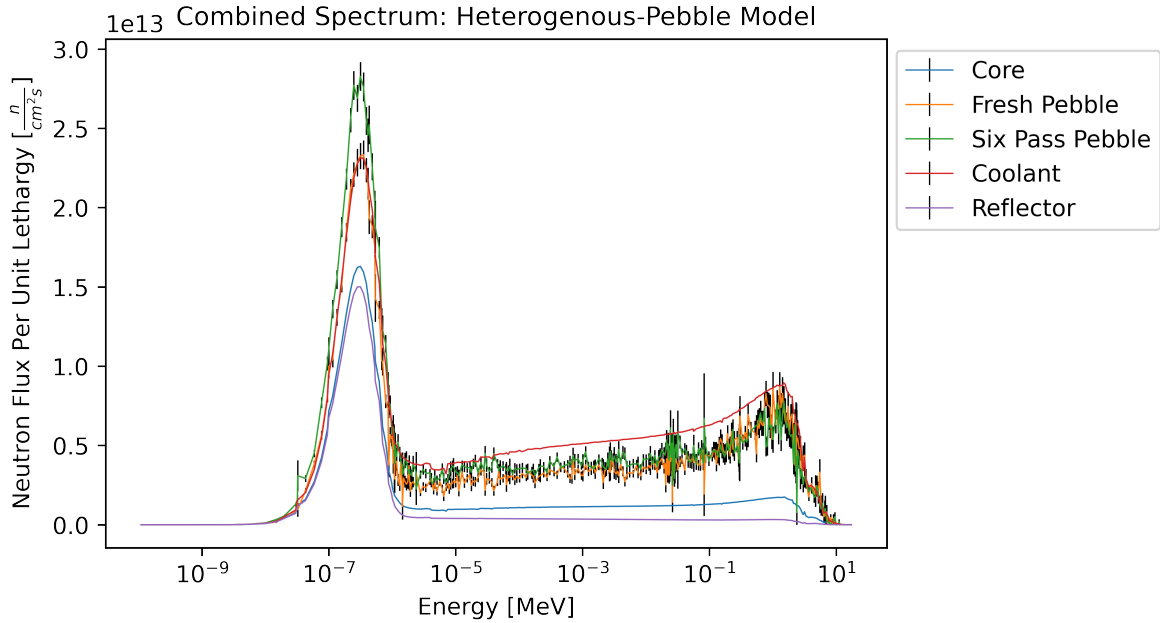


Figure 4.15: Lethargy Adjusted Neutron Flux Energy Spectrum in the Whole-Core for the Heterogenized-Pebble Sangamon20

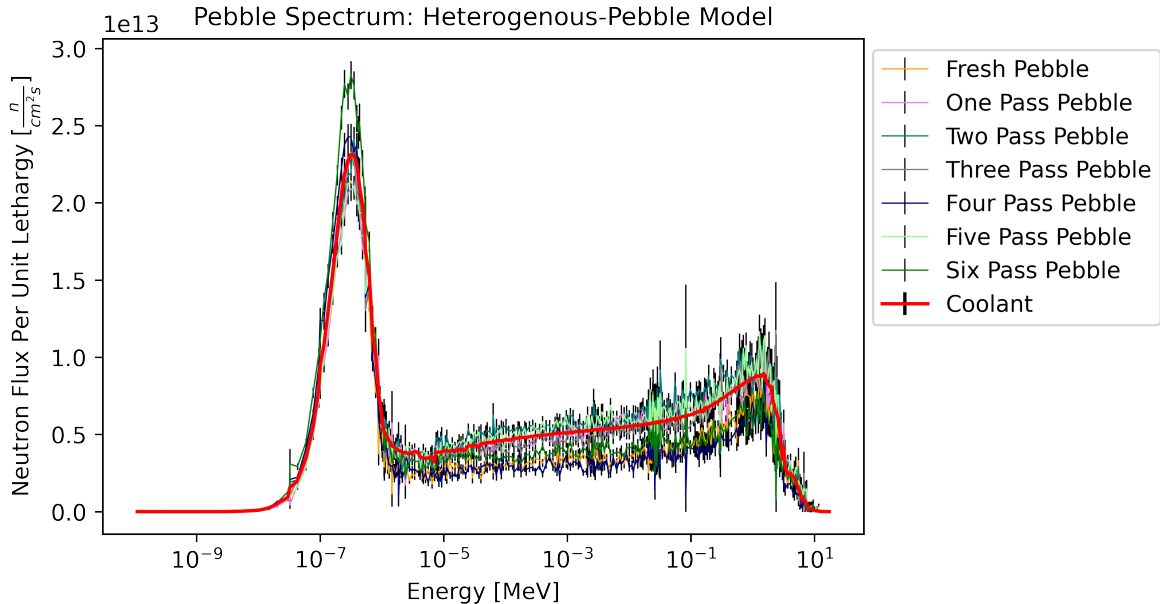


Figure 4.16: Lethargy Adjusted Neutron Flux Energy Spectrum in the Each Pebble Burnup and Coolant for the Heterogenous-Pebble Sangamon20

The spectra for the Sangamon20 core using heterogenized TRISO particles are shown in Figure 4.15. Much like the flux profiles in 4.11 and 4.12, the heterogeneous model's spectra are of a similar morphology to the homogenized spectra. Figure 4.16 shows the pebble spectra for the heterogeneous pebble model, and, much like the combined

pebble and coolant spectra in 4.9, the coolant spectrum roughly follows the average of the pebble spectra.

In order to better examine the differences between the homogenized and heterogenized versions, Figures 4.17 and 4.18 plot the simple relative difference for all spectra, and the radial fast and thermal profiles. The relative difference calculation used the following:

$$\Delta i = \frac{i_{hom} - i_{het}}{i_{het}} \quad (4.2)$$

where

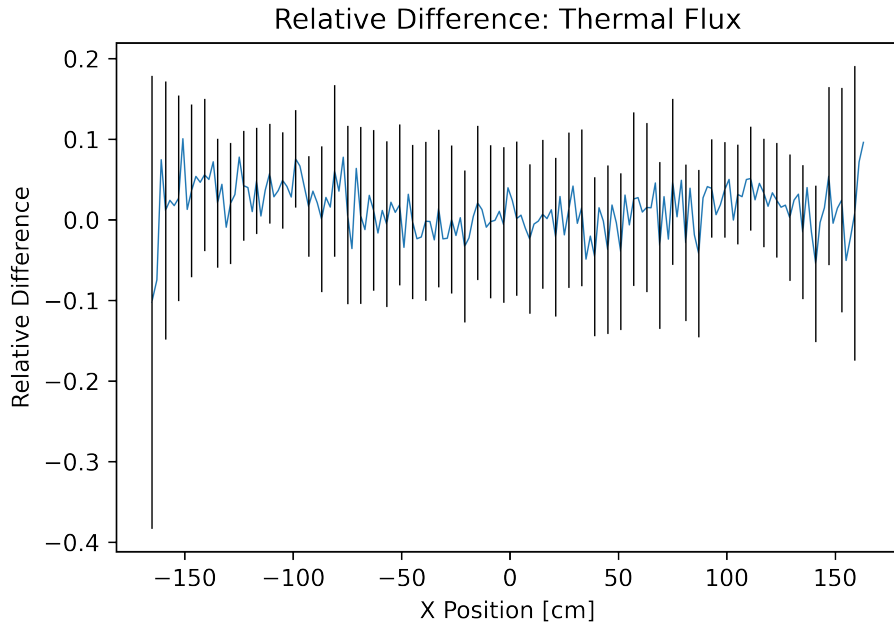
$\Delta i$  = relative difference for parameter  $i$  between homogenized and heterogenized model

$i_{hom}$  = homogenized parameter  $i$

$i_{het}$  = heterogenized parameter  $i$

(4.3)

And error calculation followed error propagation rules as shown in [46].



(a) Thermal Flux

Figure 4.17: Relative Difference in Radial Thermal and Fast Flux Profiles Between Cores Using Homogenized and Heterogenized Pebbles

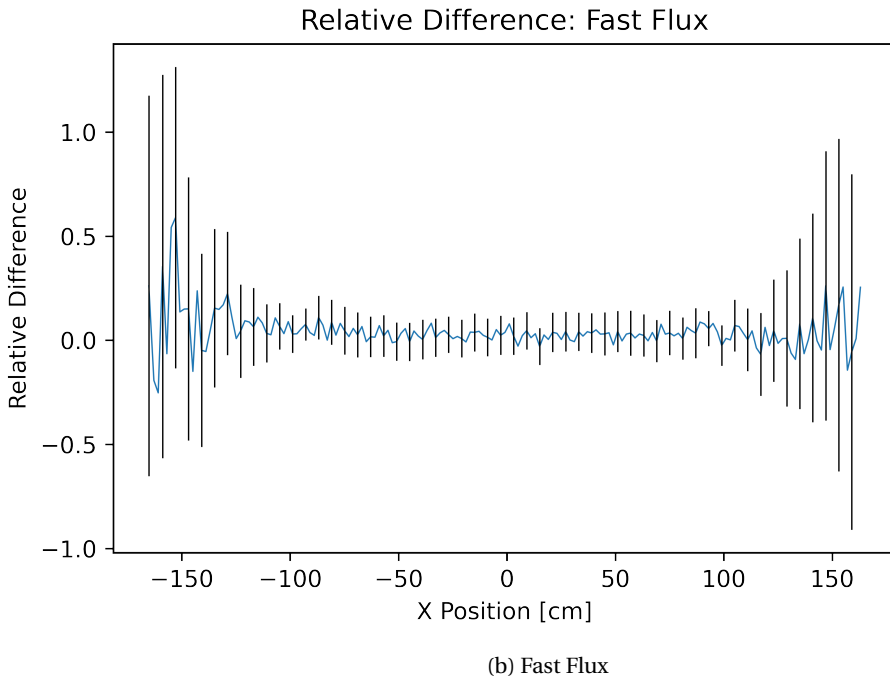


Figure 4.17: (cont.)

The relative difference in the thermal flux is generally between  $\pm 10\%$  for the entire span of the reactor. However, once one accounts for error, it is entirely possible that these differences are wholly accounted for with error alone. The magnitude of the error is fairly constant — except at the edges, where it is much larger. For the fast flux spectrum, the active core region containing the fuel pebbles has a range of  $\pm 10 - 20\%$  relative difference, which is once again accounted for by error. The error on the outer edges in the fast flux plot is much greater than that in the thermal flux, but this is to be expected — as said before, the reflector causes significant thermalization of neutrons entering it, and this means that there are fewer fast neutrons in the reflector to contribute to tallies. For both the thermal and fast fluxes, the value of the relative difference tends to oscillate from one data point to the next. Additionally, the thermal flux's relative difference has two small peaks, each corresponding with the reflector region. These peaks, as shown before, coincide with the actual peaks in the thermal flux 10 cm into the reflector. This is in contrast to the fast flux relative difference profile, which, although it oscillates like the thermal flux, is generally a flat line, and does *not* feature the same center peak that the fast flux does.

For both the thermal and fast flux profiles, relative difference worsens on the outermost edges. Overall, Figures 4.17a and 4.17b suggest that the homogenized simulation is slightly over-predicting the magnitude of the flux when compared to the heterogenized core; however, given the size of the error, these differences do not exist with certainty.

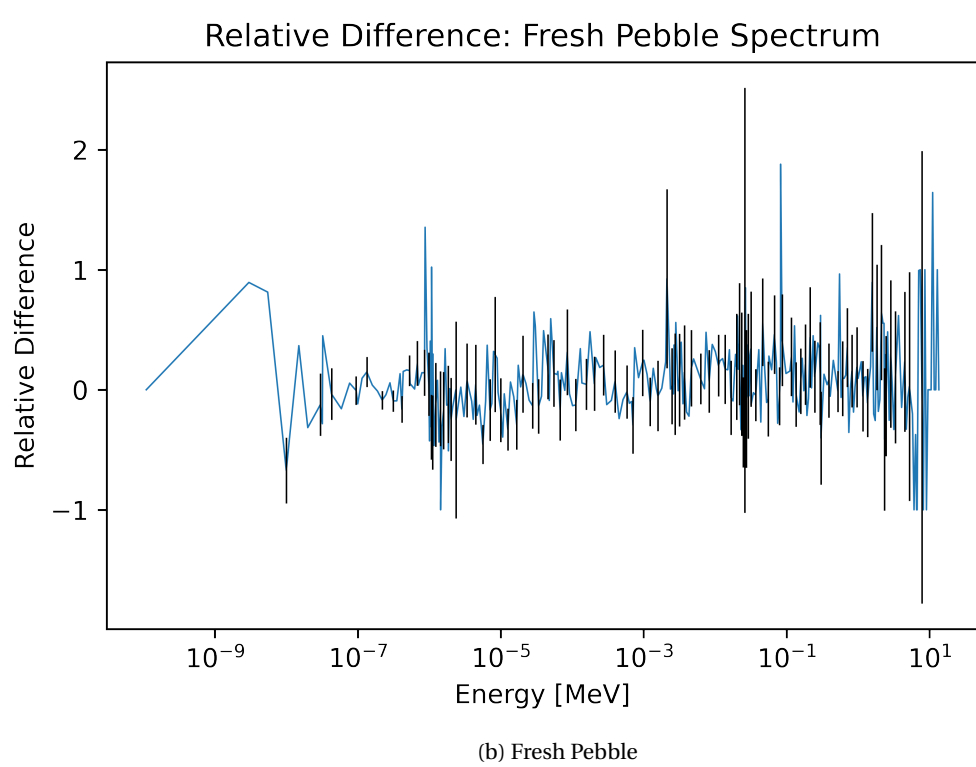
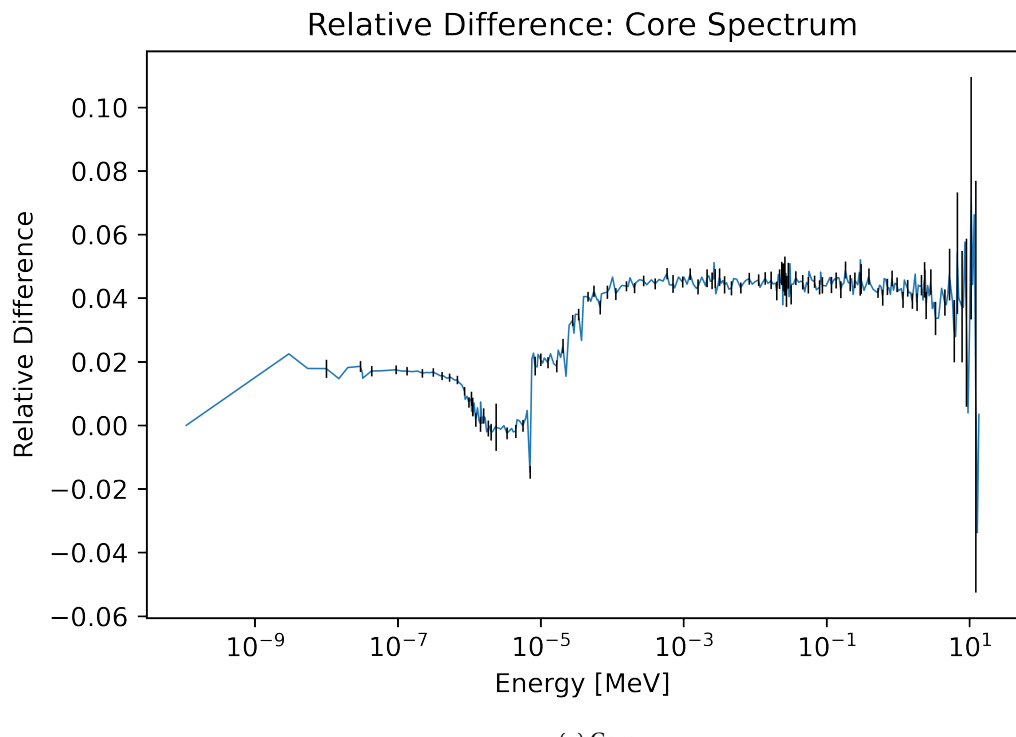


Figure 4.18: Relative Difference in Lethargy Adjusted Neutron Flux Energy Spectra Between Cores using Homogenized and Heterogenized Pebbles

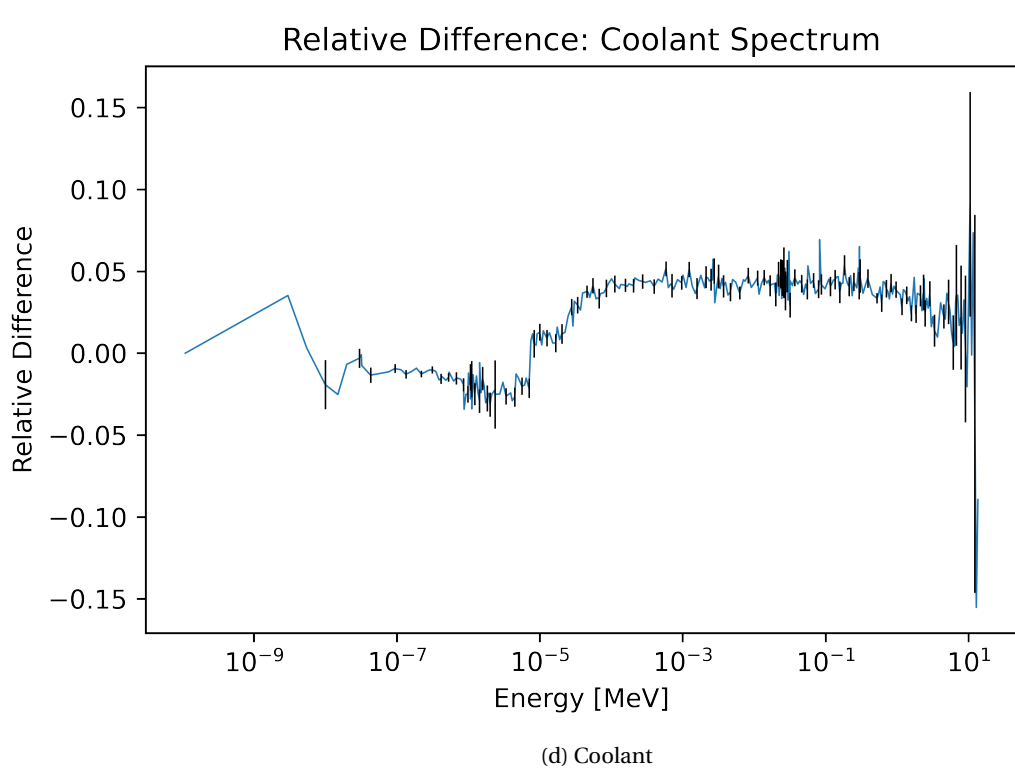
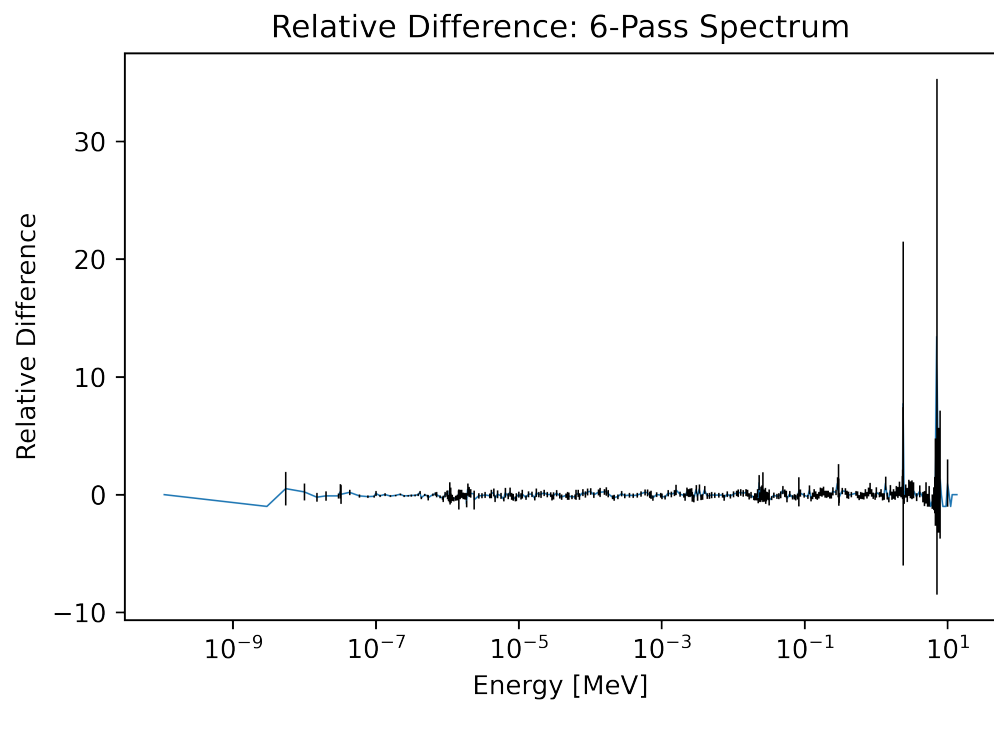


Figure 4.18: (cont.)

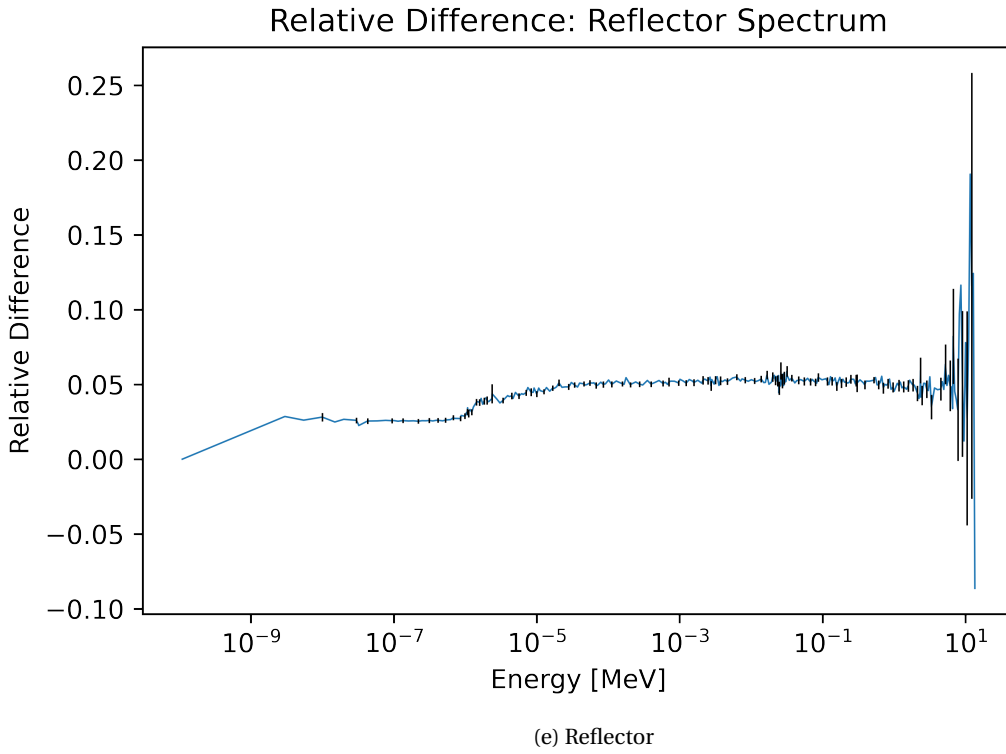


Figure 4.18: (cont.)

Figure 4.18 shows the relative difference in the core, reflector, coolant, and a fresh and six-pass pebble. For all relative difference images in the spectra, a maximum energy cutoff of 13.499 MeV was applied, as data points after this are too inaccurate (due to the low number of tallies in the spectra being compared) and tend to hide the trends in the lower energy ranges. Overall, the homogenized model is over-predicting the thermal peak compared with the heterogeneous model in the core spectra by 5%. Around  $10 \times 10^{-6}$  MeV, at an energy just above the thermal peak, the two spectra agree before diverging again, this time with a slightly greater disagreement. Unlike Figure 4.17, considering only error leaves the relative differences seen in Figure 4.18 unaccounted for (with the exception of the highest neutron energy ranges, and the pebble spectra, which have higher uncertainty).

The pebble spectra in 4.18b and 4.18c have a much greater range of relative difference (greater than 1.0, sometimes spiking to factors of 10+). However, given the wild oscillations and higher error, it is difficult to say with certainty that any of these peaks are "real", and not simply due to error. Future work could consider using a multi-pebble detector to further resolve these differences. This is discussed in Chapter 5.

The coolant and core spectra likely provided a better understanding of the effect of homogenization on neutron energy spectra. The coolant spectra in 4.18d differed after the thermal peak in a magnitude and shape matching the differences in core spectra in 4.18a, showing that the homogeneous model is over-predicting the magnitude of the

faster neutron energy range by around 5%. Unlike the core, however, the coolant has much closer agreement at lower energy levels, including at the thermal peak. The reflector shows a slight over estimation for the homogeneous spectra, which is consistent for all but the highest energy levels (where low tally scores in the compared spectra's detectors may be the cause).

## 4.4 Shuffling and Symmetry Tests

Two additional studies look at the effects of assuming a one-sixth core symmetry, and the effects of changing the fuel composition in each pebble, effectively shuffling the pebbles without re-generating their location. All tests use the homogenized pebble assumption as a base.

### 4.4.1 Effects of Symmetry Assumption

Overall, the effects of using a one-sixth core symmetry were minimal. 4.2 shows the effect of symmetry assumptions on the  $k_{eff}$  and current, and compares them to the control model. In Table 4.2 the relative difference between  $k_{eff}$  and  $J^+$  are calculated between the value provided in the table, and the same parameter in the Sangamon20 control model (see Section 4.2).

Run	$k_{eff}$	$k_{eff} \% \Delta$	$J^+ [\frac{n}{cm^2 s}]$	$J^+ \% \Delta$
Run 1	$1.01019 \pm 0.00054$	0.096%	$7.034 \times 10^{11} \pm 9.988 \times 10^{08}$	0.443%
Run 2	$1.01029 \pm 0.00054$	0.106%	$6.979 \times 10^{11} \pm 9.072 \times 10^{08}$	0.347%
Run 3	$1.01116 \pm 0.00057$	0.192%	$7.016 \times 10^{11} \pm 1.045 \times 10^{09}$	0.187%
Run 4	$1.00753 \pm 0.00053$	0.167%	$7.051 \times 10^{11} \pm 8.320 \times 10^{08}$	0.682%
Run 5	$1.01096 \pm 0.00049$	0.172%	$7.000 \times 10^{11} \pm 9.239 \times 10^{08}$	0.046%
Run 6	$1.00997 \pm 0.00056$	0.074%	$7.000 \times 10^{11} \pm 1.309 \times 10^{09}$	0.046%

Table 4.2: Symmetry Run Results Summary.  $\% \Delta$  differences are compared against the control model.

Figure 4.19 provides cross-sections of the geometry, and fission rate/thermal flux meshes for a one-sixth core symmetry test, in this case Run 1. The fission rate mesh naturally exhibits a six-part repeating pattern, and still shows the banding patterns on the outer edges. Other runs are not shown due to similar features, but can be found in Section B

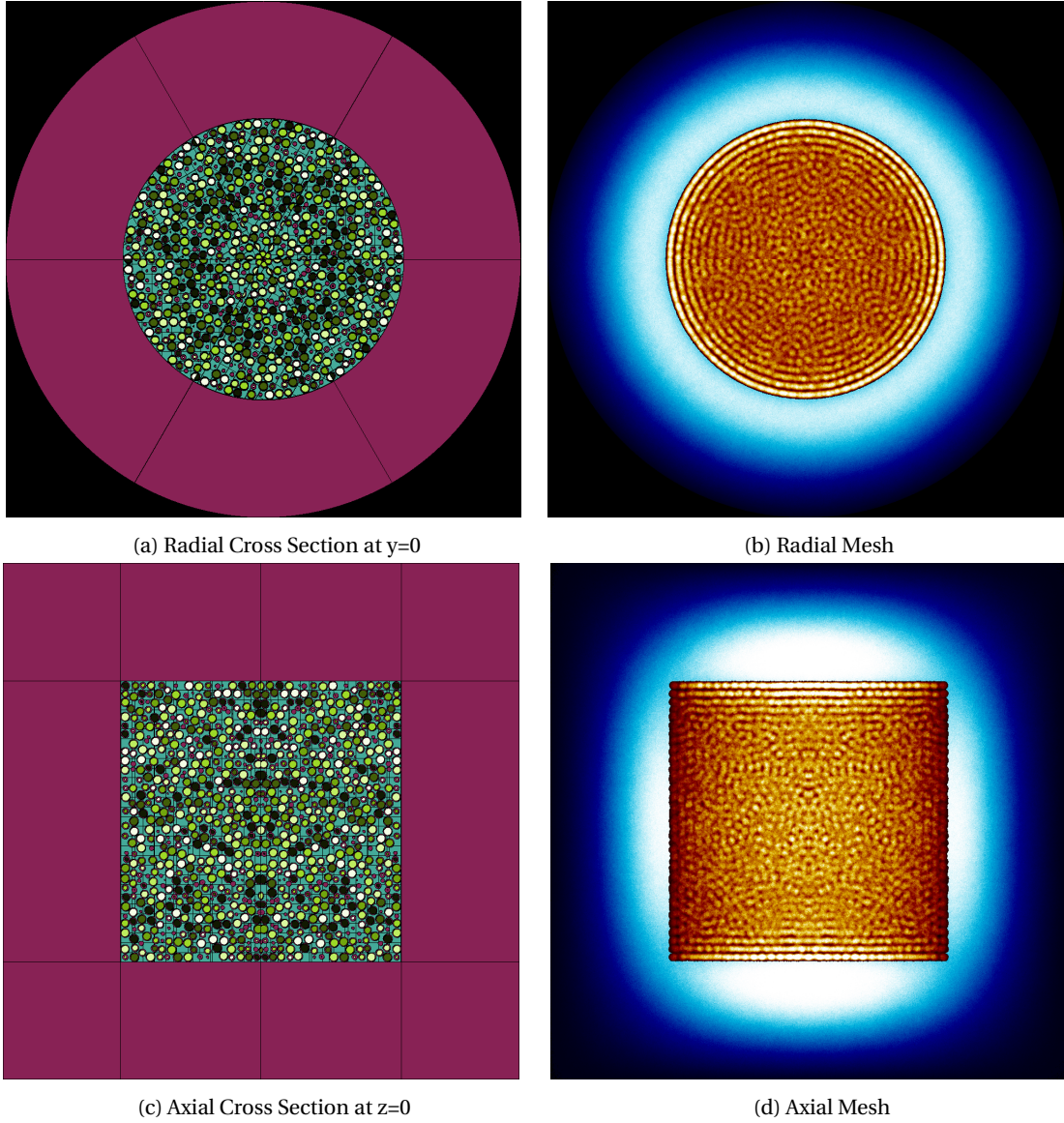


Figure 4.19: Sensitivity Analysis:  $\frac{1}{6}$  Symmetry Using the Portion of the Core Between  $0^\circ - 60^\circ$

One point of interest is the degree to which the region from 0 to 60 degrees matches the same region in the control fission rate mesh. An image subtraction program generated Figure 4.20 by subtracting the radial meshes for the control (Figure 4.3b) and first symmetry test (Figure 4.19b). For a more detailed description of its use, please refer to Section A. Figure 4.20 allows us to more clearly observe where differences are strongest between the models.

Within the region between 0 and 60 degrees, the two meshes are almost identical, pixel for pixel. While this might be unsurprising in the center of this region, the perfect match towards the edges of it are less so. As a reminder, the symmetry tests all use a one-sixth symmetry, and a periodic boundary condition, i.e., if a neutron leaves the slice on one side, it re-enters the slice on the other. In effect, the edges of the 0 to 60 degree slice in the symmetry

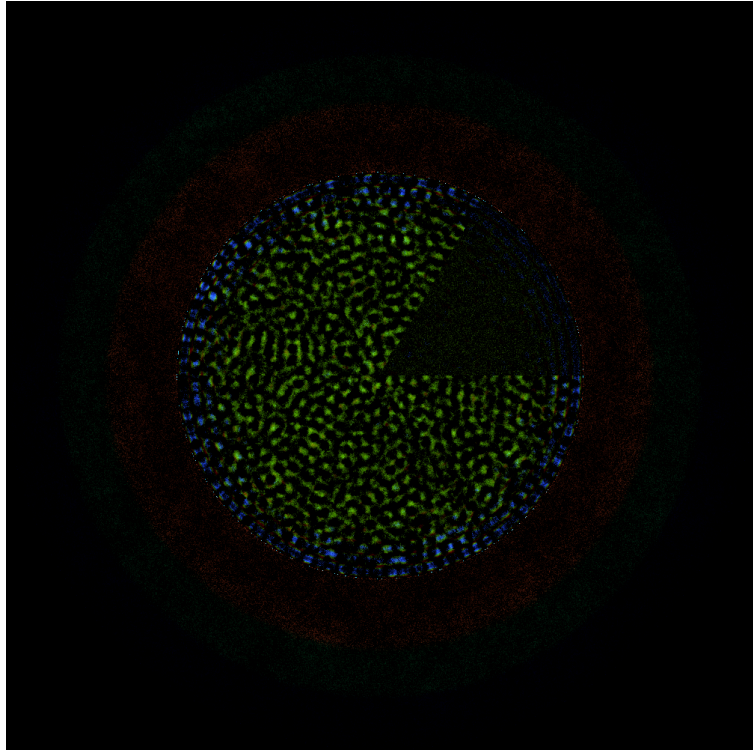


Figure 4.20: An Image Generated by Subtracting 4.19b from 4.3b.

test are seeing entirely different materials, compared with the control. The edges in 4.20 are not a gradient, but rather a hard line, which may suggest that with proper mixing nearest-neighbor pebbles have a relatively lesser impact on core parameters. However, note that Sangamon20 uses only fuel pebbles, and this observation may be false in a reactor design using, for example, absorber pebbles containing something such as boron, or inert pebbles at the edge to protect the reflector. For the results of Symmetry tests 2 through 6, see Section B.

#### 4.4.2 Effects of Pebble Shuffling

The final test on the effects of changes to core modeling is another test of consistency between similar HTGR designs with a different pebble configurations. Rather than re-generate the pebble locations several times, the 'shuffling' test simply reassigns each pebble with a different fuel composition (creating a new input file). For example, the pebbles that were once fresh are now first-pass, the first pass pebbles are now second-pass, and so on. The manual shuffling followed the process outlined in Section 3.7, Table 3.6, and the results of this test are in Table 4.3.

Table 4.3: Shuffling Run Results Summary. % $\Delta$  differences are compared against the control model.

Run	$k_{eff}$	$k_{eff} \text{ \%}\Delta$	$J^+ [\frac{n}{cm^2 s}]$	$J^+ \text{ \%}\Delta$
Run 1	$1.01033 \pm 0.00052$	0.110%	$6.999 \times 10^{11} \pm 9.169 \times 10^{08}$	0.053%
Run 2	$1.01027 \pm 0.00050$	0.104%	$7.026 \times 10^{11} \pm 9.204 \times 10^{08}$	0.328%
Run 3	$1.00910 \pm 0.00058$	0.012%	$7.039 \times 10^{11} \pm 8.587 \times 10^{08}$	0.515%
Run 4	$1.00912 \pm 0.00051$	0.010%	$7.023 \times 10^{11} \pm 9.341 \times 10^{08}$	0.295%
Run 5	$1.00986 \pm 0.00058$	0.063%	$7.005 \times 10^{11} \pm 9.247 \times 10^{08}$	0.032%
Run 6	$1.00981 \pm 0.00054$	0.058%	$7.021 \times 10^{11} \pm 9.619 \times 10^{08}$	0.260%

As with 4.2, 4.3 shows  $k_{eff}$  and the current of each perturbation and compares them to the control. Overall, much like the symmetry test, re-mixing the pebbles had little effect on overall results. Likely, provided the pebbles are sufficiently mixed, and no 'pockets' of like pebbles exist, designs that are otherwise identical should provide similar results. For all geometry cross-sections and thermal flux/fission rate mesh images, and the results of image difference for each run, see Section C.

# Chapter 5

## Conclusion

This chapter provides a synopsis of the work we performed to characterize the Sangamon20 and its sensitivity to modeling simplifications. The first section gives a general summary of the results from the heterogenization (see Section 4.3), symmetry (see Subsection 4.4.1) and shuffling (see Subsection 4.4.2) tests, and discusses them. The second section covers suggested future work

### 5.1 Summary and Discussion

Previous work in HTGR pebble-bed modeling noted that the specific lattice arrangement used had little effect [50], [24], [7]. The pebble-shuffling and symmetry tests support this observation in regard to a random arrangement of the pebbles. Table 5.1 below gives a summary of the range of errors, average error, and the associated control parameter uncertainty for the outward neutron current and  $k_{eff}$  values for the symmetry and shuffling tests.

Table 5.1: Symmetry and Shuffle Test Error Ranges, Average Values, and Uncertainty in the Associated Control Model Value

Parameter	Error Range	Error Average	Associated Control Uncertainty
Outward Current: Symmetry Test	0.682% - 0.046%	0.145%	0.124%
$k_{eff}$ : Symmetry Test	0.192% - 0.074%	0.0789%	$\pm 0.0545\%$
Outward Current: Shuffle Test	0.515% - 0.032%	0.229%	0.124%
$k_{eff}$ : Shuffle Test	0.110% - 0.010%	0.05%	$\pm 0.0545\%$

Overall, the error values in the lower ranges, and the averages, tend to be very near, or less than the uncertainty in the control model. However, the outward current error upper ranges — especially in the symmetry test — can be much greater than the "base" model's uncertainty, by a factor of around 5.5 in the symmetry test. On the whole, the error in  $k_{eff}$  is much less than the error in the outward current, and the shuffling test had lower minimum and maximum error values than the symmetry test — but averaged higher. However, the differences in both were less than the differences observed from heterogenization versus homogenization

The heterogenization tests highlight the need for an accurate representation of TRISO particles. While the overall differences between the fast and thermal flux profiles are within error, the homogenized pebbles will under-predict

$k_{eff}$  by more than 4.0%, while over-predicting the magnitude of the neutron energy lethargy-adjusted flux core spectrum by as much as 5.0% at energies greater than  $10^{-04}$  [MeV]. The most dramatic changes to spectra are within the pebbles themselves, where high-energy neutron peaks are over-estimated in the fresh and sixth-pass pebbles by a factor of 2-4 due to the effects of self-shielding. However, the total outward neutron current, used to gauge the effectiveness of the reflector, differed by only 0.349%. This is likely because the reflector is thick enough to minimize fast neutron leakage, which prevents the fast flux changes (see Figure 4.17b) in the active core from affecting the outer regions of the reflector. The thermal flux isn't changed to a degree unexplained by error (see Figure 4.17a), so the thermal neutron contribution to outward neutron current should be similar to that in the control as well.

For isotopic inventories, most isotopes either increased or decreased at a uniform rate with each pass through the core. However, some isotopes, such as  $^{239}Pu$ , reach a peak concentration in MOL, and subsequently decline. When choosing a multi-pass cycle over an Once Through Then Out (OTTO) fuel cycle, it is important to remember this behavior in the case of fuel failure that may require ejecting a pebble before its final pass.

## 5.2 Future Work

The symmetry test showed that, with random mixing, simplifying the simulation by approximating the whole-core with a  $\frac{1}{6}$  slice had minimal effects on the current and  $k_{eff}$ . However, the 'banding' and petal-like pebble patterns this symmetry creates highlights a potential issue, however unlikely. What if the random pebble dispersal happens to lump a number of the same or similar burnup pebbles together? How would this affect a whole core model, or one using symmetry? Future work could explore the effects of pebble 'lumping', such as the size of pebble-lump needed before it causes a noticeable effect, and what magnitude of effect can be expected.

Additionally, this design used an infinite lattice of like pebbles in the depletion model to arrive at an equilibrium composition. It is possible to improve the accuracy of the equilibrium composition by using other methods. By tracking compositions over time in the actual core, as opposed to an infinite lattice, or splitting the core into axial layers to track the pebble isotopic inventory as a function of the number of passes and current height in the core. This would provide higher-fidelity, time-dependent data on pebble isotopes. From there, an exploration of the resulting source term based on models of varying fidelity could provide insight on the accuracy of fuel composition data required to accurately determine source term and accident consequences.

The current design is slightly supercritical, and one could explore adding in an additional "half-pass" — i.e., half of the sixth-pass pebbles go for a seventh pass, and the other half replaced with fresh pebbles. This change would mean that there are half as many fresh pebbles in the core as there are currently, and the 7th pass pebbles, as they continue to burn in the core, would build up a higher concentration of neutron poisons and other fission

products. This would likely change the magnitude of the fast flux — though it likely wouldn't change the overall shape — and it would have an effect on the coolant and whole-core energy spectra, likely shifting it to lower energy ranges. Alternatively, one could explore the addition of neutron-absorber pebbles to handle excess reactivity.

In the pebble spectra, the small size of a single pebble detector leads to high uncertainties. While the coolant spectrum — which has a much lower uncertainty — can provide a general idea of the averaged pebble spectra, it cannot provide fine detail. A future investigation using a multi-pebble detector will be necessary before the pebble spectra should be used in other calculations or analysis.

Finally, the pebble dispersal method used here does not account for gravity, which would make the pebbles settle closer together. Without using a core that has a diameter which is an integer multiple of the pebble diameter, it is not possible to get a perfect close-pack arrangement (shaking a vessel will help achieve closer packing, but this is not possible here). One could simulate the effects of gravity by dispersing the pebbles over a volume with a slightly shorter height, instead of the full height. One could also split the core into axial layers, and apply a packing fraction equal to the theoretical maximum at the bottom-most layers, and reduce packing fraction as one moves up through the layers. This will require careful tracking of the number of pebbles in each layer if the entire core uses a target number of fuel pebbles, but may provide a better estimate of pebble behavior in a system that does not otherwise incorporate gravity. However, it is important to note that at a packing fraction of around 0.58, the model is already approaching the theoretical maximum packing fraction, so the difference this would make may be minimal. At the same time, as pointed out in [24], even small changes to packing fraction and pebble arrangement may have a significant impact in small, low-leakage systems (such as a well-reflected SMR or microreactor), which is why exploring the effect the aforementioned changes may have could be important, even if the pebble arrangement doesn't appear to change much.

# Bibliography

- [1] Acir Adem et al. "Criticality and burnup analyses of a PBMR-400 full core using Monte Carlo calculation method". In: *Annals of Nuclear Energy* 38.2 (Feb. 1, 2011). Publisher: Pergamon, pp. 298–301. ISSN: 0306-4549. DOI: 10.1016/j.anucene.2010.10.013.
- [2] Felipe Albornoz and Sergio Korochinsky. "MCNP Modelling of the PBMR Equilibrium Core". In: *Proceedings of the International Conference on Physics of Reactors 2006*. International Conference on Physics of Reactors 2006. Vancouver, BC, Canada, Jan. 2006.
- [3] R.S. Babcock et al. *MOCUP: MCNP-ORIGEN2 coupling utility programs*. CONF-9505218 INIS Reference Number: 36023841. International Atomic Energy Agency (IAEA), 1995, pp. 318–334.
- [4] R. Bäumer et al. "Construction and operating experience with the 300-MW THTR nuclear power plant". In: *Nuclear Engineering and Design* 121.2 (July 2, 1990), pp. 155–166. ISSN: 0029-5493. DOI: 10.1016/0029-5493(90)90100-C.
- [5] J M Beck and L F Pincock. *High Temperature Gas-cooled Reactors Lessons Learned Applicable to the Next Generation Nuclear Plant*. INL/EXT-10-19329. INL, Apr. 2011, p. 78.
- [6] Friederike Bostelmann et al. "Criticality calculations of the Very High Temperature Reactor Critical Assembly benchmark with Serpent and SCALE/KENO-VI". In: *Annals of Nuclear Energy* 90 (Apr. 1, 2016), pp. 343–352. ISSN: 0306-4549. DOI: 10.1016/j.anucene.2015.12.008.
- [7] Forrest B Brown et al. "STOCHASTIC GEOMETRY AND HTGR MODELING WITH MCNP5". In: *Proceedings of the Monte Carlo 2005 Topical Meeting - The Monte Carlo Method Conference*. Conference: Monte Carlo 2005 Topical Meeting - The Monte Carlo Method: Versatility Unbounded In A Dynamic Computing World. Chattanooga, Tennessee: American Nuclear Society, 2005, p. 13.
- [8] E. Brun et al. "TRIPOLI-4®, CEA, EDF and AREVA reference Monte Carlo code". In: *Annals of Nuclear Energy*. Joint International Conference on Supercomputing in Nuclear Applications and Monte Carlo 2013, SNA + MC 2013. Pluri- and Trans-disciplinarity, Towards New Modeling and Numerical Simulation Paradigms 82 (Aug. 1, 2015), pp. 151–160. ISSN: 0306-4549. DOI: 10.1016/j.anucene.2014.07.053.

- [9] Anselmo Tomas Cisneros. “Pebble Bed Reactors Design Optimization Methods and their Application to the Pebble Bed Fluoride Salt Cooled High Temperature Reactor (PB-FHR)”. PhD thesis. University of California Berkeley, 2013. URL: <http://gradworks.umi.com/36/16/3616613.html>.
- [10] Cole Gentry. *generate random particle or pebble bed files for HTGR calc - Discussion forum for Serpent users.* Discussion Forum for Serpent Users. Sept. 29, 2015. URL: <https://ttuki.vtt.fi/serpent/viewtopic.php?f=3&t=2267&p=6161&hilit=growth+and+shake#p6161>.
- [11] Allen G. Croff. “ORIGEN2: A Versatile Computer Code for Calculating the Nuclide Compositions and Characteristics of Nuclear Materials”. In: *Nuclear Technology* 62.3 (Sept. 1, 1983). Publisher: Taylor & Francis \_eprint: <https://doi.org/10.13182/NT83-1>, pp. 335–352. ISSN: 0029-5450. DOI: 10.13182/NT83-1.
- [12] F. Daniels. *SUGGESTIONS FOR A HIGH TEMPERATURE PEBBLE PILE*. MUC-FD-8. University of Chicago Metallurgical Laboratory, 1944. DOI: 10.2172/4359817.
- [13] GEN IV International Forum. *GIF 2020 Annual Report*. 13. GIF, 2021. URL: [https://www.gen-4.org/gif/jcms/c\\_178286/gif-2020-annual-report?details=true](https://www.gen-4.org/gif/jcms/c_178286/gif-2020-annual-report?details=true).
- [14] H. Gottsaut and Krüger. “Results of experiments at the AVR reactor”. In: *Nuclear Engineering and Design* 121.2 (July 2, 1990). Publisher: North-Holland, pp. 143–153. ISSN: 0029-5493. DOI: 10.1016/0029-5493(90)90099-J.
- [15] C. J. Hamilton et al. *HTGR spent fuel composition and fuel element block flow*. GA-A-13886(Vol.1). GA-A13886. General Atomic Co., San Diego, Calif. (USA), July 1, 1976. DOI: 10.2172/7157851.
- [16] Bowers Harlan. “ANS Xe 100 Overview 2017”. DC ANS April Meeting, Apr. 5, 2017. URL: [http://www.dcssection.org/wp-content/uploads/2014/01/ANS\\_Xe-100-Overview\\_04052017.pdf](http://www.dcssection.org/wp-content/uploads/2014/01/ANS_Xe-100-Overview_04052017.pdf).
- [17] Bowers Harlan. “X-energy Xe-100 Reactor initial NRC meeting”. Xe-100 Reactor initial NRC meeting. Rockville, MD, Sept. 11, 2018. URL: <https://www.nrc.gov/docs/ML1825/ML18253A109.pdf>.
- [18] Charles R. Harris et al. “Array programming with NumPy”. In: *Nature* 585.7825 (Sept. 2020), pp. 357–362. ISSN: 1476-4687. DOI: 10.1038/s41586-020-2649-2.
- [19] Grant W. Helmreich et al. *Year One Summary of X-energy Pebble Fuel Development at ORNL*. ORNL/TM-2017/337. Oak Ridge National Lab. (ORNL), Oak Ridge, TN (United States), June 1, 2017. DOI: 10.2172/1376502.
- [20] H. G. Hereward et al. “Measurement of the Diffusion Length of Thermal Neutrons in Graphite”. In: *Canadian Journal of Research* 25a.1 (Jan. 1, 1947). Publisher: NRC Research Press, pp. 15–25. ISSN: 1923-4287. DOI: 10.1139/cjr47a-002.

- [21] F.H. Ho, R. Vollmar, and R. Turner. *Graphite design handbook*. Sept. 1988. URL: <https://www.osti.gov/servlets/purl/714896/>.
- [22] INL. *Basis for NGNP Reactor Design Down-Selection*. Nov. 2011. URL: <https://inldigitallibrary.inl.gov/sites/sti/sti/5223031.pdf>.
- [23] W.R. Johnson and G.B. Engle. *Properties of unirradiated fuel element graphites H-451 and TS-1240*. GA-A-13752, 7283150. Jan. 31, 1976, GA-A-13752, 7283150. DOI: 10.2172/7283150.
- [24] Z. Karriem, C. Stoker, and F Reitsma. “MCNP Modelling of HTGR Pebble-Type Fuel”. In: *Proceedings of the Monte Carlo 2000 Conference*. Monte Carlo 2000 Conference. Ed. by Andreas Kling et al. Lisbon: Springer, 2001, pp. 841–846. ISBN: 978-3-642-18211-2. DOI: 10.1007/978-3-642-18211-2\_134.
- [25] Hong-Chul Kim et al. “Monte Carlo Benchmark Calculations for HTR-10 Initial Core”. In: *Proceedings of the Korean Nuclear Society Conference* (2005). Publisher: Korean Nuclear Society, pp. 5–6. URL: <https://www.koreascience.or.kr/article/CFK0200533239312837.page>.
- [26] N. Lenssen et al. “Improvements in the GISTEMP uncertainty model”. In: *J. Geophys. Res. Atmos.* 124.12 (2019), pp. 6307–6326. DOI: 10.1029/2018JD029522.
- [27] Jaakko Leppänen. *Serpent – a Continuous-energy Monte Carlo Reactor Physics Burnup Calculation Code*. June 18, 2015. URL: [http://montecarlo.vtt.fi/download/Serpent\\_manual.pdf](http://montecarlo.vtt.fi/download/Serpent_manual.pdf).
- [28] Jaakko Leppänen et al. “The Serpent Monte Carlo code: Status, development and applications in 2013”. In: *Annals of Nuclear Energy*. Joint International Conference on Supercomputing in Nuclear Applications and Monte Carlo 2013, SNA + MC 2013. Pluri- and Trans-disciplinarity, Towards New Modeling and Numerical Simulation Paradigms 82 (Aug. 1, 2015), pp. 142–150. ISSN: 0306-4549. DOI: 10.1016/j.anucene.2014.08.024.
- [29] Shichang Liu et al. “Random geometry capability in RMC code for explicit analysis of polytype particle/pebble and applications to HTR-10 benchmark”. In: *Annals of Nuclear Energy* 111 (Jan. 1, 2018), pp. 41–49. ISSN: 0306-4549. DOI: 10.1016/j.anucene.2017.08.063.
- [30] Robert G Mortimer. “The Behavior of Gases and Liquids”. In: *Physical Chemistry*. 3rd. Rhodes College: Elsevier Academic Press, 2008, p. 5. ISBN: 13: 978-0-12-370617-1.
- [31] Isao MURATA et al. “New Sampling Method in Continuous Energy Monte Carlo Calculation for Pebble Bed Reactors”. In: *Journal of Nuclear Science and Technology* 34.8 (Aug. 1, 1997). Publisher: Taylor & Francis \_eprint: <https://doi.org/10.1080/18811248.1997.9733737>, pp. 734–744. ISSN: 0022-3131. DOI: 10.1080/18811248.1997.9733737.

- [32] OECD NEA. *NEA Benchmark of the Modular High-Temperature Gas-Cooled Reactor-350 MW Core Design Volumes I and II*. Feb. 16, 2018.
- [33] OECD and NEA. “IRPhe Handbook 2013”. In: (2019). ISSN: 26175614. DOI: 10.1787/8d549c0f-en.
- [34] Jeffrey A Phillips, Eric L Shaber, and Scott G Nagley. “FABRICATION OF URANIUM OXYCARBIDE KERNELS AND COMPACTS FOR HTR FUEL”. In: *Nuclear Engineering and Design* 251.0 (Oct. 2012). ISSN: 0029-5493. DOI: 10.1016/j.nucengdes.2011.10.033.
- [35] Frederik Reitsma et al. “INVESTIGATION OF THE POWER PEAKING IN THE PBMR PEBBLE- BED REACTOR”. In: *Proceedings of the Mathematics and Computation, Supercomputing, Reactor Physics and Nuclear and Biological Applications Conference*. Mathematics and Computation, Supercomputing, Reactor Physics and Nuclear and Biological Applications. Palais des Papes, Avignon, France, 2005, p. 13.
- [36] H. Reutler and G. H. Lohnert. “Advantages of going modular in HTRs”. In: *Nuclear Engineering and Design* 78.2 (Apr. 1, 1984), pp. 129–136. ISSN: 0029-5493. DOI: 10.1016/0029-5493(84)90298-X.
- [37] Zoe Richter. *Isotopic Fuel Compositions in the Sangamon20 Model*. Type: dataset. Sept. 11, 2021. DOI: 10.5281/zenodo.5501385.
- [38] Zoe Richter. *Isotopic Fuel Compositions in the Sangamon200 Model*. Type: dataset. Apr. 8, 2022. DOI: 10.5281/zenodo.6426312.
- [39] Zoë Richter et al. *ZoeRichter/phlox: Version 1.1*. Apr. 12, 2022. DOI: 10.5281/zenodo.6451576.
- [40] H.J. Ruetten et al. *VSOP (99/05) computer code system*. 0944-2952. Juel-4189 INIS Reference Number: 37024454. Germany, 2005, p. 172.
- [41] Anthony Scopatz et al. “PyNE: Python for Nuclear Engineering”. In: *Proceedings of the American Nuclear Society Winter Conference*. American Nuclear Society Winter Conference. Vol. 107. Reactor Physics: General—I. San Diego, CA, USA: American Nuclear Society, Nov. 11, 2012, pp. 985–987. URL: <http://epubs.ans.org/?a=14978>.
- [42] Ding She et al. “EXPLICIT MODELLING OF DOUBLE-HETEROGENEOUS PEBBLE- BED REACTORS WITH THE RMC CODE”. In: *Proceedings of the American Nuclear Society MC2015 Conference*. ANS MC2015 - Joint International Conference on Mathematics and Computation (M&C), Supercomputing in Nuclear Applications (SNA) and the Monte Carlo (MC) Method. Nashville, TN, Apr. 2015.
- [43] S. Shiozawa et al. “Overview of HTTR design features”. In: *Nuclear Engineering and Design*. Japan’s HTTR 233.1 (Oct. 1, 2004), pp. 11–21. ISSN: 0029-5493. DOI: 10.1016/j.nucengdes.2004.07.016.

- [44] Massoud T. Simnad. "The early history of high-temperature helium gas-cooled nuclear power reactors". In: *Energy*. High-temperature Helium Gas-cooled Nuclear reactors: Past Experience Current Status and Future Prospects 16.1 (Jan. 1, 1991), pp. 25–32. ISSN: 0360-5442. DOI: 10.1016/0360-5442(91)90084-Y.
- [45] T.K. Kim et al. *Whole-Core Depletion Studies in Support of Fuel Specification for the Next Generation Nuclear Plant (NGNP) Core*. Argonne National Laboratory, July 30, 2004. URL: <https://publications.anl.gov/anlpubs/2004/11/51497.pdf>.
- [46] John Taylor. "Chapter 3: Propagation of Uncertainties". In: *An Introduction to Error Analysis: The Study of Uncertainties in Physical Measurements*. Second. University of Colorado: University Science Books, 1997, pp. 45–79.
- [47] GISTEMP Team. *GISS Surface Temperature Analysis (GISTEMP), version 4*. NASA Goddard Institute for Space Studies, 2022. URL: [data.giss.nasa.gov/gistemp/](http://data.giss.nasa.gov/gistemp/).
- [48] W.K. Terry, H.D. Gougar, and A.M. Ougouag. "Direct deterministic method for neutronics analysis and computation of asymptotic burnup distribution in a recirculating pebble-bed reactor". In: *Annals of Nuclear Energy* 29.11 (July 2002), pp. 1345–1364. ISSN: 03064549. DOI: 10.1016/S0306-4549(01)00110-4.
- [49] Sai S Tulluri. "Analysis of random packing of uniform spheres using the Monte Carlo simulation method". Masters of Science Thesis. New Jersey Institute of Technology, May 2003.
- [50] Mehmet Türkmen and Üner Çolak. "Effect of pebble packing on neutron spectrum and the isotopic composition of HTGR fuel". In: *Annals of Nuclear Energy* 46 (Aug. 1, 2012), pp. 29–36. ISSN: 0306-4549. DOI: 10.1016/j.anucene.2012.03.016.
- [51] Guido Van Rossum and Fred L. Drake. *Python 3 Reference Manual*. Scotts Valley, CA: CreateSpace, 2009. ISBN: 1-4414-1269-7.
- [52] Pieter J Venter, Mark N Mitchell, and Fred Fortier. "PBMR REACTOR DESIGN AND DEVELOPMENT". In: *Proceedings of the 18th International Conference on Structural Mechanics in Reactor Technology*. 18th International Conference on Structural Mechanics in Reactor Technology. 2005.
- [53] R. F. Walker. "Experience with the Fort St. Vrain reactor". In: *Annals of Nuclear Energy*. Thorium and Gas Cooled Reactors 5.8 (Jan. 1, 1978), pp. 337–356. ISSN: 0306-4549. DOI: 10.1016/0306-4549(78)90018-X.
- [54] Christopher Werner, ed. *MCNP User Manual, Code Version 6.2 LA-UR-17-29981*. Oct. 27, 2017. URL: [https://laws.lanl.gov/vhosts/mcnp.lanl.gov/pdf\\_files/la-ur-17-29981.pdf](https://laws.lanl.gov/vhosts/mcnp.lanl.gov/pdf_files/la-ur-17-29981.pdf).

# Appendices

The Appendix first provides an explanation of color theory as it pertains to digital RGB color. This is to aid an unfamiliar reader with interpreting the many image difference results in the appendices. Section B then moves to the complete results of the symmetry test, which were omitted from the main body of the report for the sake of brevity.

## A Image Difference and RGB Color

To help explain the color difference plots later in the Appendix, it may be helpful to go into further depth on RGB (red, green, blue) based colors and how the individual values correspond to colors when mixed.

In the RGB color format, values for red, green, and blue can range from 0 to 255. The higher the value for a color, the more of it is present in the resulting color. If the values for red, green, and blue are the same, then the resulting color is a shade of grey. If all values are set to their maximum, 255, then the result is pure white. If all values are 0, then the result is pure black. In general, colors with low RGB values are darker than ones with greater RGB values.

To understand why the differences in the active core are in green (see Figure 5 for an example), it is useful to revisit color theory and complementary colors. The fission rate meshes are shown in a hot color map, which ranges in color from an almost-white shade of yellow, to very dark browns. In between these maximum and minimum shades are varying shades of yellow, orange, and brown. To create a shade of yellow in RGB format, one uses a large amount of red and green. To create the sort of almost-white yellow, one simply takes the base yellow, with large amounts of red and green, and increases the blue value (which, as described before, will transition the color to a lighter shade as all three RGB values approach the maximum of 255). To move from yellow to an orangey-brown, one shifts the green value down. Lowering red and green while keeping blue at a low value produces the darkest shades of brown seen in the color map.

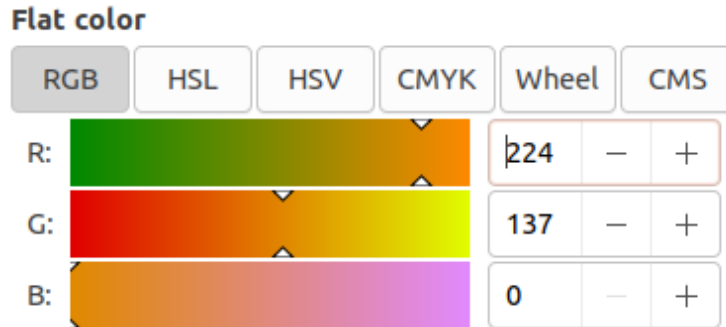


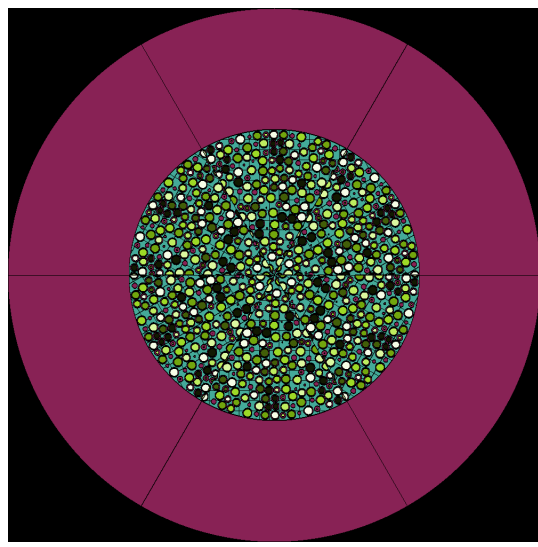
Figure 1: An example of RGB values. If the value for red and blue are held constant, shifting the value for green up or down shifts the resulting color along the color gradient to the left of the green value, which ranges from red to yellow. The arrows on the green gradient indicate what the current color is. As one can see, moving the slider to the right - increasing the value of green - will make the color more yellow, while moving it to the left, or decreasing the green level, will shift it towards orange and red.

Figure 1 gives an example of selecting a color using RGB values. Image difference works by subtracting the RGB values from each other - for example, subtracting (200, 150, 50) from (100, 200, 75) results in (100, 50, 25). Absolute values are used because negative values don't exist in RGB colors. So, when two colors which have contrasting values of green, and similar values of red and blue, the result is, of course, a shade of green. The image difference results in the "banded" regions at the outermost edges of the active core shift to blue from green simply because in the original images this region is already in the yellow to white color range, and so the only RGB value that changes is blue.

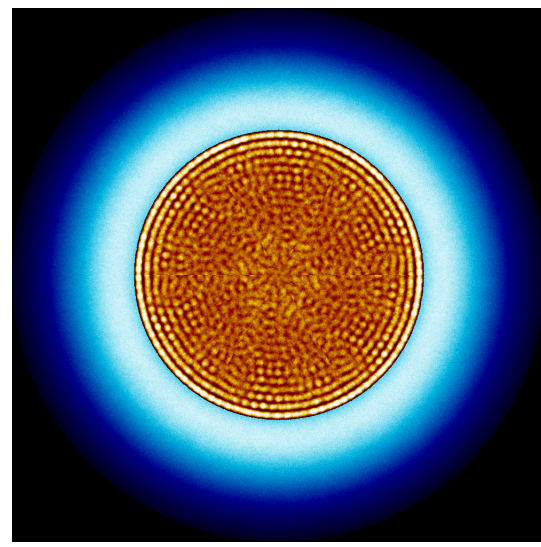
One can imagine the two extremes that an image difference could give - pure black, or RGB (0, 0, 0) means the two images were identical at that particular pixel. Meanwhile, pure white — (255, 255, 255) — is the greatest possible difference that could exist. Therefore, when interpreting the image difference results in Section B and Section C, it is important to keep in mind that the specific *color* the differences are shown in — usually green, but also blue or, rarely, red — are far less important than how bright, or intense, these colors are.

## B Symmetry Test

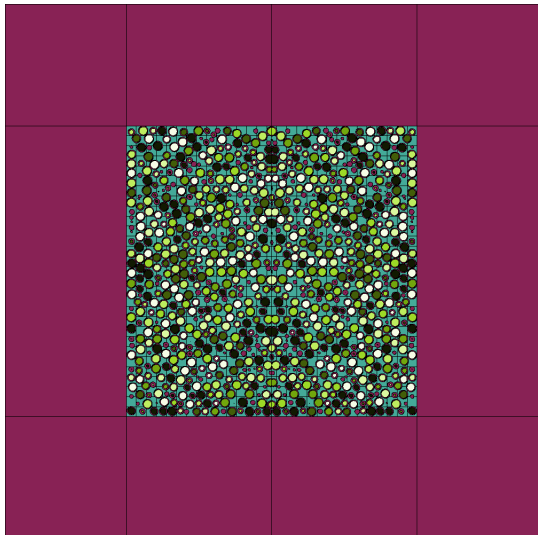
Section B contains the geometry cross sections, fission rate/thermal flux meshes, and image difference results from the other symmetry tests, corresponding to Run 2 through Run 5 in Figure 3.7. These symmetry test use an otherwise identical core model and set of run parameters (see Section 3.2) for the Sangamon20 core model. Image difference for each run compares to the Sangamon20 control model results.



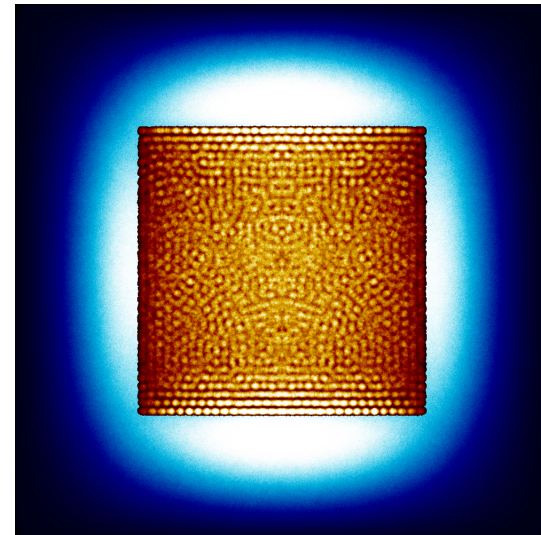
(a) Radial Cross Section at  $y=0$



(b) Radial Mesh



(c) Axial Cross Section at  $z=0$



(d) Axial Mesh

Figure 2: Sensitivity Analysis:  $\frac{1}{6}$  Symmetry Using the Portion of the Core Between  $60^\circ - 120^\circ$

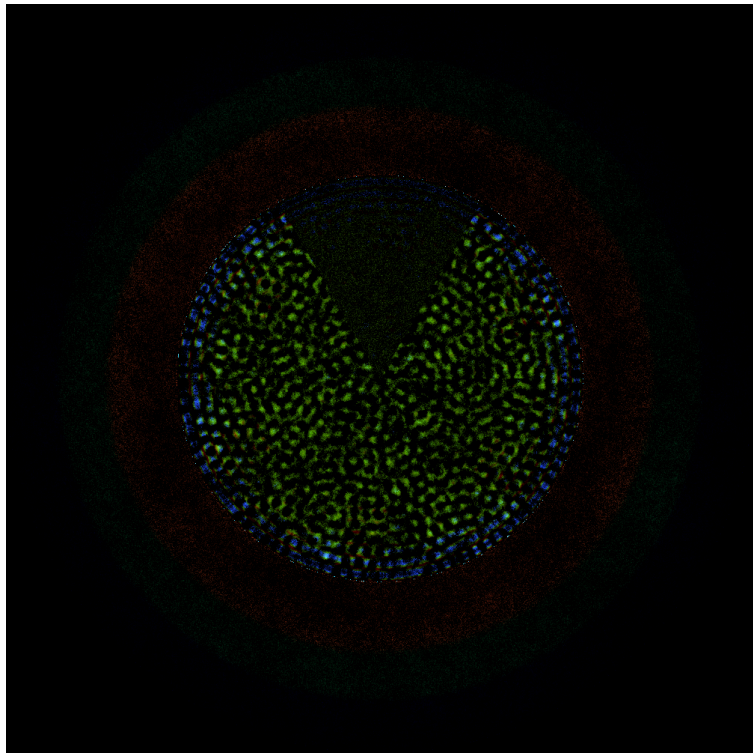
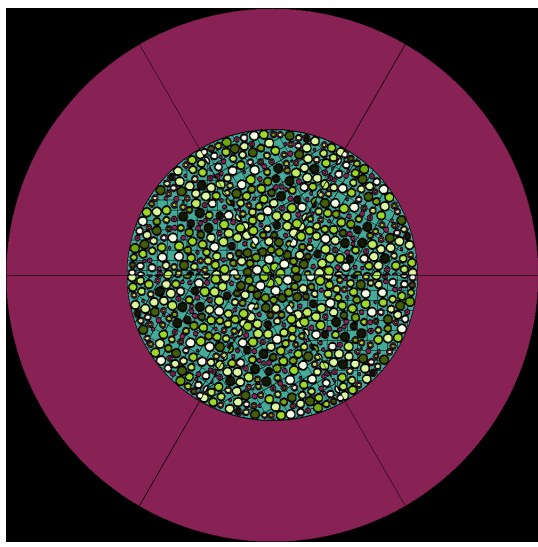
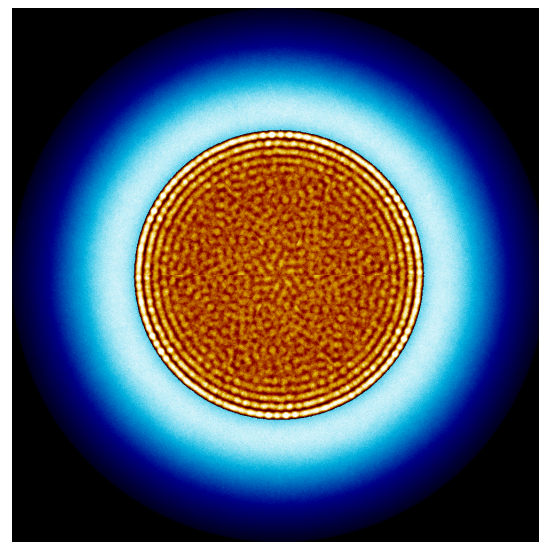


Figure 3: An Image Generated by Subtracting Figure 2b from Figure 4.3b.

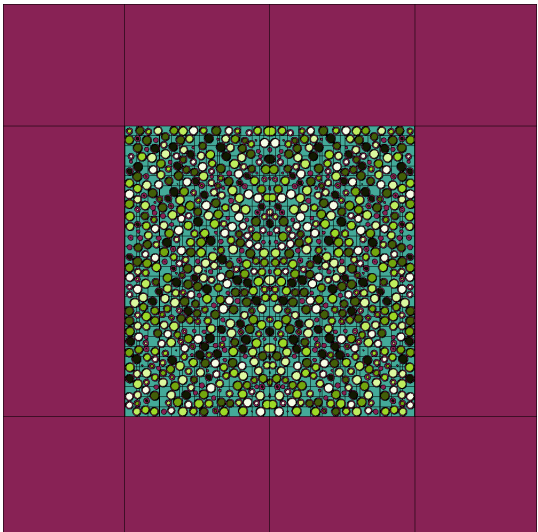
Figure 2 provides fission rate and thermal flux visualization meshes for the symmetry test using the 60 - 120 degree slice. Figure 3 is the result of using image-difference between the control's full-core radial mesh and the symmetry test's mesh.



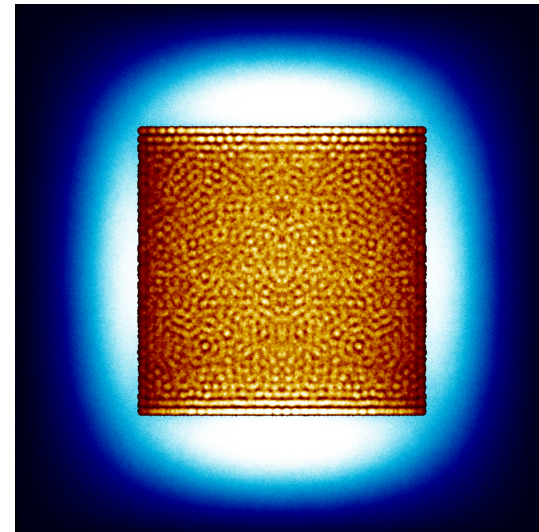
(a) Radial Cross Section at  $y=0$



(b) Radial Mesh



(c) Axial Cross Section at  $z=0$



(d) Axial Mesh

Figure 4: Sensitivity Analysis:  $\frac{1}{6}$  Symmetry Using the Portion of the Core Between  $120^\circ - 180^\circ$

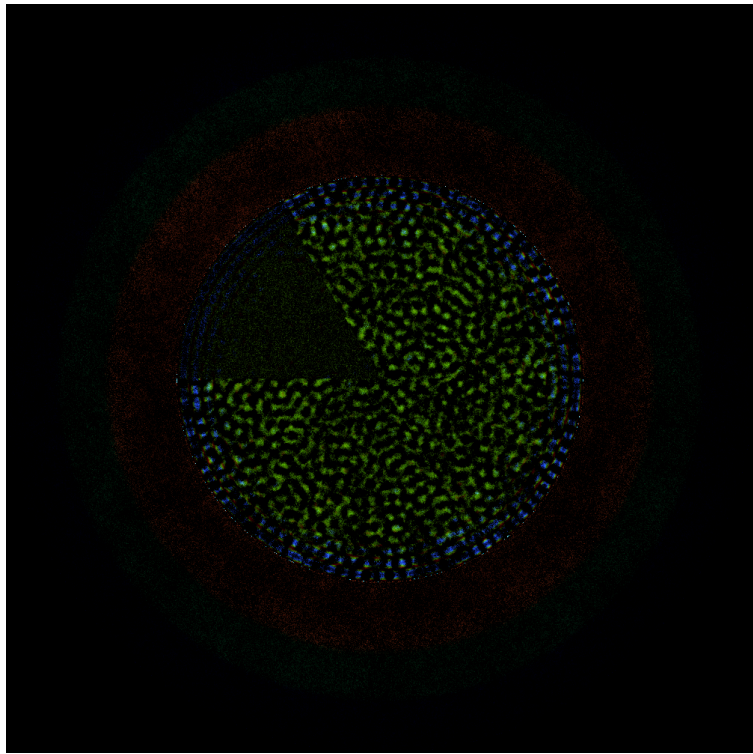
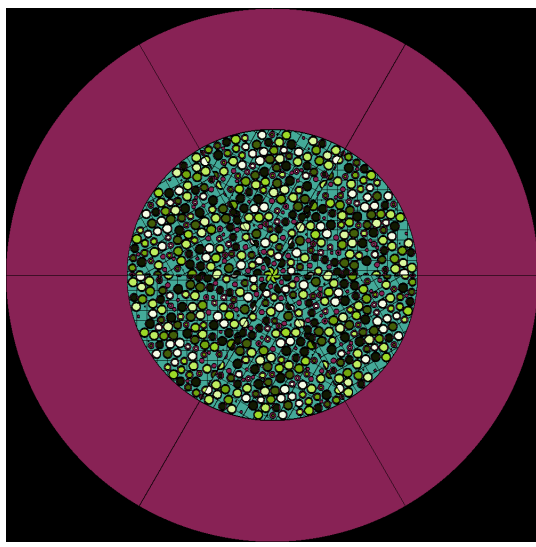
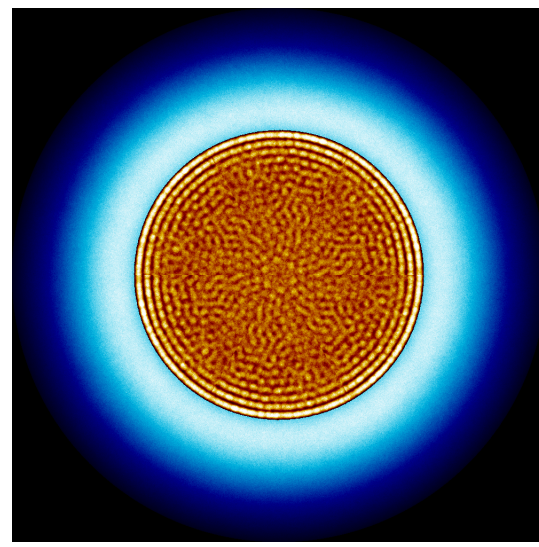


Figure 5: An Image Generated by Subtracting Figure 4b from Figure 4.3b.

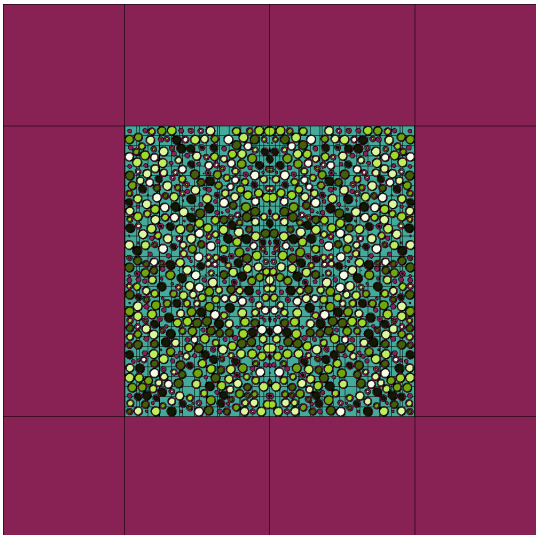
Figure 4 provides fission rate and thermal flux visualization meshes for the symmetry test using the 120 - 180 degree slice. Figure 5 is the result of using image-difference between the control's full-core radial mesh and the symmetry test's mesh.



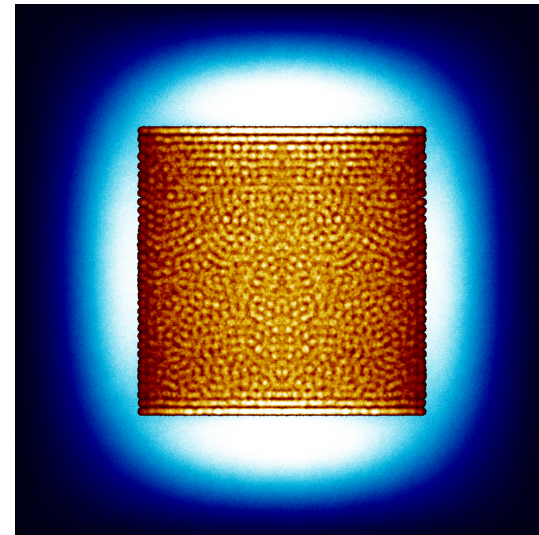
(a) Radial Cross Section at  $y=0$



(b) Radial Mesh



(c) Axial Cross Section at  $z=0$



(d) Axial Mesh

Figure 6: Sensitivity Analysis:  $\frac{1}{6}$  Symmetry Using the Portion of the Core Between  $180^\circ - 240^\circ$

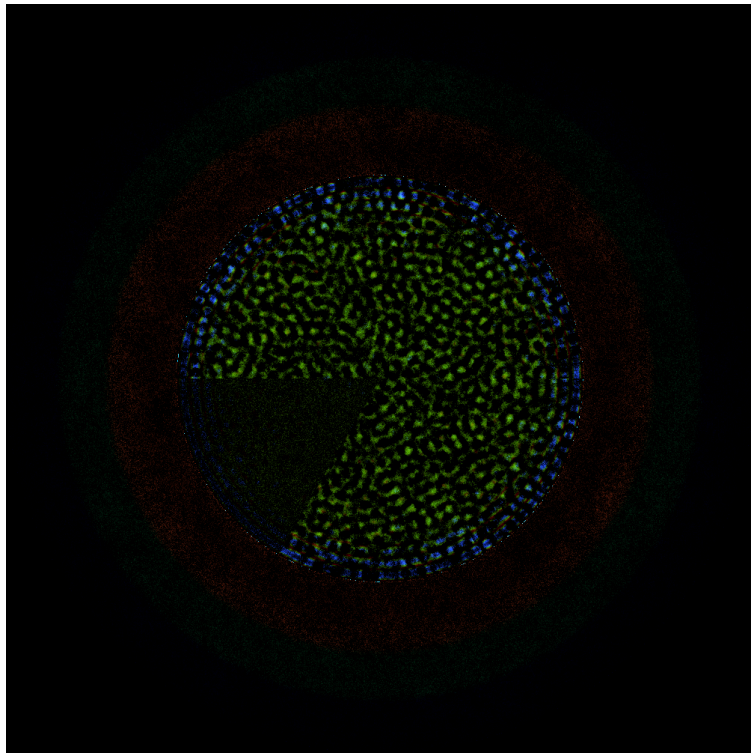
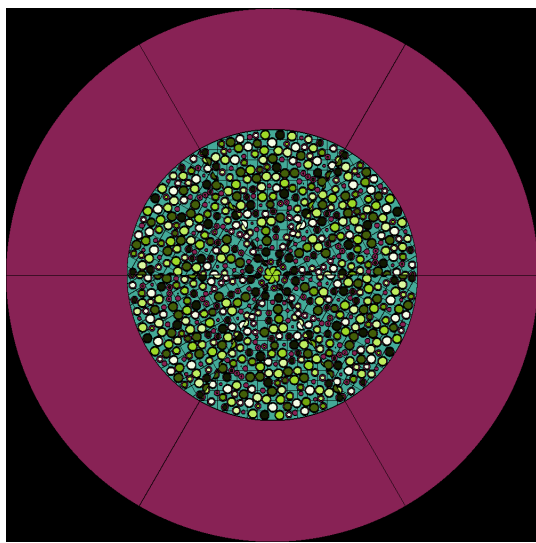
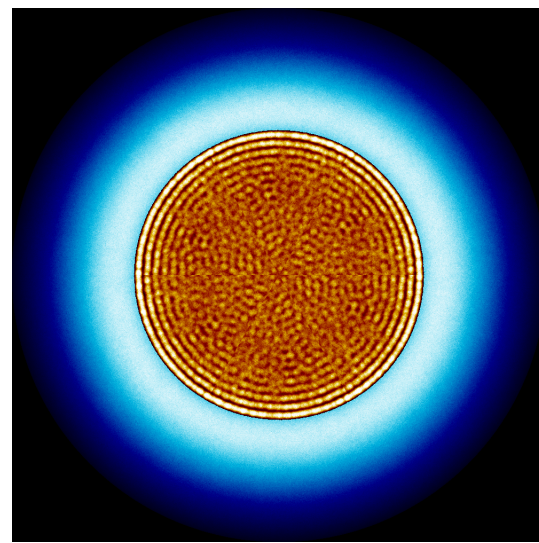


Figure 7: An Image Generated by Subtracting Figure 6b from Figure 4.3b.

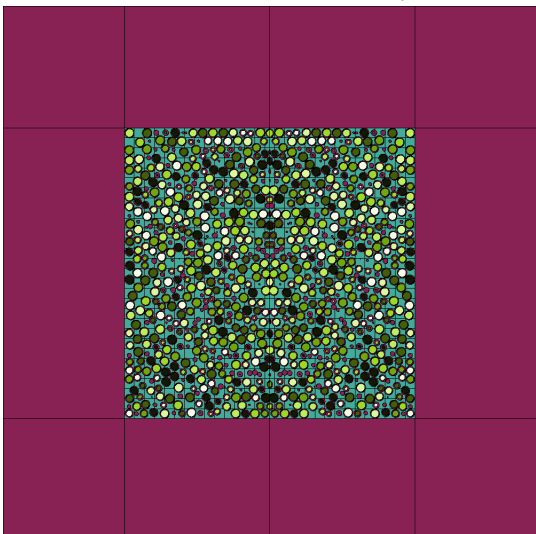
Figure 6 provides fission rate and thermal flux visualization meshes for the symmetry test using the 180 - 240 degree slice. Figure 7 is the result of using image-difference between the control's full-core radial mesh and the symmetry test's mesh.



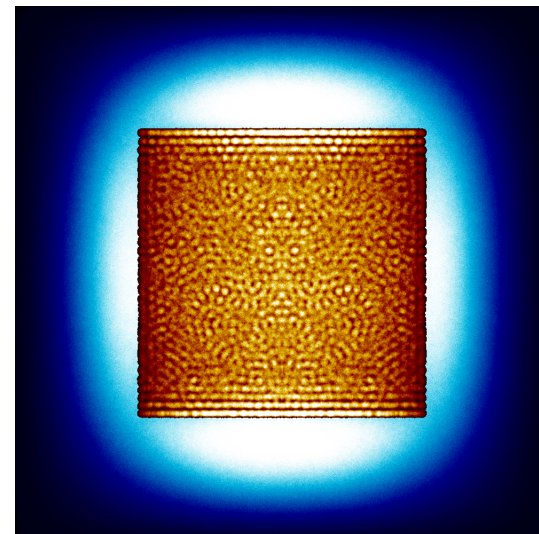
(a) Radial Cross Section at  $y=0$



(b) Radial Mesh



(c) Axial Cross Section at  $z=0$



(d) Axial Mesh

Figure 8: Sensitivity Analysis:  $\frac{1}{6}$  Symmetry Using the Portion of the Core Between  $240^\circ - 300^\circ$

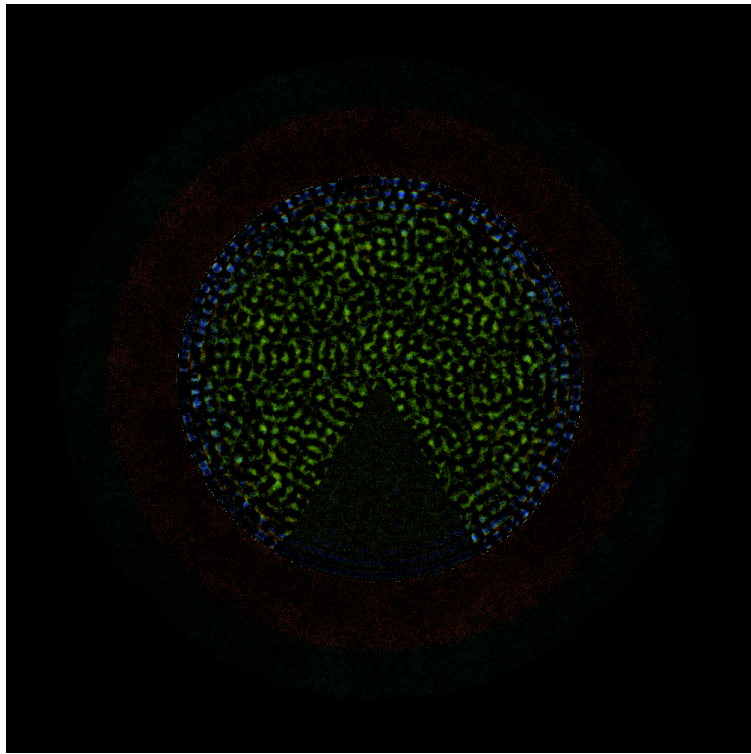
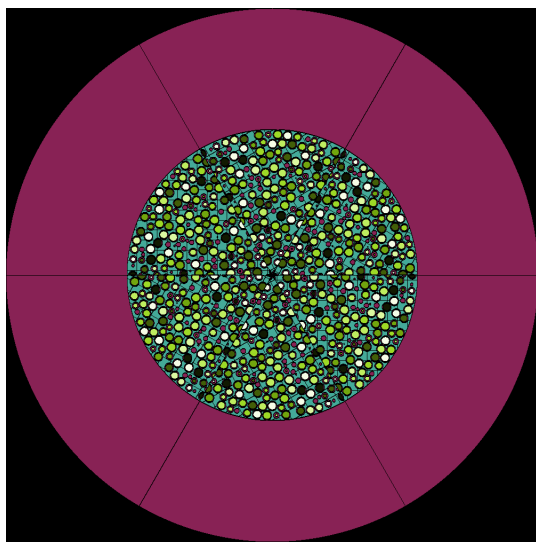
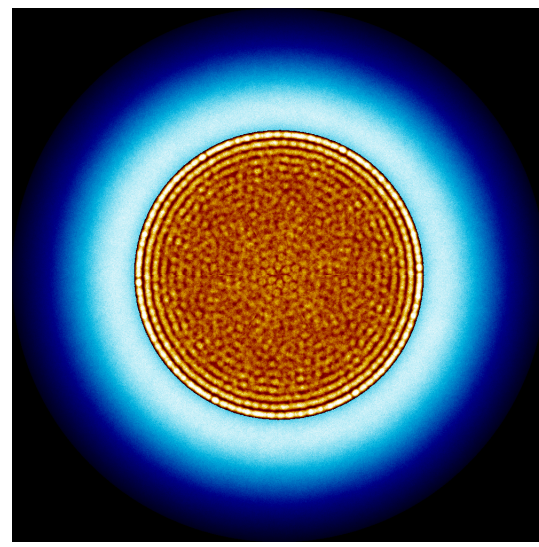


Figure 9: An Image Generated by Subtracting Figure 8b from Figure 4.3b.

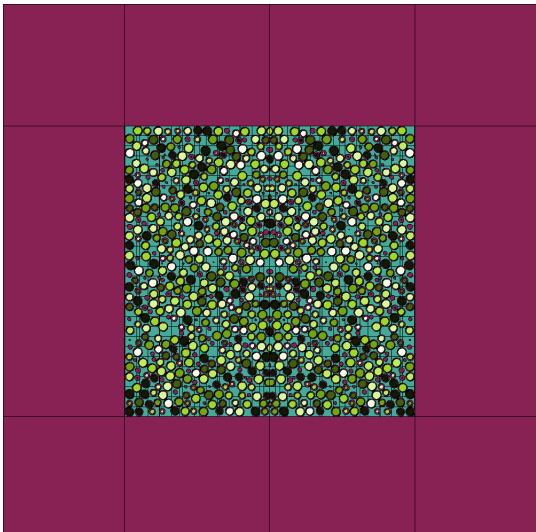
Figure 8 provides fission rate and thermal flux visualization meshes for the symmetry test using the 240 - 300 degree slice. Figure 9 is the result of using image-difference between the control's full-core radial mesh and the symmetry test's mesh.



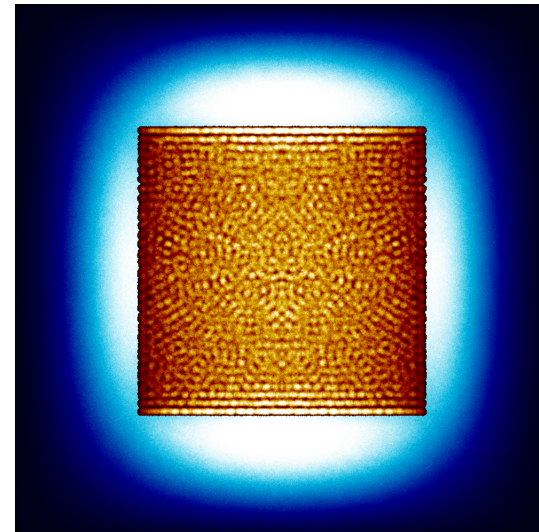
(a) Radial Cross Section at  $y=0$



(b) Radial Mesh



(c) Axial Cross Section at  $z=0$



(d) Axial Mesh

Figure 10: Sensitivity Analysis:  $\frac{1}{6}$  Symmetry Using the Portion of the Core Between  $300^\circ - 360^\circ$

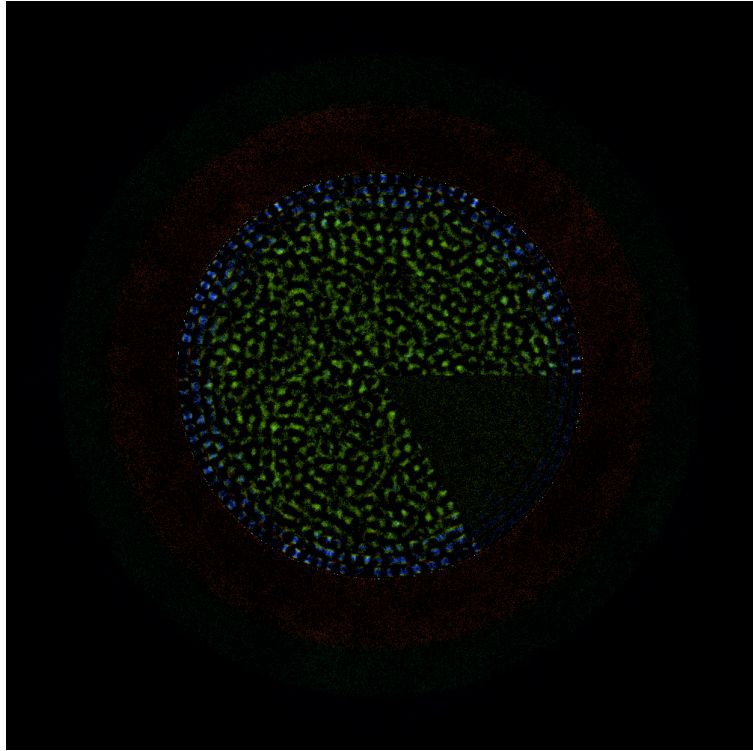


Figure 11: An Image Generated by Subtracting Figure 10b from Figure 4.3b.

Figure 10 provides fission rate and thermal flux visualization meshes for the symmetry test using the 300 - 360 degree slice. Figure 11 is the result of using image-difference between the control's full-core radial mesh and the symmetry test's mesh.

In each of the image difference results, the section of the core the symmetry assumption uses — for example, the portion of Figure 3 in the sector from  $60^\circ$  -  $120^\circ$  — is very dark. This means that this region has very little difference between it and the same sector on the control model result. The boundaries of these sectors in the image difference are also hard lines, not gradients, which suggests that the neutronics (specifically the fission rate) within and around pebbles closest to the boundary of the sector might not be as significantly impacted by their neighbor pebbles "changing" as expected. The image difference results also show very little difference in the reflector region, which makes sense, as the reflector is uniform. However, this does indicate that there wasn't a local peak in thermal flux due to, say, a mass of fresh pebbles in the representative slice. If there were such a spike, there would likely be repeating regions of brighter "hotspots" in the reflector everywhere *except* the representative sector used in the symmetry assumption.

## C Shuffle Test

Section C contains the geometry cross sections, fission rate/thermal flux meshes, and image difference results from the shuffling tests (see Section 3.7, Table 3.6), which were omitted from the main report for brevity.

Comparing the image difference results of Section C, the shuffling test, to Section B, the symmetry test, shows that the shuffling tests have a weaker effect on the fission rate and thermal flux than the symmetry tests. The small differences in this particular test would most likely indicate that the core is generally well-mixed, i.e., that each bin in the vertical direction, along the z axis, has each of the 7 fuel compositions represented equally.

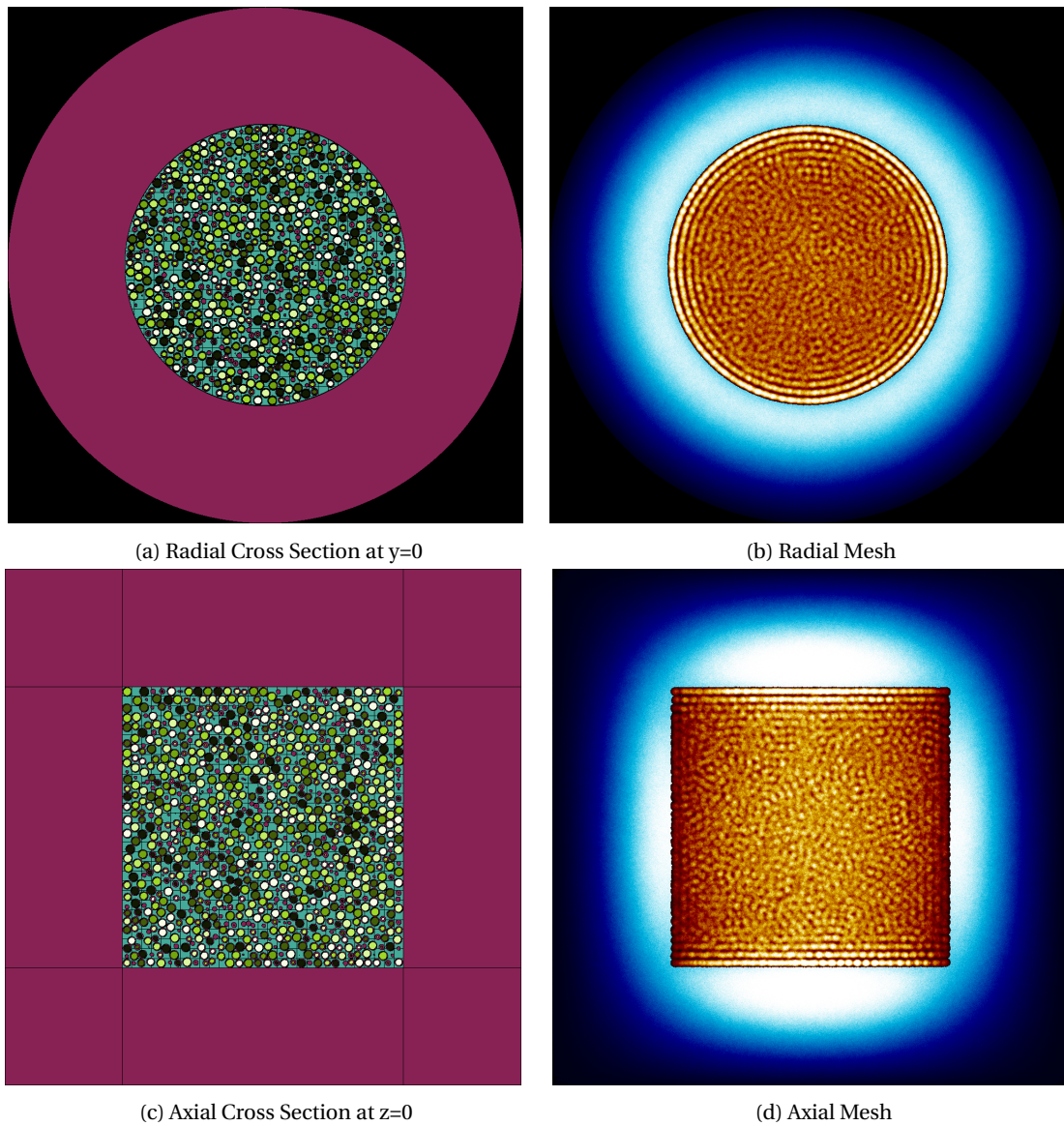


Figure 12: Shuffle Analysis: Run 1

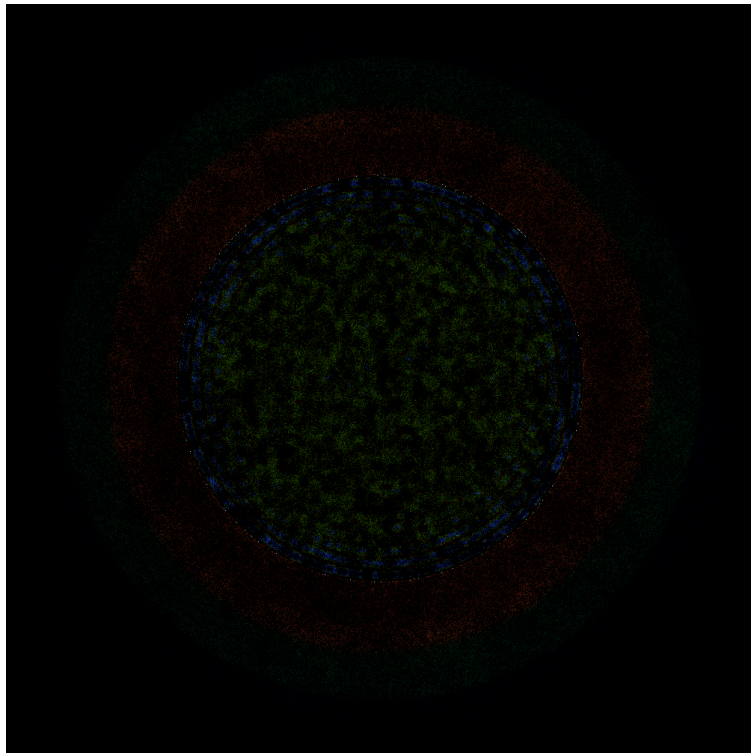
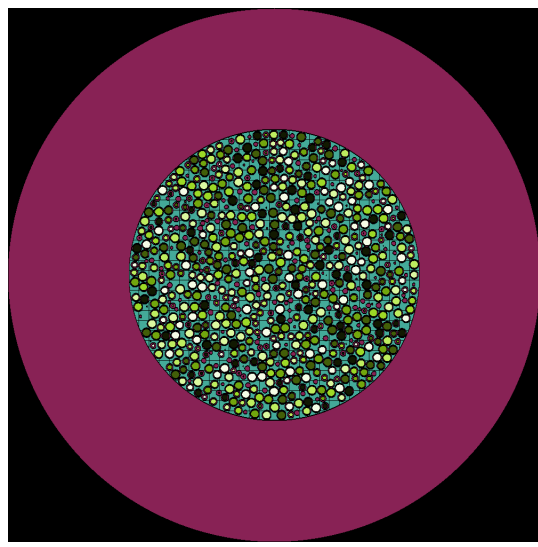
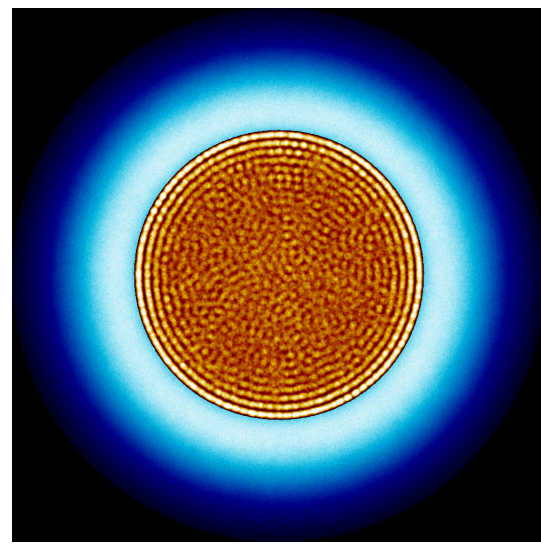


Figure 13: An Image Generated by Subtracting Figure 12b from Figure 4.3b.

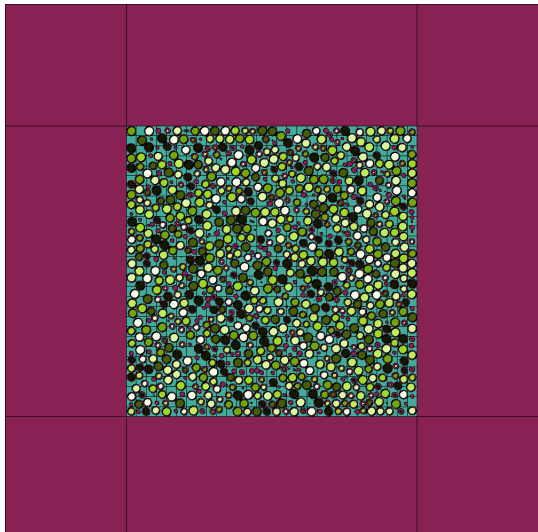
Figure 12 provides the thermal flux and fission rate meshes and geometric cross sections axially and radially. Figure 13 is the result of the image difference between the full core control mesh and Figure 12b.



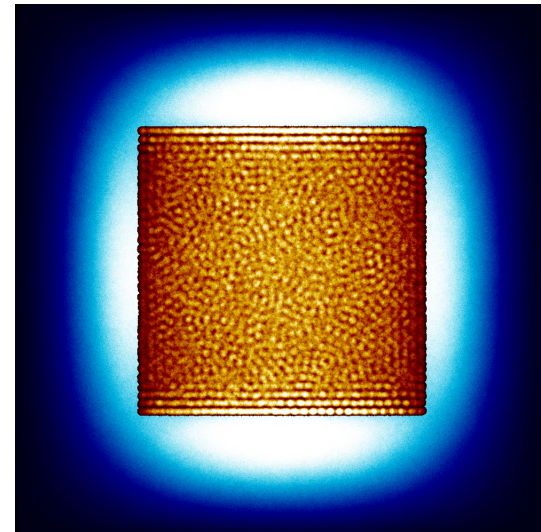
(a) Radial Cross Section at  $y=0$



(b) Radial Mesh



(c) Axial Cross Section at  $z=0$



(d) Axial Mesh

Figure 14: Shuffle Analysis: Run 2

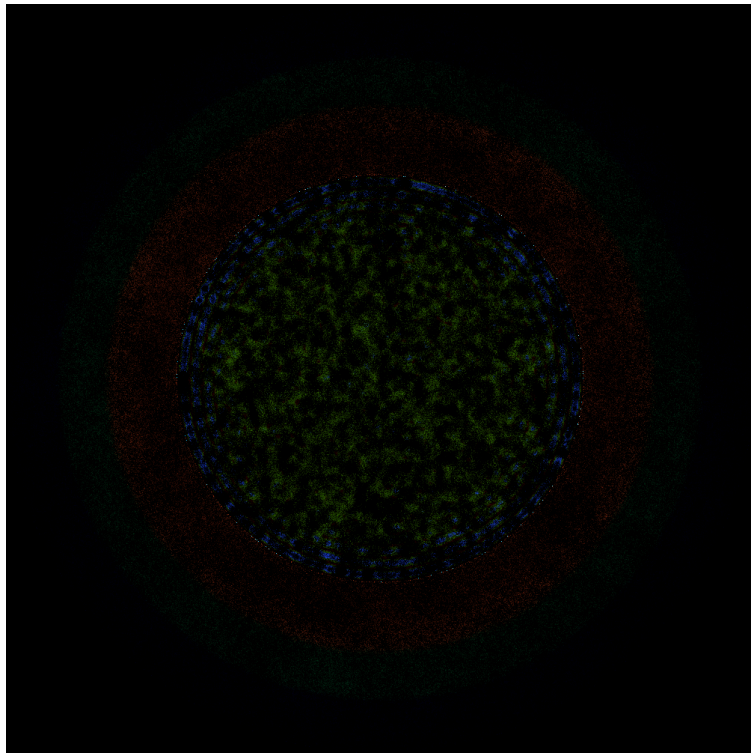
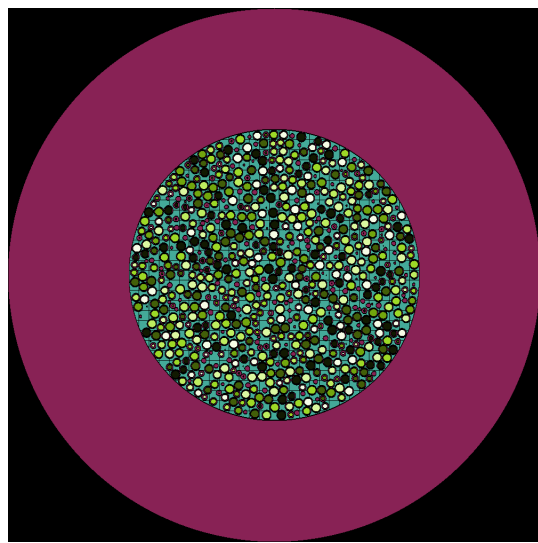
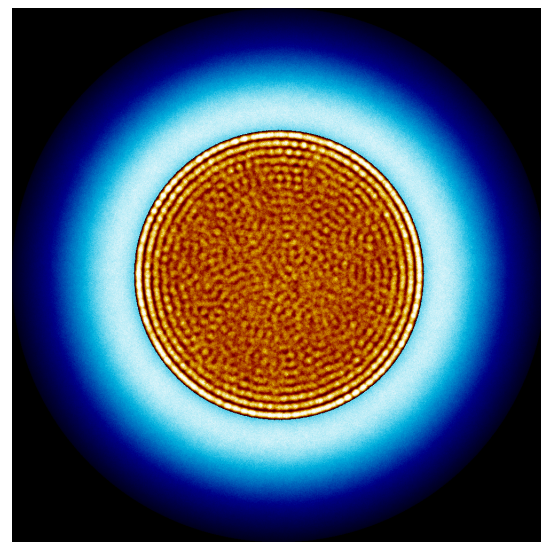


Figure 15: An Image Generated by Subtracting Figure 14b from Figure 4.3b.

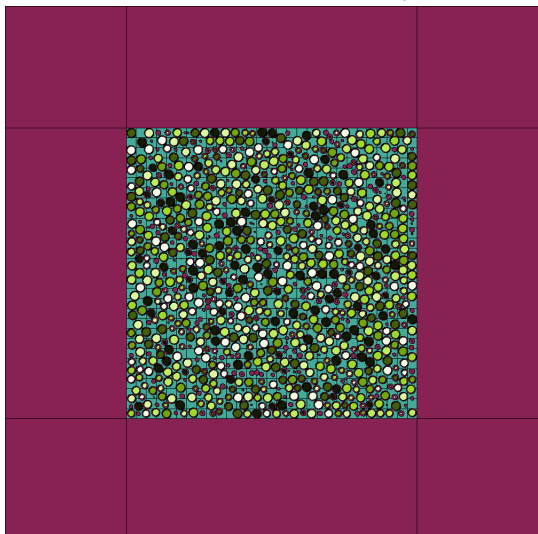
Figure 14 provides the thermal flux and fission rate meshes and geometric cross sections axially and radially. Figure 15 is the result of the image difference between the full core control mesh and Figure 14b.



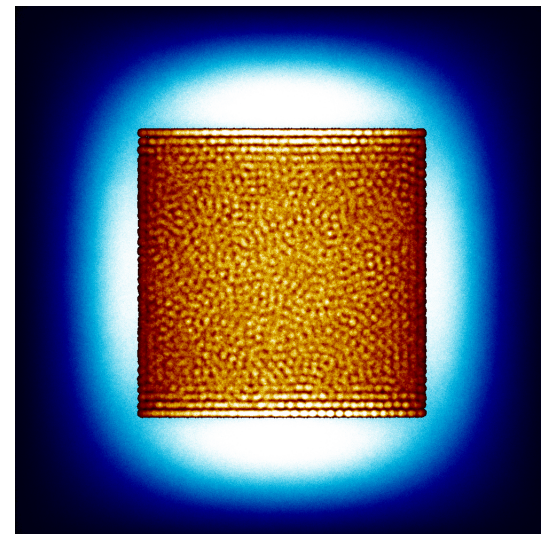
(a) Radial Cross Section at  $y=0$



(b) Radial Mesh



(c) Axial Cross Section at  $z=0$



(d) Axial Mesh

Figure 16: Shuffle Analysis: Run 3

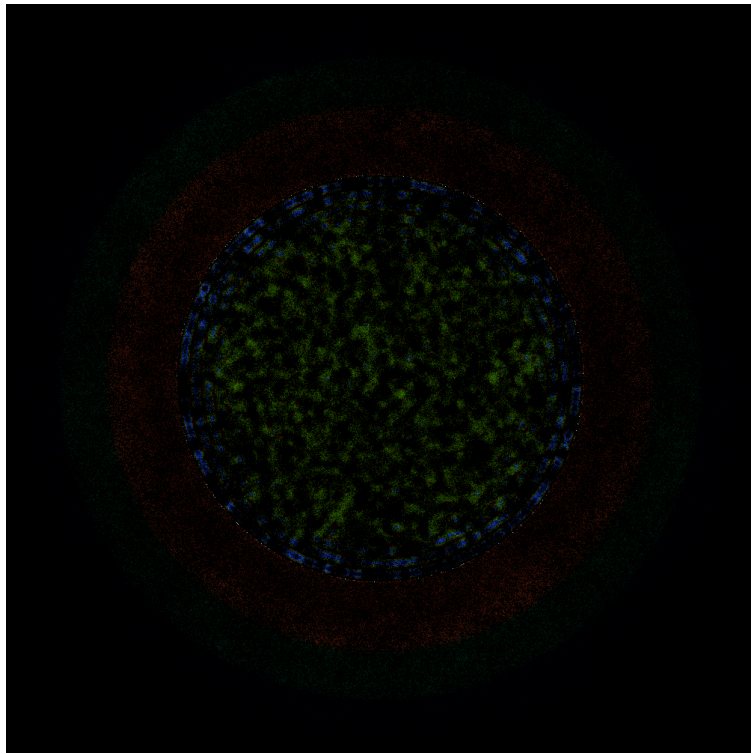
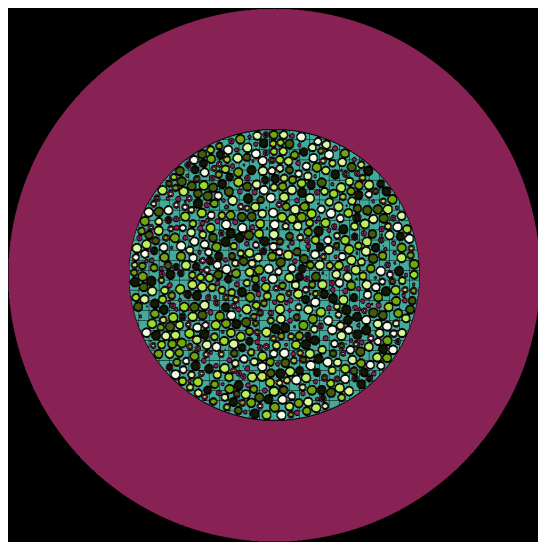
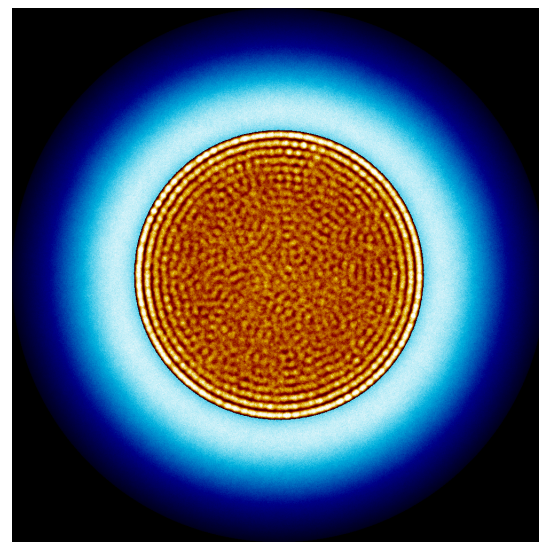


Figure 17: An Image Generated by Subtracting Figure 16b from Figure 4.3b.

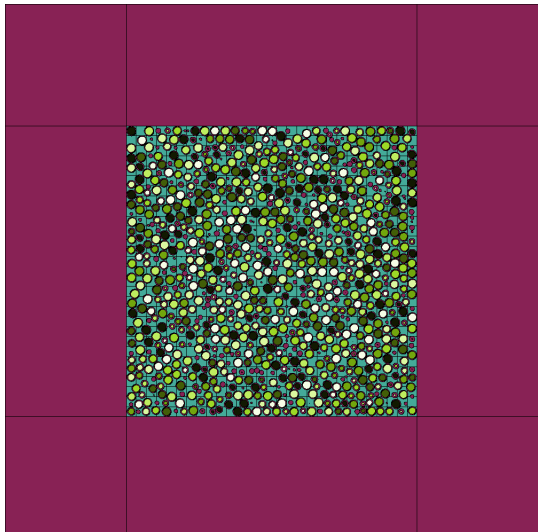
Figure 16 provides the thermal flux and fission rate meshes and geometric cross sections axially and radially. Figure 17 is the result of the image difference between the full core control mesh and Figure 16b.



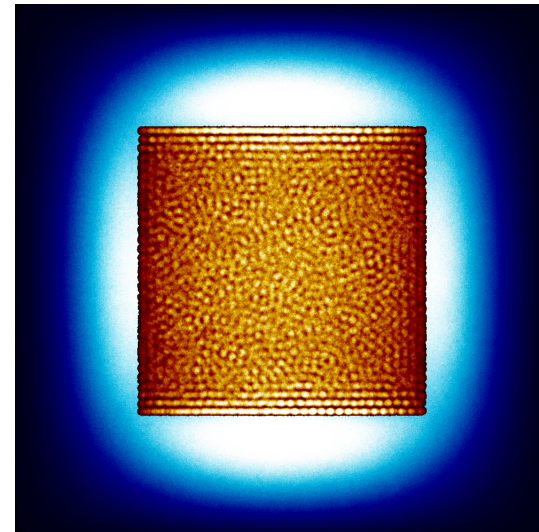
(a) Radial Cross Section at  $y=0$



(b) Radial Mesh



(c) Axial Cross Section at  $z=0$



(d) Axial Mesh

Figure 18: Shuffle Analysis: Run 4

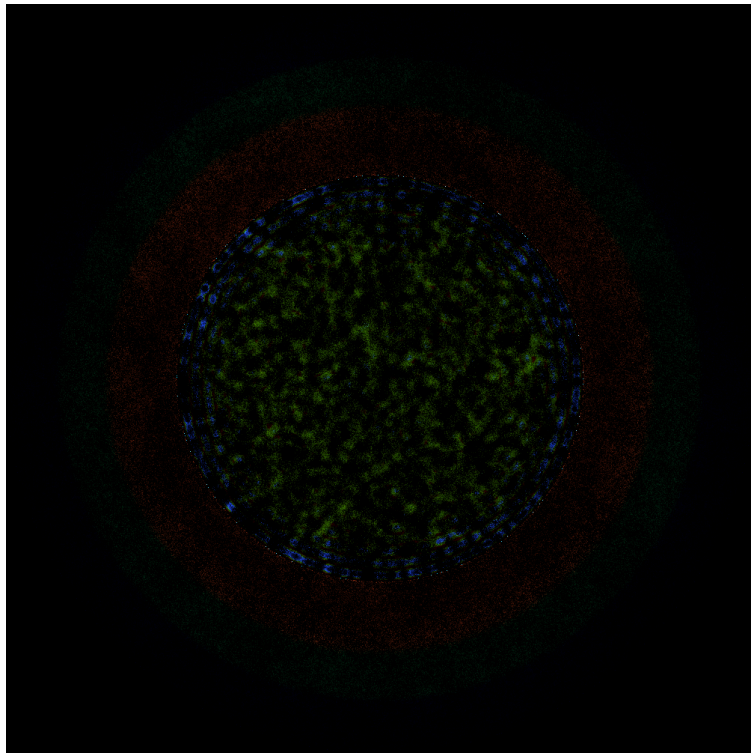
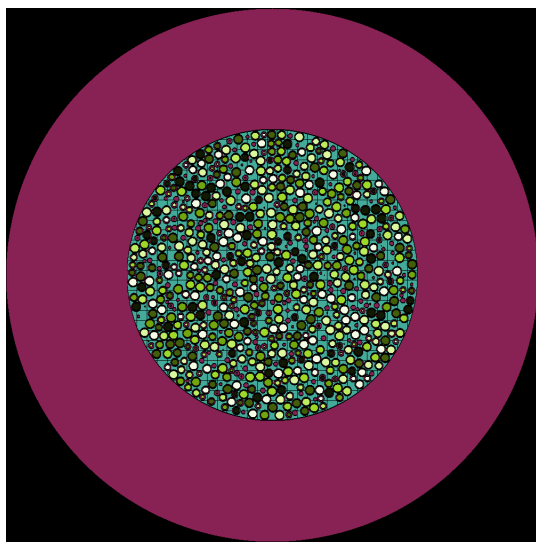
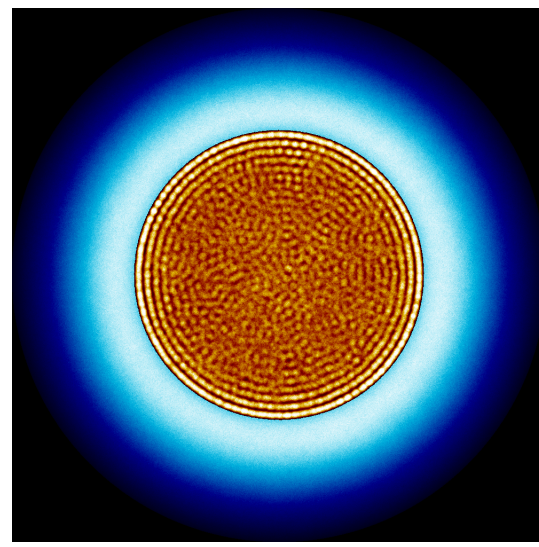


Figure 19: An Image Generated by Subtracting Figure 18b from Figure 4.3b.

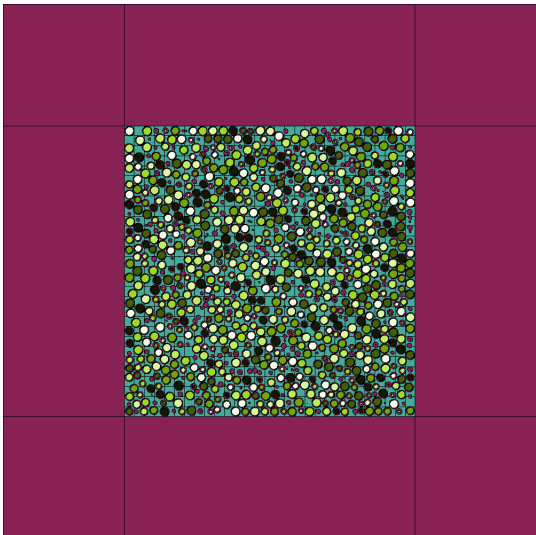
Figure 18 provides the thermal flux and fission rate meshes and geometric cross sections axially and radially. Figure 19 is the result of the image difference between the full core control mesh and Figure 18b.



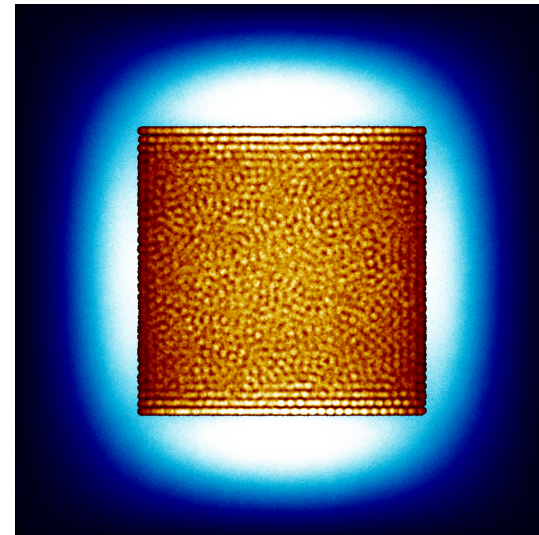
(a) Radial Cross Section at  $y=0$



(b) Radial Mesh



(c) Axial Cross Section at  $z=0$



(d) Axial Mesh

Figure 20: Shuffle Analysis: Run 5

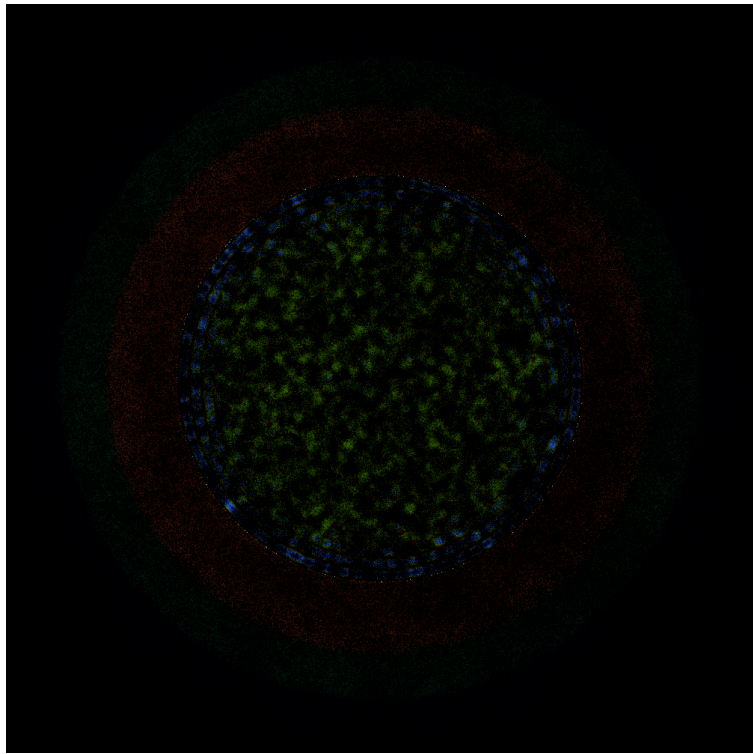
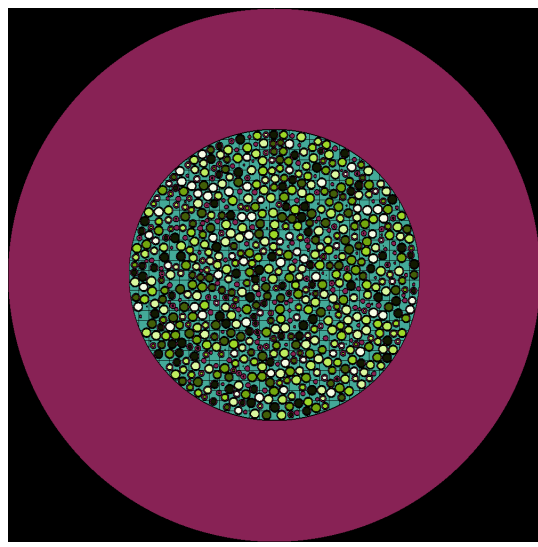
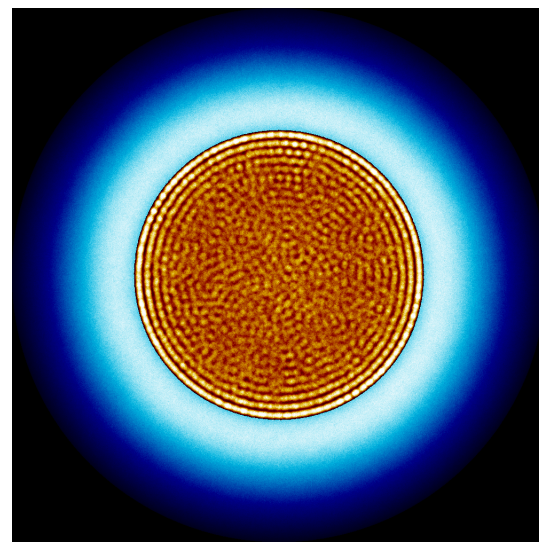


Figure 21: An Image Generated by Subtracting Figure 20b from Figure 4.3b.

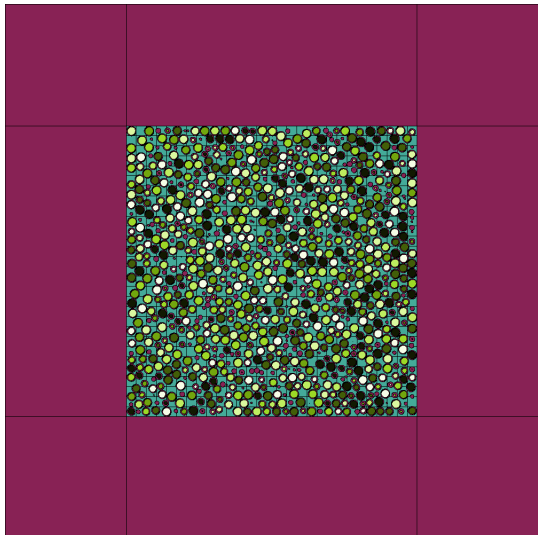
Figure 20 provides the thermal flux and fission rate meshes and geometric cross sections axially and radially. Figure 21 is the result of the image difference between the full core control mesh and Figure 20b.



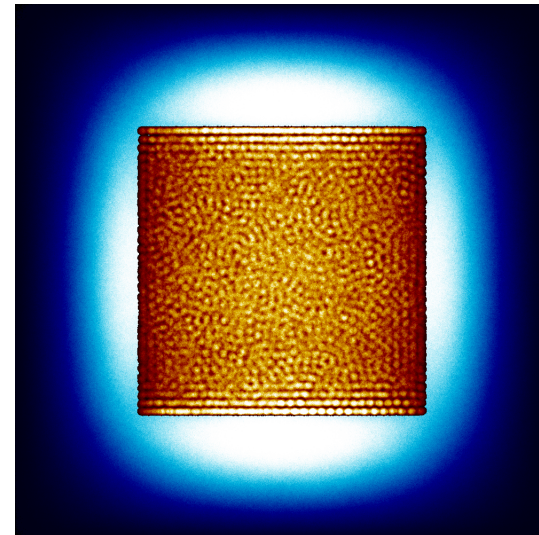
(a) Radial Cross Section at  $y=0$



(b) Radial Mesh



(c) Axial Cross Section at  $z=0$



(d) Axial Mesh

Figure 22: Shuffle Analysis: Run 6

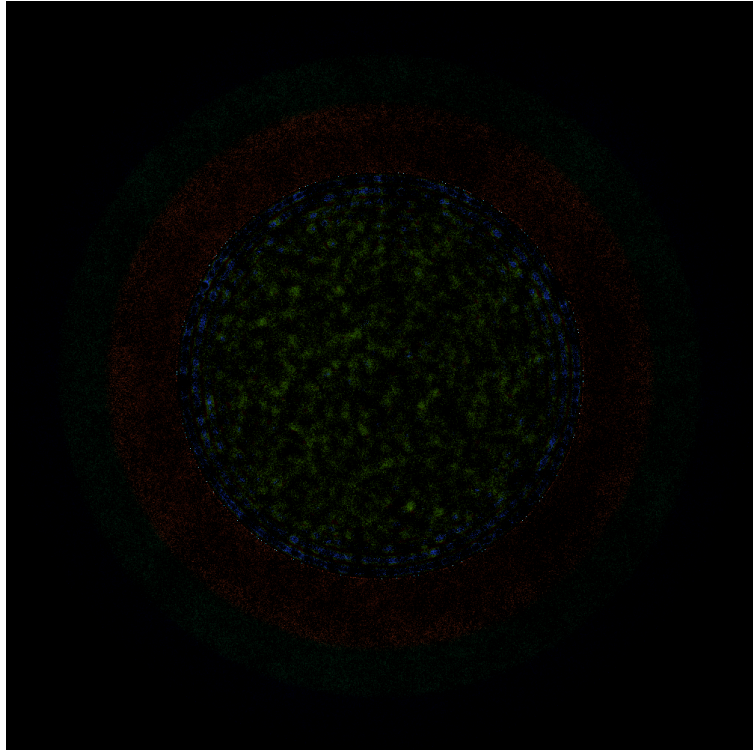


Figure 23: An Image Generated by Subtracting Figure 22b from Figure 4.3b.

Figure 22 provides the thermal flux and fission rate meshes and geometric cross sections axially and radially. Figure 23 is the result of the image difference between the full core control mesh and Figure 22b.

There are a few hotspots where small regions show a brighter patch of green. The best example of this is in the fourth quadrant of Figure 23, near the  $270^\circ$  line. Hotspots such as this could be caused by poor mixing, which would make some pebbles occur in higher concentrations (and then cause a larger difference in the shuffle test, when the same region is now dominated by a different burnup) or by the shuffling putting a different pebble burnup in a region of lower or higher flux. To investigate the source of this, the pebbles in a 10 cm square column (10 cm in x and y, the height of the reactor in z) around the hotspot were found. Table 2 shows the count of each pebble burnup.

Table 2: Representation of Pebbles by Number of Passes in a 10 cm Square Rectangular Prism Surrounding an Image Difference Hotspot at Approximately x = 11 cm, y = -56 cm

Pebble Pass	Number of Pebbles
Fresh	20
First Pass	12
Second Pass	13
Third Pass	12
Fourth Pass	10
Fifth Pass	14
Sixth Pass	11

When this region was narrowed further, to a 5 cm region, the poor mixing was more dramatic, as seen in Table 3.

Table 3: Representation of Pebbles by Number of Passes in a 5 cm Square Rectangular Prism Surrounding an Image Difference Hotspot at Approximately x = 11 cm, y = -56 cm

Pebble Pass	Number of Pebbles
Fresh	10
First Pass	3
Second Pass	4
Third Pass	1
Fourth Pass	2
Fifth Pass	2
Sixth Pass	2

In the 10 cm square column, fresh pebbles originally make up 21.7% of all pebbles in the region. In the 5cm square column that is tighter around the hotspot, fresh pebbles make up 41.7% of all pebbles. The hotspot pointed out in Figure 23 exists in some degree in Figures 13, 15, 17, 19, and 21 — it is simply brightest in Figure 23 because the shuffle scheme corresponding to this Figure 23 replaces fresh pebbles with 6-pass pebbles, which have the greatest disparity in burnup.